DYNAMICS OF LASER-DRIVEN SHOCK WAVES IN FUSED SILICA

By

PETER MARTIN CELLIERS

B.Sc.(Eng.), Queen's University, 1980

M.A.Sc., The University of British Columbia, 1983

A THESIS SUBMITTED IN PARTIAL FULFILLMENT OF
THE REQUIREMENTS FOR THE DEGREE OF
DOCTOR OF PHILOSOPHY

in

THE FACULTY OF GRADUATE STUDIES
DEPARTMENT OF PHYSICS

We accept this thesis as conforming
to the required standard.

THE UNIVERSITY OF BRITISH COLUMBIA

September 1987

In presenting this thesis in partial fulfilment of the requirements for an advanced degree at the University of British Columbia, I agree that the Library shall make it freely available for reference and study. I further agree that permission for extensive copying of this thesis for scholarly purposes may be granted by the head of my department or by his or her representatives. It is understood that copying or publication of this thesis for financial gain shall not be allowed without my written permission.

Department of Physics

The University of British Columbia
1956 Main Mall
Vancouver, Canada
V6T 1Y3

Date 15 October 1987

ABSTRACT

The formation of a laser-driven shock in fused silica was observed experimentally. Fused silica slabs were irradiated with 0.53 μm laser light in a pulse of 2 ns FWHM at intensities ranging from 10^{12} W/cm^2 to 5×10^{13} W/cm^2, producing a pressure pulse ranging from $<$ 30 GPa to 500 GPa. Shock trajectories were observed using streaked shadowgram and schlieren methods. The experiment was modelled with a one-dimensional Lagrangean laser-plasma hydrocode. Comparison of the simulation results with the experimental observations indicate that the high pressure shock develops anomalously slowly at intensities $> 1 \times 10^{13}$ W/cm^2. Furthermore the shock displayed non-steady propagation for a transient period following its formation. The non-steady propagation is interpreted to be due to a relaxation process in the phase transformation of the fused silica to the high pressure stishovite phase which occurs in the shock front. The slow formation of the shock at high intensities is consistent with a significant volume collapse (phase transition) possibly induced by isentropic compression; however, this interpretation is uncertain due to the complications introduced by non-equilibrium thermodynamics and the possibility of two-dimensional motion.

TABLE OF CONTENTS

LIST OF TABLES

LIST OF FIGURES

ACKNOWLEDGEMENT

I would like to thank my research supervisor, Dr. A. Ng, for the opportunity to work in a unique laser facility (for a Canadian university), which has undergone continuous improvement largely due to his persistent efforts. As well, I thank my supervisory committee, Dr. B. Ahlborn, Dr. A.J. Barnard and Dr. D. Beder, for their time and effort.

I received a great deal of help from Dean Parfeniuk in performing the experimental measurements of this work, and in subsequent discussions of the results. Also, Luiz Da Silva was of great help for problems in computing and in general discussions related to laser plasmas. Hubert Houtman was very helpful in introducing me to dye lasers and other useful practical things. Alan Cheuck, who is indispensable to the plasma group, performed great services in ensuring that equipment worked, and important supplies were always available. As for other members of the plasma group, I thank them for the company and interesting coffee time diversions.

The financial assistance of the Natural Sciences and Engineering Research Council is appreciated.

CHAPTER 1

INTRODUCTION

1.1 High pressure physics and laser-driven shocks

The study of high pressure physics is of multidisciplinary interest and is important in understanding phenomena in geophysics, planetary physics, high density plasmas, condensed matter physics, inertial confinement fusion and nuclear explosions. Shock compression of solids has played a major role in the field of high pressure physics, and has led to many notable discoveries. Of particular interest is information on the thermodynamic properties of matter at high pressure, the most important being the equation of state or EOS. Measurements of the propagation of high pressure shock waves can be used to infer the EOS at high pressures[1].

Dynamic pressures exceeding many megabar can be obtained in solids using various techniques. Many early measurements were accomplished with explosive systems[2]. Explosive systems are still widely used, but the state-of-the art in precision is obtained with the two stage light gas gun[3]. These techniques have been refined over the years to provide precise measurements of the equation of state of many solids. They are currently limited to the pressure range < 1 TPa (1 TPa = 10 Mbar). Much higher pressures can be obtained with nuclear explosions[4], but this technique is expensive and not available to most researchers; it is therefore more suitable for providing accurate benchmark data in the high pressure regime.

With the advent of high power pulsed lasers, the achievement of ultra-high pressures through the laser ablation process became a reality. Much of the initial impetus for studying laser-matter interactions was directed towards utilizing the high pressures to drive spherical implosions in inertial confinement fusion schemes[5,6]. The use of these high pressures as a tool for high pressure physics research was soon recognized, and laser driven shocks have been studied as a laboratory technique for more than a decade[7-10]. Laser-driven shocks differ from conventionally produced shocks in several distinct aspects. The principal advantage is that higher pressures can be obtained with laser irradiation, up to roughly 10 TPa. However, sample sizes are typically much smaller, usually with thickness < 100 μm, and the time durations are correspondingly smaller, from $0.5 - 5$ ns. The pressure is easily controlled by varying the laser intensity at the target surface.

The laser-driven ablation process is shown schematically in Figure 1-1. The laser light is focussed at intensities of typically $10^{12} - 10^{15}$ W/cm^2 onto the solid target surface. During the process of ablation the surface layer of the solid target material is vaporized, and expands into the vacuum; this forms a plasma on the surface of the target. The laser can be considered as an energy source which heats the plasma. For sub-micron laser wavelengths most of the energy is absorbed in the plasma before the laser light reaches the critical density layer (n_{cr}). This is the surface at which the electron plasma frequency is resonant with the laser frequency, where the light is reflected, and beyond which it cannot penetrate. The absorbed laser energy heats the coronal plasma to temperatures of the order of $200 - 2000$ eV. Thus a very large temperature gradient exists between the n_{cr} layer and the cold solid. This results in a large thermal flux into the cold target causing ablation of the solid. The region containing the large gradients is called the ablation zone, and the point where it joins onto the cold solid is called the ablation front. The ablated material flows outward past n_{cr} and into the coronal plasma which expands into the vacuum at velocities around 10^7 cm/s.

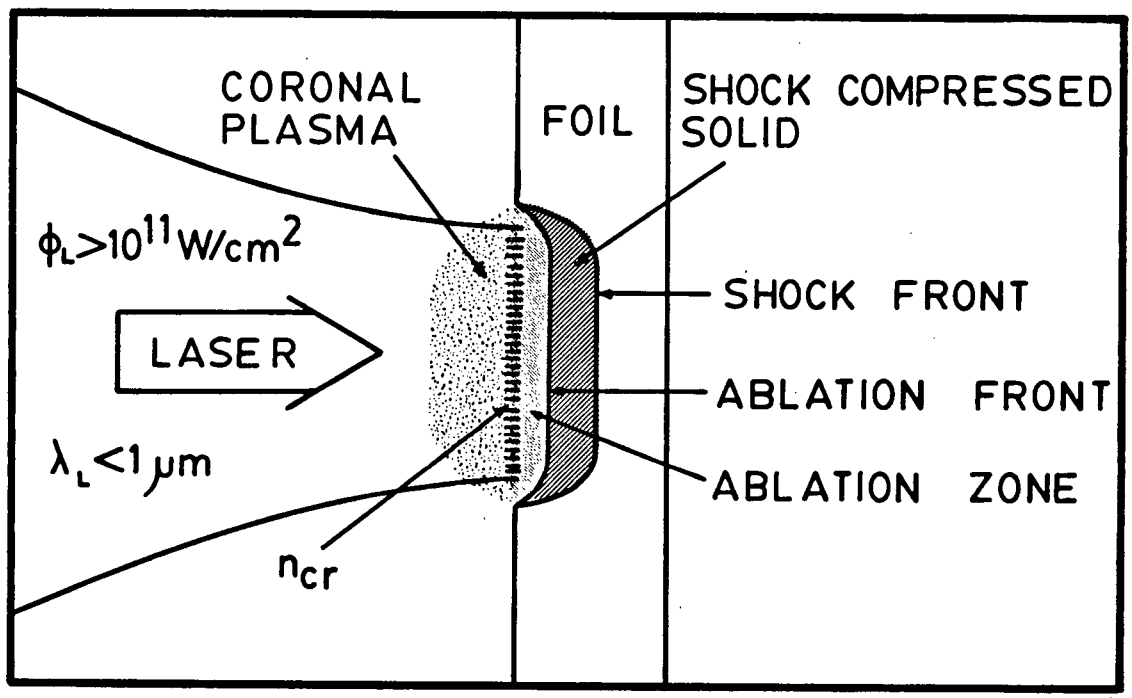

Figure 1-1 Schematic of a solid target irradiated by laser radiation at high intensities.

The laser-driven shock arises essentially out of momentum conservation. The momentum of the the high speed plasma flow into the vacuum generates large pressures (which are nearly proportional to the focussed laser intensity) at the surface of the target. This drives a strong shock into the target. The shock propagates much faster than the ablation front. It compresses and accelerates an amount of mass about an order of magnitude larger than the mass boiled off to produce the plasma flow.

Two types of experimental diagnostics have been used to study laser-driven shocks. Firstly, for an opaque target, such as a metal foil, the shock can be observed at the moment it emerges from the target rear surface[8-12]. This technique has been used to map the shock trajectory by measuring the shock arrival time for several different target thicknesses, which then leads to a measurement of the shock speed[11,13]. Several shots are necessary to obtain this measurement. A more sophisticated variation of this uses (one or more) steps on the target rear surface so that the shock arrival time at each step may be used to infer a shock speed in a single shot[8-10]. Detection of the shock arrival at the rear surface can be achieved by observing the luminescence[8-11,13] of the shock-heated material, or by observing the change in surface reflectivity[12] (using a probe light) as the unloading material expands to low densities. In both cases a high speed streak camera is used as the detector. For equation of state research, the shock speed alone is insufficient to determine the thermodynamic state of the shocked material. Another parameter is required, such as particle speed or pressure. This is much more difficult to obtain; the impedance mismatch technique, using layered targets of different materials, is one method for obtaining the additional information[14].

The second method for observing laser-driven shocks utilizes tranparent targets. In this case it is possible to observe the shock with an optical imaging system, by viewing it from the side. This technique was first demonstrated by van Kessel and co-workers using plexiglas and solid H_2 targets[7,15,16]. The information obtained

is essentially the same: shock speed can be inferred, which leads to estimates of the pressure. However, with a streak camera one can obtain a continuous observation of the shock formation and evolution process within a single shot. This can provide much more information for detailed comparison with hydrodynamic models of the laser-matter interaction. Furthermore, with two-dimensional time-resolved framing photographs one could obtain information on two-dimensional motion of the shock front[16]. The main disadvantage of this technique is that it is restricted to materials that are initially transparent.

A number of problems associated with the laser-driven shock method have been identified[17]. These include target preheat due to suprathermal electrons and X-rays, shock planarity and uniformity, shock attenuation, and experimental difficulties associated with high speed microscopic nature of the diagnostics. Trainor and Lee[18] have discussed some of the problems due to electron preheat and shock decay, and provide a semi-empirical model for optimizing shock experiments for a 1.06 μm Nd-laser. The suprathermal electrons create an enormous electrostatic field in the vicinity of the laser produced plasma which has led to dielectric breakdown in transparent targets at 1.3 μm. These effects were so severe as to obscure the shock formation process near the surface of the target[19,20]. The preheat problems due to suprathermal electrons are reduced drastically with shorter wavelength laser radiation (as well as reduced laser intensity – at the expense of reduced pressure). For wavelengths approaching ultra-violet radiative preheat becomes a greater concern. Finally, the problems of uniformity and planarity of the shock are related to the intensity distribution and overall size of the focussed laser spot at the target surface.

1.2 Present investigation

The main objective of this work was to obtain detailed measurements of the formation of a laser-driven shock in a transparent solid material, and compare

these to detailed calculations of the shock trajectory. The measurement technique was essentially the same as that used by van Kessel and Sigel[7], who observed the shock from side-on streak measurements. The measurements were designed to examine the shock formation process with high spatial and temporal resolution, with emphasis on examining the trajectory in the early stages of its formation when the laser pulse is rising in intensity. A comprehensive theoretical investigation of the shock formation process was undertaken using a hydrocode to model the laser-matter interaction. Despite the fact that this technique had been demonstrated more than a decade ago, a detailed study of this sort has not been reported in the literature. The only other major study with this intention is that reported by Amiranoff *et al.*[20] who encountered the problems with dielectric breakdown, which prevented them from examining the shock in the early stages of its development when the pressure is highest. In the experiments performed for this thesis the laser intensity was moderate, and the wavelength was much shorter (0.53 μm) so that suprathermal electrons were not a problem.

The target material used in the experiment was fused silica.† Comparison of the experimental results with the hydrocode simulations has revealed some important features. The measurements yield the first observation of non-steady shock propagation in a laser-driven shock experiment. In addition, there is an anomalous delay for the formation of the shock above a certain laser intensity. Both of these effects cause noticeable disagreement between the measured shock trajectories and simulated trajectories. The simulations are based on standard computer modelling methods used for analyzing laser-target experiments which have been very successful in modelling previous laser-driven shock experiments[9,10,13]. The results are

† This material is variously called "quartz", "fused quartz", "fused silica", and "vitreous silica" in the literature. These names all refer to the amorphous form of SiO_2 with density $\sim 2.2 g/cm^3$ at standard conditions.

interpreted qualitatively in terms of high pressure phase transformations known to occur in silica.

The results, and the disagreement with simulations, are significant because they suggest that rate-dependent kinetics of the transformation processes are not only evident in the measurements, more importantly they appear to *dominate* them. Phase transformation kinetics under shock compression is an area of condensed matter physics and shock compression science which is still not well understood. A detailed study of a pressure-induced phase transformation using laser-driven shocks has not, up to now, been reported in the literature. As noted above the main emphasis with the laser shock technique has been the achievement of extremes in pressure. However, the other extreme – microscopic space and time scales – offered by the laser shock technique is particularly suited to studying fast phase transformations. This is because the nanosecond time and micron length scales characteristic of laser-shock experiments have the best chance of revealing relaxation effects in solid-solid phase transformations such as that occuring in silica at high pressure.

1.3 Thesis outline

Chapter 2 reviews details of shock compression of phase transforming solids including the known high pressure data on silica. The equation of state models used in the hydrocode calculations are briefly described, and compared with Hugoniot (shock wave) data. A description of the experimental facility is given in chapter 3. Details of the experimental arrangement for obtaining shock trajectories is then described. Finally, a description of the raw data and the method used to reduce it to a trajectory measurement is given. The hydrocode for producing trajectory calculations is described in chapter 4. This is followed by a comprehensive review of the shock formation process as predicted by the hydrocode under the conditions obtained in the experiment. The effects of various additions to the physical model

used in the basic hydrocode were examined to see how they might modify the predicted trajectories. The data extracted from a series of trajectory measurements is presented in chapter 5 and compared with the hydrocode predictions. This is followed by a detailed discussion of the measurements and interpretations. A summary of the main results from experiment and simulation is given in chapter 6, as well as suggestions for further investigations.

CHAPTER 2

SHOCK COMPRESSION AND SILICA AT HIGH PRESSURE

2.1 Introduction

This chapter presents a review of current knowledge of silica under high pressure conditions. This includes information derived from static compression, shock compression, and isentropic compression experiments. A qualitative description of shock compression of solids, including the effects of phase transformations, is given as an introduction to the review of the high pressure properties of SiO_2.

2.2 Shock compression process

2.2.1 Rankine-Hugoniot relations

The locus of thermodynamic states obtained from shock compression of a material is uniquely determined by the equation of state. This locus is usually called the shock adiabat or Rankine-Hugoniot curve or simply the Hugoniot. This curve can be calculated in a completely general manner by considering only the conservation of mass, momentum and energy across the shock front. Conservation of mass and momentum across the shock front can be written in the form,

$$\frac{V_0}{V} = \frac{D}{(D-u)} \qquad [2-1]$$

$$p - p_0 = \frac{Du}{V_0} \qquad [2-2]$$

Here D is the shock speed and u is the particle speed behind the shock front as measured in the laboratory frame in which the particle speed ahead of the shock front is zero. p is the pressure and V is the specific volume; the subscript 0 indicates the initial state (ahead of the shock), and no subscript refers to the state behind the shock. The equation for conservation of energy across the shock front relates the internal energies of the initial state, E_0, and the final state, E, to the pressure and volume jumps across the shock,

$$E - E_0 = \frac{1}{2}(p + p_0)(V_0 - V). \qquad [2-3]$$

Thus, there are three equations, while there are five parameters associated with the shocked state: D, u, p, V, and E. If the equation of state, $p = p(V, E)$, is known for the material, then it may be added as a fourth equation which gives a system which can be reduced to a single equation with one free parameter. This equation gives the locus of points reached by single shocks, i.e. the Hugoniot. For many reasons the equation of state (EOS) is not known from theoretical considerations alone, so it must be measured. From the three conservation equations and simultaneous measurement of two shock parameters (e.g. D and u) the EOS parameters p, V and E (along the Hugoniot) can be inferred.

A schematic of the Hugoniot curve for a solid as it appears in the $p - V$ plane is shown by the solid curve in Figure 2-1. The natural initial state for shock compression of solids is the point (p_0,V_0) which corresponds to zero pressure ($p_0 =$

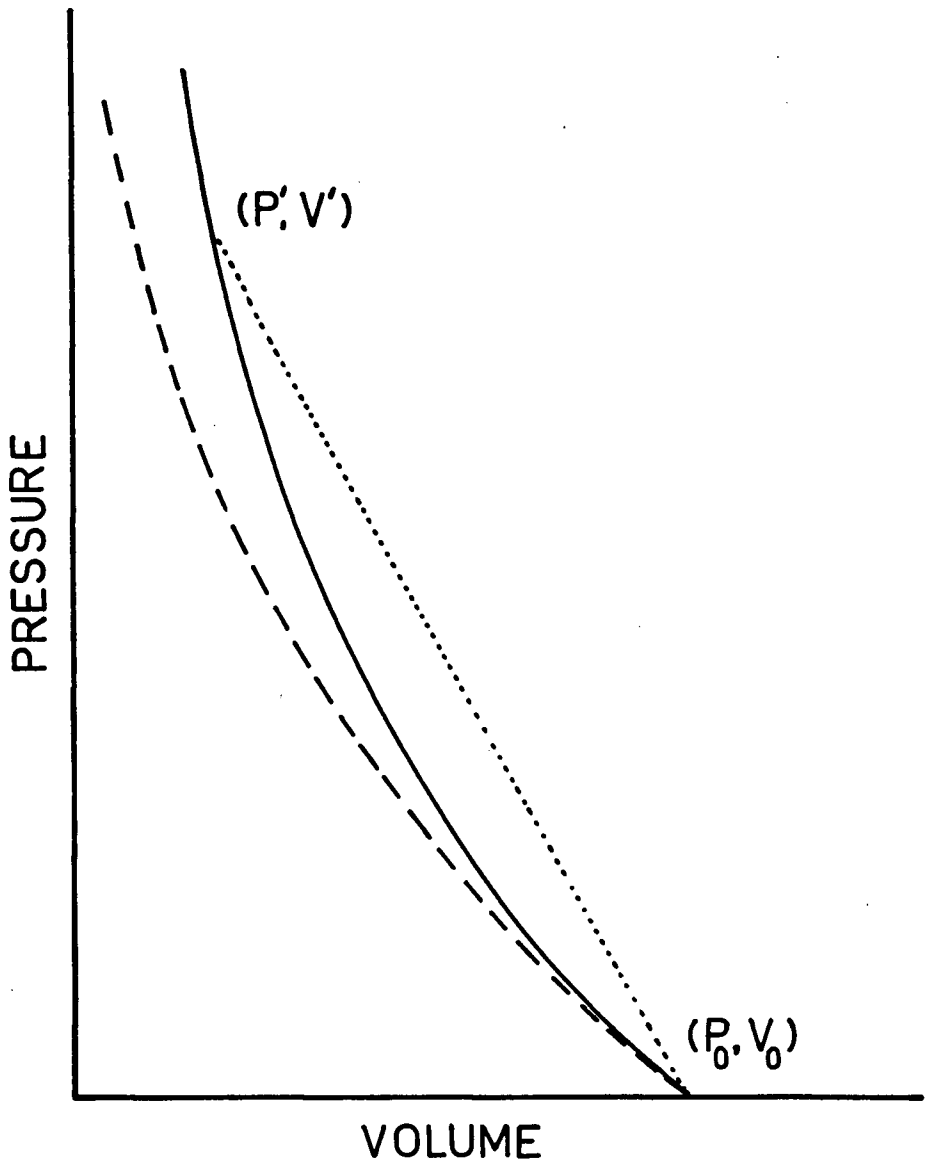

Figure 2-1 Schematic diagram of Hugoniot curve on the p-V plane. Indicated on the diagram are the Hugoniot (solid), the cold curve (dashed). Also shown is the Rayleigh line (dotted) for shock compression to the point (p', V') on the Hugoniot.

0) and the specific volume characteristic of the material at standard conditions.† The isentrope passing through this point is denoted by the dashed curve; this is also often referred to as the cold compression curve. The isotherm and isentrope at zero temperature are the same curve which is called the zero-degree isotherm.‡ For many metals, and other materials of simple atomic structure the zero-degree isotherm can be calculated theoretically using electron band structure models, usually to the accuracy of a few per-cent[1]. At low pressures (weak shocks) the Hugoniot is tangent to the cold curve, and the shock propagates at the sound speed. At higher pressures the shock process heats material irreversibly so that the Hugoniot crosses higher and higher isentropes with increasing pressure. Equations [2-1] and [2-2] can be combined to give,

$$p - p_0 = \frac{D^2}{V_0^2}(V_0 - V). \qquad [2-4]$$

On the thermodynamic $p-V$ plane a straight line drawn between the initial (V_0, p_0) and final (V, p) states has a slope proportional to D^2. This is called the Rayleigh line, and represents a useful graphical interpretation of the relationship between shock pressure, compression and shock speed: i.e. $D^2 \propto \Delta p/\Delta V$. The Rayleigh line is denoted by the dotted line in Figure 2-1.

---

† The term "standard conditions" normally refers to the material state at room temperature (273 K) and atmospheric pressure. For shock compression of solids 1 atm $\simeq$ 1 bar is a negligible quantity, thus it is convenient to regard the pressure at standard conditions as effectively zero, i.e. $p_0 = 0$.

‡ The zero-degree isotherm lies below the $T = 273$ K isotherm on the $p - V$ plane so that the volume at $p = 0, T = 0$ is slightly smaller than the volume at $p = 0, T = 273$ K by about $1 - 2$ %. This difference is very slight so that the zero-degree isotherm and the cold compression curve can be regarded as nearly identical, except for very precise purposes.

This simple treatment of the shock transition is applicable to gases and to condensed materials in the limit of strong shocks. However, at lower pressures the response of condensed matter to pressure loading is more complicated. Firstly, there are strength effects in which the material supports a stress which is not purely hydrostatic, but also contains a shear stress component. Secondly, many solids can undergo structural phase transitions in which the material transforms at a characteristic pressure to a phase different from that of its initial state, often accompanied by a volume collapse to a higher density. (Melting transitions are often accompanied by a slight volume expansion, and are not discussed explicitly in the following discussion.) Both of these effects are known to occur in silica at the lower end of the pressure range of the experiments described below. Material strength effects and/or phase transformations are manifested in the Hugoniot curve by one or more cusps as shown in Figures 2-2 and 2-3. The following section gives a qualitative description of the response of the material in these cases. Good reviews of the effects of material strength and phase transformations can be found in the works by Zel'dovich and Raizer[21] and by Duvall and Graham[22].

2.2.2 Elastic-plastic flow

Solids exhibit shear strength as one of their defining attributes. In the small amplitude limit longitudinal plane waves deform the material in a uniaxial fashion; that is, the material is compressed only in the direction perpendicular to the wave front, and not in the parallel direction. In the material behind the shock the stress distribution is anisotropic in which the longitudinal stress component is different from the lateral stress component. This type of wave is elastic because the material suffers no permanent deformation (at low stresses), and it is reversible. The stress-strain relationship can be plotted on the σ_ℓ-V plane as shown in Figure 2-2. Here σ_ℓ represents the longitudinal stress, which is usually the quantity accessible to the experimentalist. For a solid body undergoing uniaxial strain the longitudinal

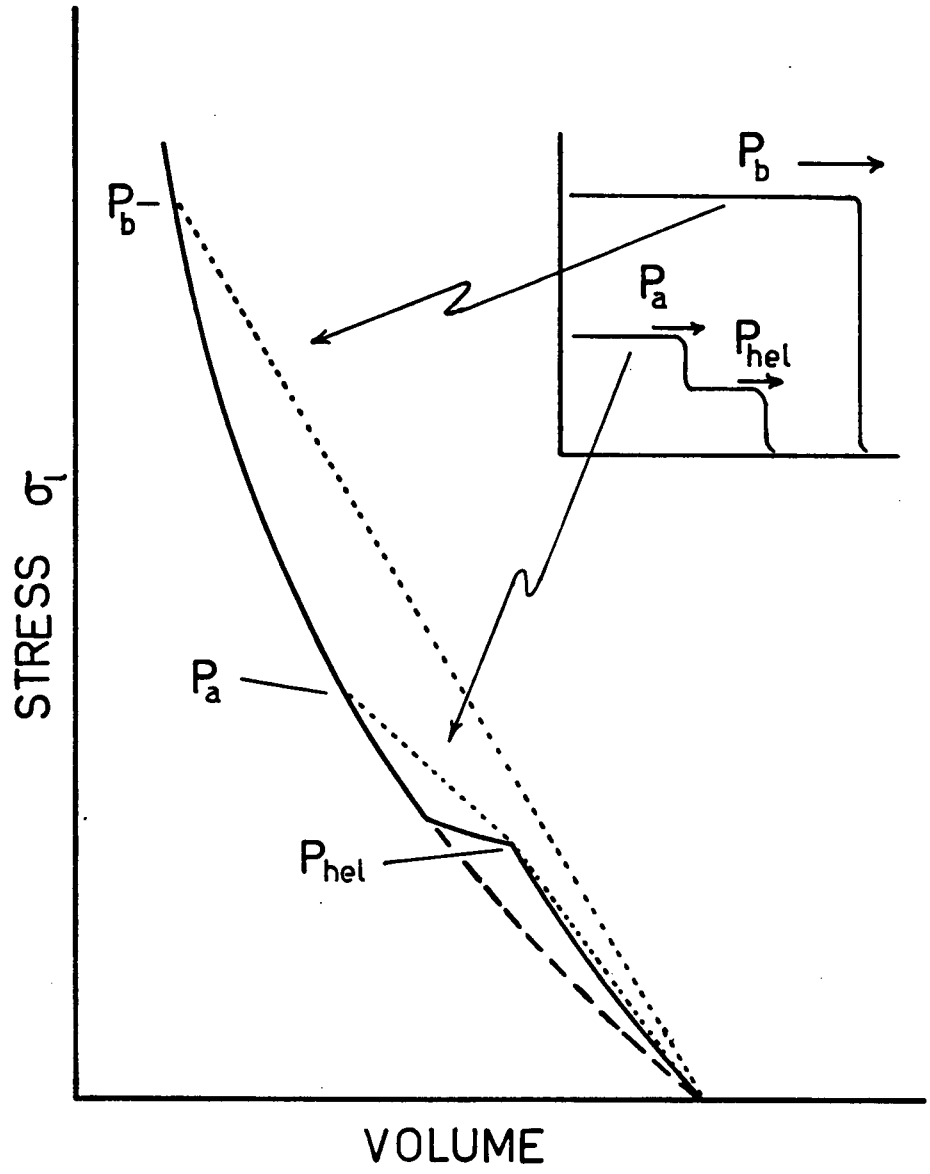

Figure 2-2 Schematic picture of shock compression of an elastic-plastic material. The Hugoniot is indicated by the solid curve, the hydrostat (bulk compression) by the dashed curve, and the Rayleigh lines by the dotted curves. The inset shows the pressure distribution in the compression process for: (a) pressure P_a which exceeds the HEL and results in a two-wave structure; and (b) pressure P_b which substantially exceeds the HEL so that the elastic wave is overtaken by the strong shock.

stress, σ_ℓ, and lateral stress σ_t are related to the mean stress (or hydrostatic pressure component), p by,

$$p = \frac{1}{3}(\sigma_\ell + 2\sigma_t) \qquad [2-5]$$

and the maximum resolved shear stress, τ, is given by,†

$$\tau = \frac{1}{2}(\sigma_\ell - \sigma_t) \qquad [2-6]$$

This results in the relationship[23],

$$\sigma_\ell = p + \frac{4\tau}{3}. \qquad [2-7]$$

Thus the elastic deformation curve lies above the equilibrium hydrostatic compression curve by an amount equal to $4\tau/3$. Therefore, the elastic wave travels at a greater speed than a fluid-like bulk compression wave in which the material deforms isotropically. If the driving stress exceeds a characteristic value, called the Hugoniot elastic limit (HEL), the material suffers permanent deformation (plastic flow) which tends to maintain the shear stress near a limiting value (equal to the shear strength). This creates a cusp on the Hugoniot curve as illustrated in Figure 2-2. At extreme pressures far beyond the HEL the effects of elastic shear strength diminish due to heating or melting and the material can usually be regarded as a hydrostatic fluid. In an intermediate regime above the HEL, material undergoes plastic deformation, as well as supporting shear stress. This regime of

† The maximum resolved shear stress is found by choosing a coordinate system which maximizes the shear stress along one of the coordinate directions. Such a coordinate system has one axis parallel to the wave front and another axis at a 45 degree angle to the wave front. The maximum resolved shear stress is therefore directed along planes oriented at 45 degrees with respect to the shock front.

stresses has been carefully studied for a number of materials initially using wave profile measurements[24] and more recently with piezoresistive gauges[25].

Because of the cusp at the HEL there is a range of driving stresses for which a single step wave transition is unstable. This can be seen by considering the Rayleigh lines for two stresses as shown in Figure 2-2. At the stress level $P_a > P_{hel}$ one may note that the Rayleigh line joining the initial state to P_a has a smaller slope than that of a compression to P_{hel}. This means that a single step compression to the state P_a would propagate at a slower speed than the elastic wave propagating at the lower stress level P_{hel}. The state P_a is therefore reached in a two-step process in which an elastic wave compresses the material to P_{hel}. This is followed by a slower plastic wave which completes the transition to P_a from the stress P_{hel}. The wave speeds can be calculated from the Rayleigh lines (dotted lines in Figure 2-2). The plastic wave travels more slowly than the elastic wave because of the smaller Rayleigh line slope, thus the two wave structure is stable. Two-wave structures are stable as long as the elastic wave speed exceeds the plastic wave speed. This condition is not met if the stress level is high enough that the Rayleigh line lies entirely above the Hugoniot. Such a situation corresponds to the stress level P_b in Figure 2-2. In this case a single step transition is stable, because it propagates at a higher speed than the elastic wave.

2.2.3 Phase Transformations

The wave structure occuring in a phase transforming material is in many ways similar to that which occurs due to elastic plastic flow. Figure 2-3 is a schematic representation of thermodynamic paths on the p-V plane for a phase transforming material, with initial volume V_0. For the purposes of this discussion, we assume that the stress is purely hydrostatic: $\sigma_\ell = \sigma_t = p$; $\tau = 0$. On the isotherm (dashed curve) phase transformation occurs near the pressure P_t. For a first order phase transition

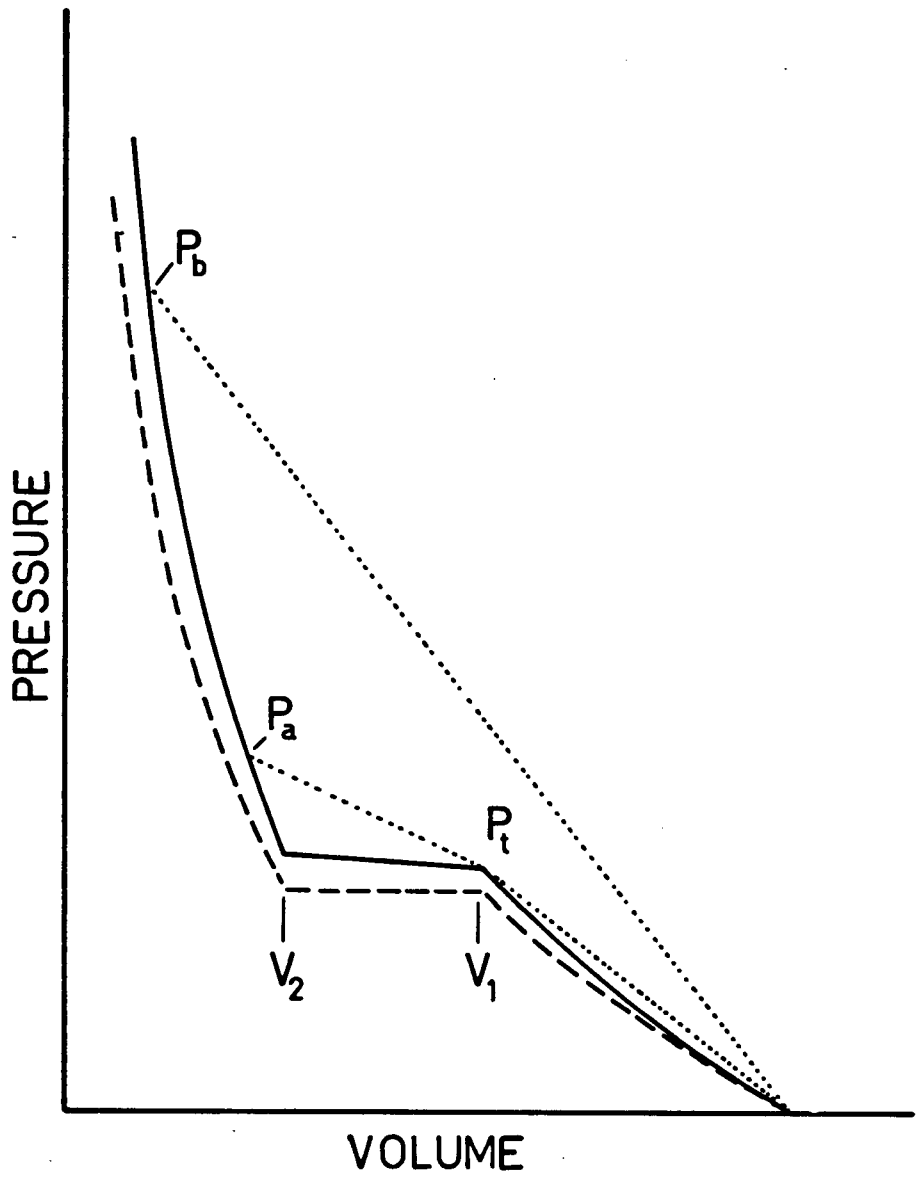

Figure 2-3 Schematic picture of the isotherm and isentrope for a phase transforming material. The isotherm is indicated by the dashed curve, and the isentrope by the solid curve. The dotted lines are the Rayleigh lines.

there is a discontinuous change of volume at constant pressure on the isotherm. Above P_t the isotherm follows a continuous curve characteristic of the structure of the new phase. The region at pressure P_t spanning the volume change from V_1 to V_2 is a mixed phase region where both the new and old phases may coexist with appropriate volume fractions to make up the mixed phase volume. An isentrope is indicated by the solid line in Figure 2-3. In compression the isentrope passing through a given state always has larger slope than the isotherm, thus this curve lies above the isotherm and has a non-zero slope in the mixed phase region. The Hugoniot curve, in turn, lies above the isentrope; however, at moderate pressures the Hugoniot is usually well approximated by the isentrope through the initial state. Thus one may consider the solid curve in Figure 2-3 to be the Hugoniot as well. At the transition pressure, P_t, on the Hugoniot there is a cusp in the curve due to the discontinuous change in slope. This leads to a stable two wave structure for pressures larger than P_t. The arguments for this behaviour parallel those given for elastic-plastic flow. The leading wave compresses the material in the intial phase up to the transition pressure P_t, while compression to the final state is accomplished in a slower second wave in which the actual phase transformation occurs. For very large pressures the compression can be accomplished in a single step transition (corresponding to P_b in Figure 2-3). Wave speeds can be calculated by constructing the usual Rayleigh lines, denoted by the dotted lines, as for the elastic-plastic transition.

2.2.4 Shock front structure

The analysis presented above has regarded the waves as being step transitions between distinct end states (the end points of the Rayleigh line segments). This corresponds to an ideal case where the shock jump equations described above represent the shock front as a mathematical discontinuity of infinitesimal thickness. In fact the shock front has finite thickness in which a variety of microscopic dissipative

mechanisms must play a role in entropy production. Usually these dissipation processes occur at a very high rate so that the material behind the shock front reaches thermodynamic equilibrium soon after the passage of the shock front. For simple metals, and in the limit of strong shocks (significantly above the HEL) Wallace[26,27] has calculated shock front thicknesses to be of the order of several hundred atomic layers, and rise times $\leq 10^{-12}$ s. The rise time decreases with increasing shock strength. When phase transformations are possible additional complications arise: a characteristic time scale is usually associated with the transformation processes occuring in the shock front. This makes rigorous theoretical calculations much more difficult for phase transforming materials. Time dependent effects have been experimentally observed both for elastic-plastic flow[28,29] and for shock-induced phase transformations[32-35].

When a time dependent process operates within a shock transition it modifies the observable aspects of the compression process. The time dependence arises from the fact that there is always a finite time period which the material takes to adjust itself to the load applied to it. Thus a pressure step applied to the material results in an initially non-steady propagation which relaxes to a steady state (constant speed) after several relaxation times. During this time the wave decelerates as enough time ellapses for the initial layers to reach equilibrium. When a steady state is achieved the transition between initial and final state is accomplished over a finite distance traversed by the travelling wave, which gives rise to a steady wave profile. These rate dependent effects have been detected experimentally by observing changes in shock strength as a function of sample thickness, or by direct measurement of the wave profiles[28,29].

In the case of elastic-plastic flow Grady[28] has pointed out the notable experimental fact that for a wide variety of materials the rise time of the plastic wave (in a two-wave profile) appears to be inversely proportional to the fourth power of the Hugoniot stress. Using this empirical fact Swegle and Grady[29] developed a

phenomenological description of the shock process in which the strain rate, $\dot{\epsilon}$† is related to the deviatoric viscous stress, s_v,‡ in the manner, $\dot{\epsilon} \propto s_v^2$. The effective viscosity η, which is the ratio of stress to strain rate, therefore scales with strain rate as $\eta \propto \dot{\epsilon}^{-\frac{1}{2}}$. (With Newtonian viscosity $\eta = constant$, and wave rise times are invariant with respect to stress levels.) Numerical modelling [29,30] using this phenomenological description of the viscous processes has successfully described wave profiles (of plastic waves) for a wide variety of materials and stress levels. Moss[31] has since derived the fourth power dependence of strain rate on Hugoniot stress using plasticity theory. He notes that $\eta \propto \dot{\epsilon}^{-\frac{1}{2}}$ follows from a theoretical dislocation model of shear deformation in solids, thus providing the beginnings of a theoretical foundation for the microscopic processes leading to these results.

Most types of solid-solid phase transformations require a finite time to take place. In static experiments, near equilibrium, this can sometimes take hours or more. Shock fronts provide situations much further from equilibrium, and phase transformations can take place within the short time it takes the shock front to pass through the material. Theoretical understanding of shock-induced phase transformations is not complete. Several examples of experiments and calculations have been discussed by Duvall and Graham[22] in their review. In particular, one general phenomenological approach that has been used with some success has been refined by Andrews[32], and Hayes[33,34]. The method is based on constructions of the Gibbs free energy, G, of the pure phases. It can be extended to include non-equilibrium mixtures. In this case the reaction between two phases proceeds according to, $dx/dt \propto (G_1 - G_2)/\tau$ where x is a mass fraction, $G_1(V,T)$ and $G_2(V,T)$ are Gibb's free energies of the pure phases and τ is a characteristic time associated with the

† The strain is $\epsilon = 1 - V/V_0$ and the strain rate is $\dot{\epsilon} = d\epsilon/dt$.

‡ The deviatoric stress tensor is, $s_{ij} = \sigma_{ij} - (\sigma_{kk}/3)\delta_{ij}$. The deviatoric viscous stress is the longitudinal component of s_{ij}, i.e. the component directed normal to the shock front.

transformation process. Generally τ has to be determined empirically by fitting the model to experiment. The method has met with success in describing shock-induced transformation in bismuth[32,33,35]. However, Hayes, applying the same theory in a detailed study of polymorphic transformation in KCl[34], found that the transformation proceeded with two different rates: when shocked the material intially transformed to partial completion at a very high rate (instrument limited); subsequent equilibration proceeded at a slower (measureable) rate which depended on the crytallographic orientation of the sample with respect to the shock direction. This implied that two different modes of transformation are involved, and that the phenomenological model was not adequate to describe the experiment. A critical assumption of the phenomenological model of transformation is that the shocked layers are at all times homogeneous in temperature, pressure, and particle velocity. These assumptions, as well as others not mentioned here, may not apply to the silica system under shock, as will be described below.

In summary, the existence of time dependent effects associated with phase transformations is generally accepted; however, details of shock induced phase transformation kinetics are still not well understood in a general fashion. Time dependent effects appear to be important in the experiments described in this work. The situation in fused silica is further complicated because both elastic-plastic flow and phase transformations are involved in the shock compression process. (This will be elaborated upon below.) A detailed theoretical treatment including rate dependent effects is beyond the scope of this investigation.

2.3 High Pressure properties of silica

The silica (SiO_2) system is among the most complicated and interesting materials studied at conditions of high pressure and/or high temperature. The low pressure phases of SiO_2 are of sufficient importance to the ceramic and refractory industries that extensive research and knowledge were already complete nearly

a century ago; there is much information in the general reference by Sosman[36]. Figure 2-4 shows a schematic phase diagram of silica illustrating various known phases, taken from the book by Hummel[37]. α- and β-quartz, α- and β-cristobalite, and trydimite, are all low pressure variations of the SiO_2 system, and are distinguished by different crystal structures, densities and other physical constants.

At standard conditions α-quartz is the stable phase. Some of the phase boundaries, especially those involving the tridymite phases, are not well established because extremely slow reaction rates between different phases makes it difficult to establish thermodynamic stability. The slow reaction rates allow many phases to exist as metastable states outside their stability regions. Both fused silica and cristobalite are metastable at room temperature; they are obtained by supercooling from temperature-pressure regions where they are stable. The physical properties of fused silica most resemble those of the cristobalite phase, i.e. density, refractive index, thermodynamic constants and also in its short range microscopic structure[38].

The high pressure phases known as coesite[39] and stishovite[40] were discovered relatively recently by static loading methods. In these methods samples of SiO_2 are compressed in a static press and simultaneously heated to temperatures ranging from 500 K to 1500 K for a period of many minutes to hours duration. The samples are then cooled to room temperature while still under pressure. After this, the pressure can be released and the sample studied. Both of these high density modifications are metastable at room temperature and pressure. Coesite is the stable phase at a transformation pressure of 2.6 GPa[41] and temperature of 500 K. Stishovite requires pressures greater than 8.5 GPa[42]. Both coesite and stishovite have been recovered in nature from meteorite impact craters[43,44]. However, only stishovite has been recovered from shock experiments, but not coesite[22]. The activation energy for the transformation process is apparently fairly high since the transformation rate is "sluggish" at the elevated temperatures needed[41,42]. For

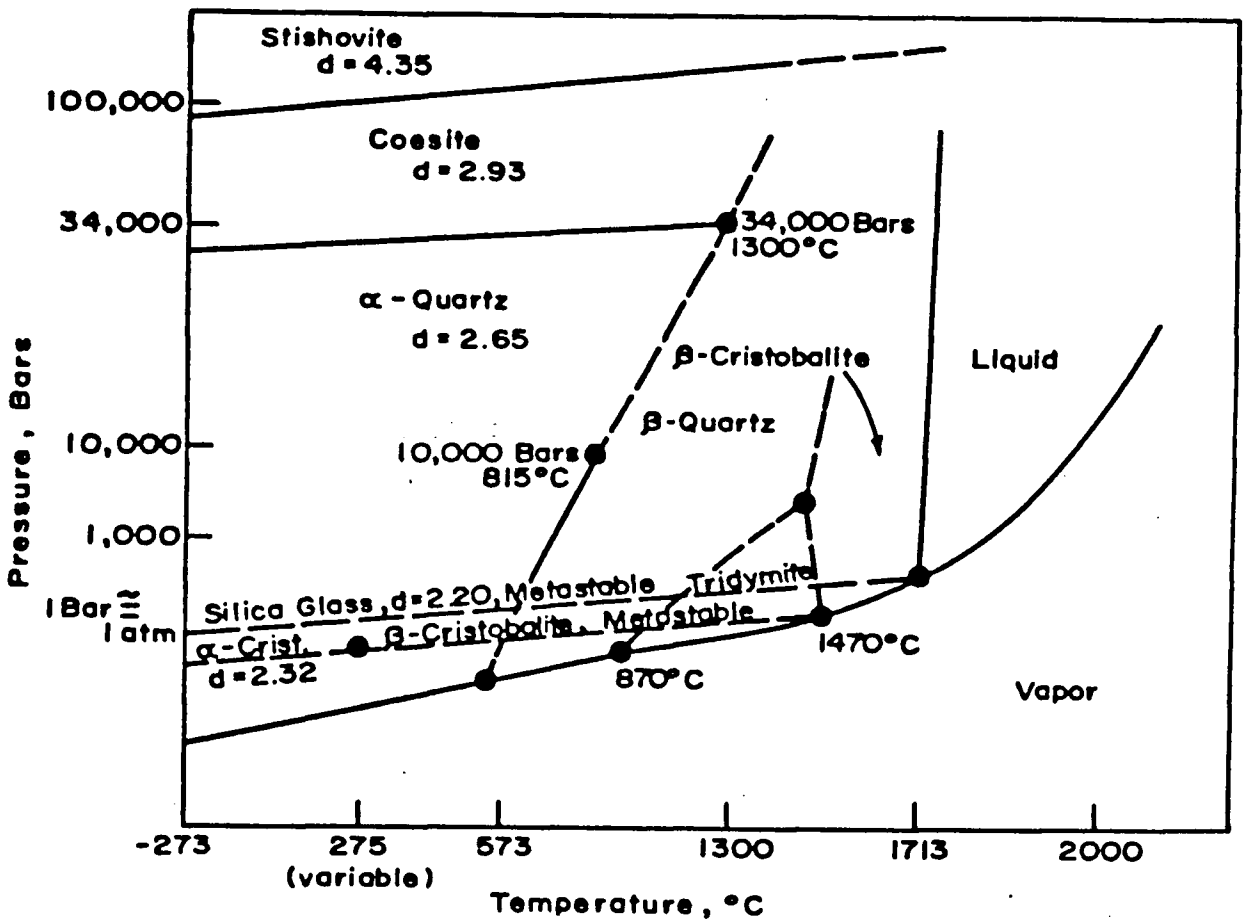

Figure 2-4 Phase diagram for SiO_2 [taken from Hummel[37], Figure 2-5]. The scales are only schematic representations; dashed curves indicate postulated phase boundaries or metastable states.

shock compression experiments stishovite is the most interesting phase since it is believed to be the end state for the SiO_2 system at high pressure. Table I summarizes some experimentally determined properties of SiO_2 in the α-quartz, fused silica, and stishovite forms at standard conditions (zero pressure). The symbols used in this table represent density, ρ, bulk modulus, K, and longitudinal (elastic) sound speed v_p. The two values of v_p for α-quartz correspond to the two principal axes of the crystal structure; for stishovite only an average value (from a polycrystalline sample) was measured. Also indicated is the crystal structure.

Table I. Properties of fused silica, α-quartz and stishovite

Phase	ρ (g/cm^3)	K (GPa)	v_p (km/s)	Structure
Fused silica	2.20	36.9[a]	5.97[b]	amorphous
α-quartz	2.65	36.4[c]	5.70[d] 6.36[d]	hexagonal
Stishovite	4.29[e]	345[e]	11[e]	tetragonal (rutile)

a Kondo *et al.*[61]
b Gray[45]
c Jorgensen[46]
d Mason[47]
e Mitzutani *et al.*[48]

All the low pressure phases of SiO_2, as well as coesite, have a tetrahedral bonding structure between the Si and O atoms giving a coordination number of four for the Si atom. Stishovite is different, as X-ray measurements reveal it to have the rutile structure with a coordination number of six. The higher coordination number affords denser packing of the lattice to give the significant density difference between the low pressure and high pressure phases.

Although fused silica is not thermodynamically stable it is a common form of the SiO_2 system at standard conditions. Static compression of this material

has attracted special interest. It undergoes an irreversible process under pressure termed "densification", in which samples of fused silica can be compressed to stable densities (upon pressure release)[49] reaching 2.65 g/cm^3, close to that of α-quartz. Densified silica has been recovered from shock experiments on both α-quartz and fused silica[50]. The structure of the densified silica is completely amorphous. The microscopic mechanism for this appears to be connected with a general shift in the average Si-O-Si bond angle and a shortening in the Si-O bond length to afford a denser packing of the amorphous lattice[51].

2.4 Shock compression of SiO_2

Shock compression experiments on SiO_2 are usually performed from one of two possible starting states: that of fused silica, and that of α-quartz. The first detailed study of SiO_2 under shock compression was due to Wackerle[52]. This data has since been extended by other workers[53–57]. A number of interesting properties of SiO_2 were revealed. Both fused silica and α-quartz were found to support a two-wave structure indicative of elastic-plastic flow or a phase transition. The Hugoniot elastic yield stress for both materials was found to be remarkably high - about 10 GPa. (In α-quartz shocks oriented along different cystallographic axes give different elastic limits.) Note that this value is similar to, or larger than, the static transition pressure for stishovite. For loading pressures larger than this the material appears to suffer a sudden loss of strength and undergoes significant compression up to densities $\sim$ 4.5 g/cm^3 which is around a factor of two. For pressures above $\sim$ 40 GPa both α-quartz and fused silica have similar Hugoniot curves on the p-V plane. A plot of the experimental Hugoniot curves on the p-V plane is shown in Figure 2-5 using data from several authors. The apparently common curve for the high pressure states on the p-V plane suggests that a common high pressure phase is obtained from the two initial states. McQueen *et al.*[58] have identified this high pressure phase to be stishovite. This identification is based on the similarities of

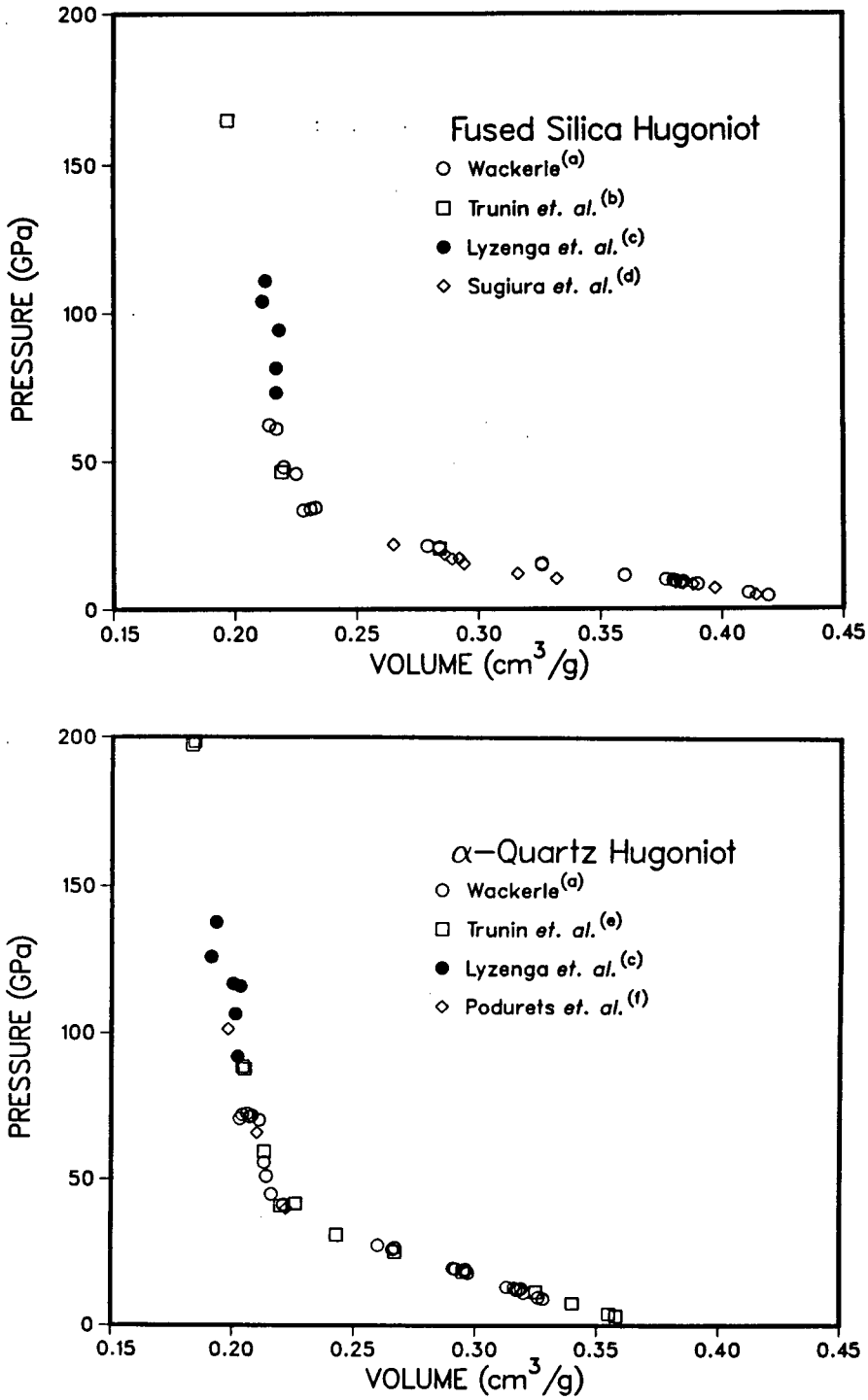

Figure 2-5 Shock Hugoniot measurements for fused silica and α-quartz. Data from several sources is indicated: (a) Wackerle[52]; (b) Trunin *et al.* ref 53 ; (c) Lyzenga *et al.*[54]; (d) Sugiura *et al.*[55]; (e) Trunin *et al.*[56]; and, (f) Podurets *et al.*[57].

the observed transition pressures and volumes between shock compression and static compression data. Using only Wackerle's shock data and the known zero pressure density of stishovite, McQueen *et al.* inferred a transition energy between the quartz and stishovite phases, $E_{tr} \sim 1.5$ MJ/kg, and a bulk sound speed for the stishovite phase, $c_0 \sim 1.0 \times 10^6$ cm/s. Calorimetric measurements have since found $E_{tr} \simeq 0.80$ MJ/kg[59].

In fused silica the wave profiles for the elastic precursor exhibit another interesting feature. This is a gradually increasing foot followed by a shock transition to the yield stress[52,60]. This behaviour is attributed to an anomalous increase in the compressibility with stress ($\partial^2 p/\partial V^2 \leq 0$) up to stresses of $\sim$ 3.6 GPa, and has been observed in a variety of glasses in static compression measurements as well[61]. Barker and Hollenbach[60] have made precise measurements of these profiles, and have exploited this property to launch ramp waves into other materials. Fused silica has found wide use as a window material in shock experiments on other materials. It has been found to remain transparent at least up to the Hugoniot elastic limit, and its refractive index has been calculated as a function of compression by Setchell[62] using the data from Barker amd Hollenbach[60].

Shock temperatures in both α-quartz and fused silica have been measured by Lyzenga *et al.*[54] These measurements also established more accurate data for the Hugoniot in the pressure range of 50 - 150 GPa. The temperature measurements revealed a melting transition at a pressure of 70 GPa and a temperature of 4500 K. A particularly interesting feature of this transition is that the solid remains in an apparently superheated state for pressures in the mixed phase region. At pressures above the mixed phase region the Hugoniot temperature drops to that of the liquid phase. This behaviour is indicated in Figure 2-9, in the next section, where the measured shock temperatures are compared with theoretical equation of state data.

Both forms of SiO_2 used in shock studies belong to a class of materials identified by Grady[63] as "brittle solids". This class of materials comprise many silicate

minerals, oxides and refractory materials. They are distinct from other solids (e.g. metals) by their extraordinarily high Hugoniot elastic limits and their tendency to suffer a dramatic loss of strength when the HEL is exceeded. Grady suggests that the shock compression process for these materials is not homogeneous, but rather heterogeneous, in which localized planar regions (shear bands) undergo large deformation while the rest of the material remains largely undamaged. This model appears to be supported by experiment. A spatially heterogeneous pattern of luminescence in the form of bands was observed in α-quartz under shock[64,65] near the dynamic yield point ($\sim$ 5 GPa for x-cut quartz); and, a spotty pattern in fused silica[66] (also near the yield point). The radiation emitted is also strongly non-thermal: characterized by non-Planckian band emission, high effective temperatures and low emissivity, as would be expected for a heterogeneous process[65,66]. Heterogeneous deformation is also evident in shock recovery of α-quartz in which planar features (lamellae) have been identified[44]. As the pressure increases the degree of heterogeneity decreases. Heterogeneous deformation is most important at moderate pressures ranging from the HEL to a few times the HEL. At very high pressures the deformation becomes homogeneous and radiation emission approaches a blackbody form with emissivity approaching unity.

Other evidence for heterogeneous deformation in SiO_2 can be seen by examining the Hugoniot curves. For both fused silica and α-quartz the stishovite transformation appears to set in just above the HEL and near the appropriate transition pressure, $\sim$ 10 GPa. But it does not reach completion until shock pressures around 30 GPa in fused silica and 40 GPa in α-quartz, which is many times the equilibrium transformation pressure (of $\sim$ 8.5 GPa). In the intermediate region there is much evidence that the material is in a non-equilibrium mixed phase state, only partially transformed to stishovite. Shock loading and release measurements have been made on fused silica by Chhabildas and Grady[67] and on x-cut α-quartz by Chhabildas[68]. These measurements show that the shock release curves follow much steeper paths

than the Hugoniot in this region. This may indicate that release follows a frozen mixed phase state consisting of fixed fractions of stishovite and quartz phases. Also, for higher pressures (above 40 GPa) the reverse transformation observed in release curves appears to set in around 10 to 20 GPa, which is much closer to the equilibrium transition value. Finally, the existence of a pure stishovite phase on the high pressure branch of the Hugoniot is not entirely certain. At higher pressures (40 - 90 GPa) Podurets *et al.*[69] have inferred a discontinuity in slope between release and recompression curves along the α-quartz Hugoniot from impedance mismatch experiments. They interpret this result to indicate that a pure phase is not achieved.

Non-equilibrium or relaxation effects have been observed in several experiments on SiO_2. Wackerle[52] found that the strength of the elastic precursor in α-quartz tended to decrease with increasing sample thickness at the same load stress; similarly, an increase in the apparent elastic limit with increasing load stress at constant sample thickness was also observed. This behaviour has been studied in detail by Ahrens and Duvall[70] for Arkansas novaculite (a naturally occuring polycrystalline α-quartz mineral). Cagnoux[71] has reported a similar stress relaxation behaviour in borosilicate glass samples stressed above the HEL. In these types of measurements the relaxation was observable on μs time scales and cm length scales. Other aspects of non-equilibrium processes have been inferred at higher pressures. Notably, the measurements of shock melting by Lyzenga *et al.*[54] indicate that a metastable superheated solid state is achieved at the shock front in the vicinity of the melt transition. Lyzenga[72] believes that an equilibration time of 10^{-9} s or longer is necessary in order to explain this superheating phenomenon. In the same series of measurements Lyzenga *et al.*[54] have reported a quasi-periodic luminescence signal in fused silica shocked to 73 GPa; this is at the onset of melt transition and suggests an instability associated with the transition occurs at the shock front.

2.5 SESAME equation of state models

The SESAME data library[73], from the Los Alamos National Laboratory, provides equation of state and other material properties in tabular form on a temperature and density grid. This data is generated from a combination of theoretical models and known experimental data to give an accurate representation of the material properties over a wide range of parameter space. Computer programs for retrieving the tables and interpolating between grid points are also provided with the data. The data and associated computer programs are available on request from the Los Alamos National Laboratory.

Three SESAME tables representing the equation of state of SiO_2 are available, and were used in the computer simulations of experiments presented in chapters 4 and 5. The tables are identified by numbers, namely 7380, 7381 and 7382. Tables 7380 and 7381 were designed for fused silica with initial density 2.2 g/cm^3, while 7382 is appropriate for α-quartz with initial density 2.65 g/cm^3. Partial documentation for these tables is available in reference 74 which gives a summary of the equation of state (EOS) tables available and a brief description of the methods used in generating them. A summary of the physical models used in calculating each of these tables is presented briefly below.

Table 7380 is "undocumented"[74], however, it was "probably generated"[74] using a method called the Barnes-Cowan-Rood procedure. Briefly, this method involves generating a cold curve based on a modified Morse potential[75] which has free parameters that allow matching to known material properties at low pressures, and to a Thomas-Fermi-Dirac (TFD)[76] cold curve at high pressures. Because of the stishovite phase transition the cold curve was actually obtained from two separate modified Morse potential calculations. These were joined at the known transition point as determined from Hugoniot data. Thermal nuclear contributions to the pressure (lattice vibrations) were calculated with the Debye model[77], which requires knowledge of the Grüneisen parameter as a function of density. The low temperature

EOS (below 1 eV temperature) is composed of the cold curve and the thermal nuclear contribution. In the region of expanded densities (less than solid) and low temperatures a virial series EOS was used[78]. Coefficients in the virial expansion were determined by matching onto the thermal pressure and density derivative of thermal pressure at the reference density. The high temperature part (above 1 eV) was added by shifting the TFD EOS so that the 1 eV isotherm would match the low temperature model. For the TFD part of the model an average atomic weight of 20.028 and atomic number of 10 was used.

Table 7381 is very similar to 7380, although it was generated with a slightly different procedure. The cold curve was obtained from a special kinked Hugoniot fit to simulate the effect of the stishovite transition. At very high pressures this was matched onto a TFD cold curve. The thermal electronic component of the pressure was obtained by mixing TFD EOS models for silicon and oxygen. The pressure contribution due to thermal nuclear motion was calculated with the Debye model for the solid and interpolated to an ideal gas in the high temperature limit.

The EOS for α-quartz in table 7382 was based on a set of five theoretical models, each valid in different regions of temperature-density space. It was calculated by F. Ree and is documented in detail in reference 79. The individual models used in this EOS were: 1) TIGER[80], for the low density low temperature region where ionization is neglible, and the system can be regarded as a heterogeneous mixture of dissociation products as well as liquid and solid phases of SiO_2; 2) GRAY[81], where the liquid, α-quartz and stishovite phases are modelled within a self-consistent framework developed by Grover; 3) OCCIPITAL[82], the high temperature low density region where the SiO_2 molecule is completely dissociated into a plasma and can be modelled with a Saha equation (ideal gas); 4) TFCMIX[83], the Thomas-Fermi theory with Kirzhnits correction for modelling the high temperature-high density region; and, 5) MASTER[84], which attempts a phenomenological correction at low

temperatures and low compression to account for atomic shell structure and electronic correlation effects. Figure 2-6 indicates the regions of temperature-density space where each of these models is expected to be valid.

Comparison of Hugoniot curves calculated from these EOS tables with the experimental Hugoniot data is shown in Figure 2-7 for the fused silica data and Figure 2-8 for the α-quartz data. The Hugoniot is shown both on the D-u plane and on the p-V plane. As can be seen for the fused silica tables, 7380 and 7381, both versions appear to fit the Hugoniot data quite well. Greater detail was used in modelling the stishovite transition for table 7380 than for 7381, and the fit appears to be superior in the mixed phase region. Also the high pressure branch from the 7380 table appears to fit the data slightly better. The comparison between table 7382 and the α-quartz data is not as accurate. The main reason for this is because no attempt was made to tailor the EOS to the experimental details of the α-quartz to stishovite transition. Thus the transition appears smoothed out in the calculated EOS. In addition, Ree[79] notes that the predicted Hugoniot is "soft" above 100 GPa (see Figure 2-8). These discrepancies arise in spite of the fact that, due to the more rigorous physical models employed, this EOS is probably the most realistic one over the very wide region of density-temperature space for which the data is tabulated. The source of these errors lies primarily in the difficulties of joining together the various theoretical models used in the calculation. In contrast, a more empirical procedure using the experimental details as an input, was applied in generating tables 7380 and 7381; thus, it is no surprise that these tables appear to fit the data more accurately.

Calculated shock temperatures along the Hugoniot are compared with the data of Lyzenga *et al.*[54] in Figure 2-9. The models used for generating tables 7380 and 7381 do not include a melting transition. Melting was included in table 7382, but due to a relatively coarse distribution of grid points its effects along the calculated Hugoniot are barely discernable. As can be seen in the figure the calculated

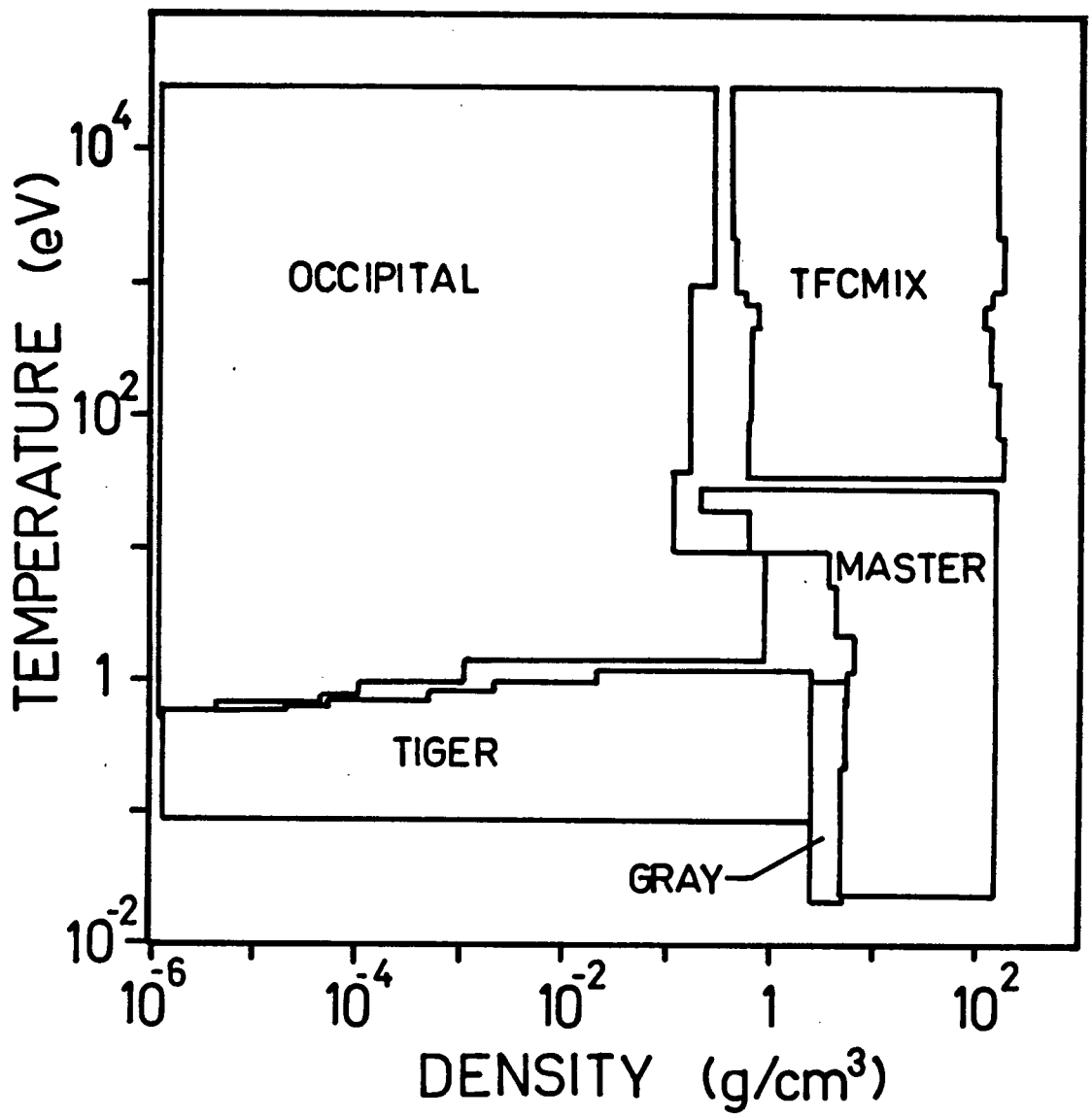

Figure 2-6 The density-temperature ranges of the five computer models for the SiO_2 system used to calculate SESAME table 7382. (From F. Ree[79].)

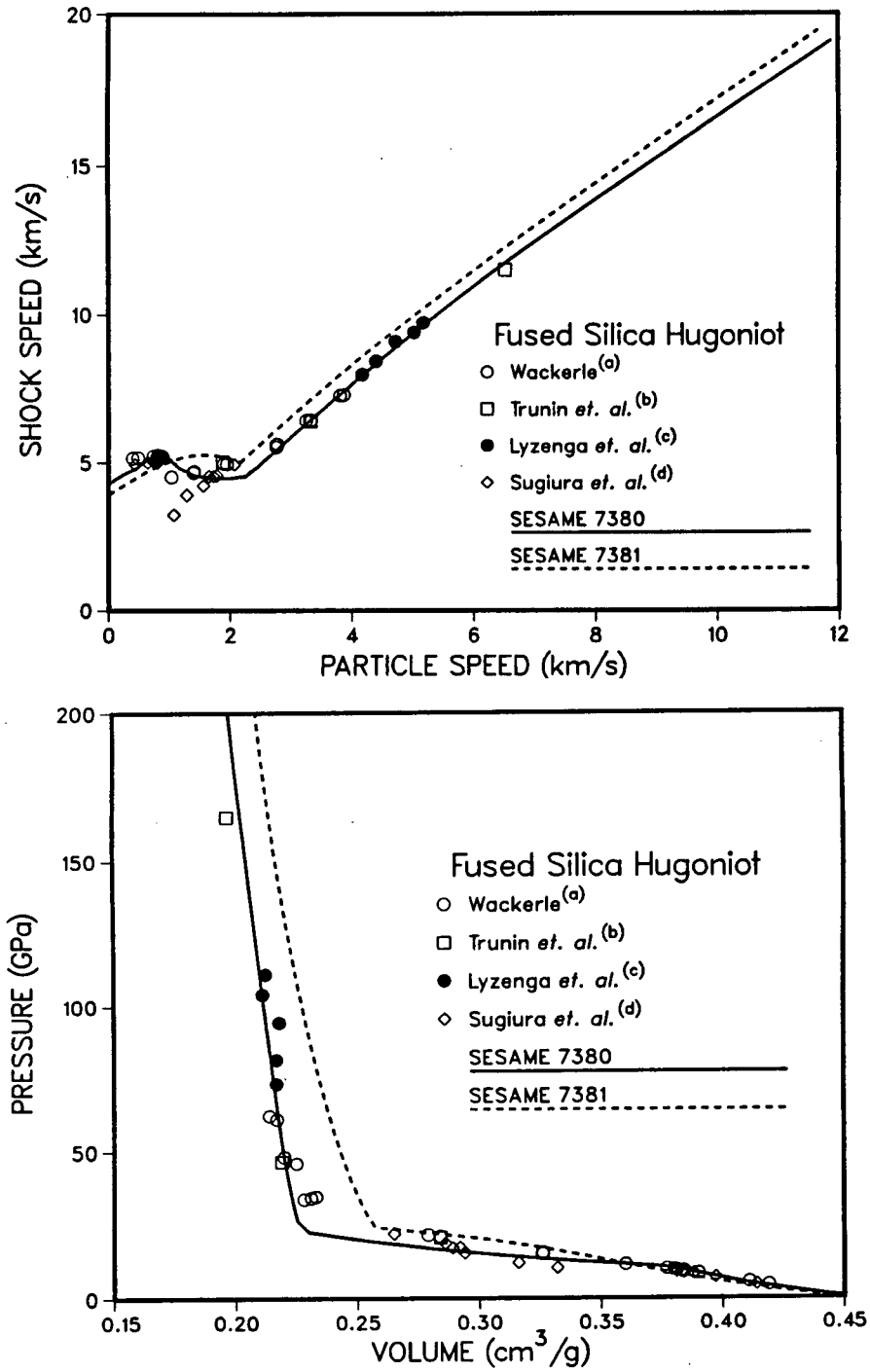

Figure 2-7 Comparison of fused silica Hugoniot data with SESAME tables 7380 and 7381. In the upper figure data is plotted in the D-u plane; in the lower figure it is plotted in the p-V plane. Data from several sources is indicated (same as Figure 2-5): (a) Wackerle[52]; (b) Trunin *et al.*[53]; (c) Lyzenga *et al.*[54]; (d) Sugiura *et al.*[55]

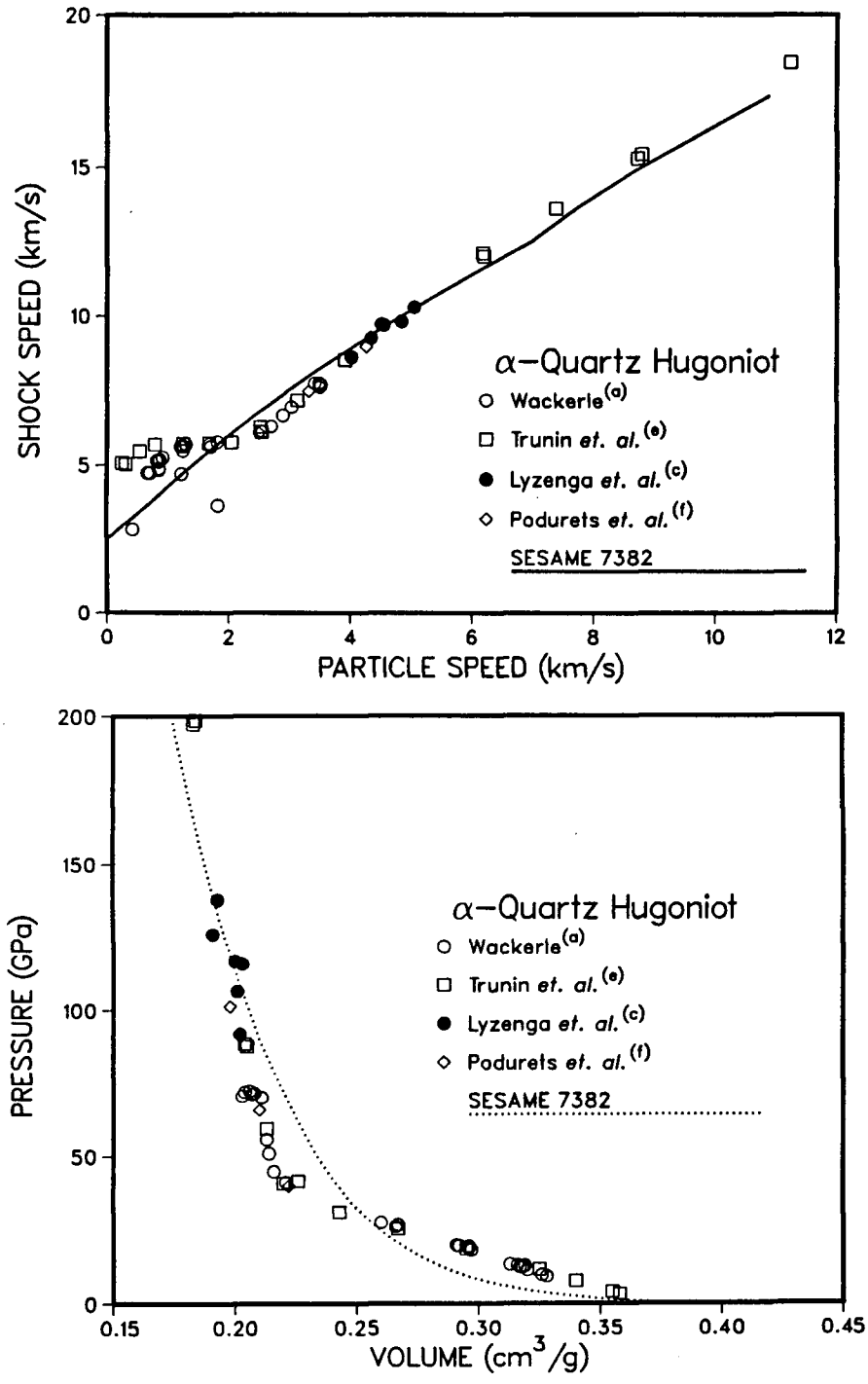

Figure 2-8 Comparison of α-quartz Hugoniot data with SESAME table 7382. In the upper figure the data is plotted in the D-u plane; in the lower it is plotted in the p-V plane. Data from several sources is indicated (same as Figure 2-5): (a) Wackerle[52]; (c) Lyzenga *et al.*[54]; (e) Trunin *et al.*[56]; and, (f) Podurets *et al.*[57].

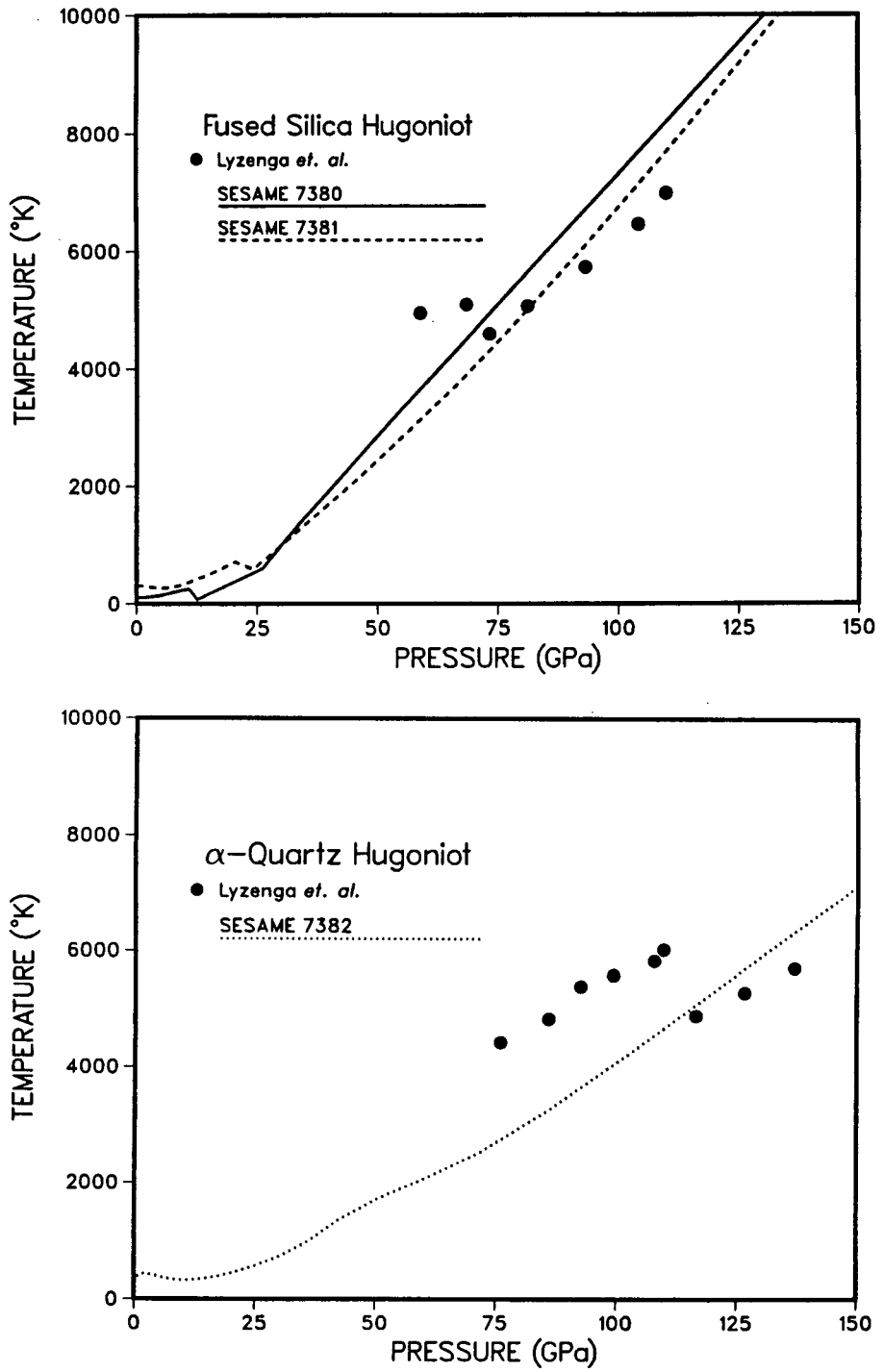

Figure 2-9 Shock temperatures along the Hugoniot. Data from Lyzenga *et al.*[54] is represented by the solid circles. Curves are from SESAME Hugoniots are indicated.

temperatures are fairly realistic and nearly agree with the measured temperatures for the liquid phase at pressures above $\sim$ 100 GPa. It should be noted that Lyzenga *et al.* believe the Hugoniot temperature measured at the onset of melting does not reflect an equilibrium state, but rather represents the temperature of a metastable supheated solid stishovite state. Nevertheless, the measured temperatures appear to lie significantly above the calculated values at pressures below the melting transition (i.e. $\leq$ 70 GPa for fused silica, and $\leq$ 110 GPa for α-quartz). This is probably an inaccuracy in the heat capacity used in generating these tables. Lyzenga *et al.*[54] fit their measurements to a Mie-Grüneisen equation of state using an empirical heat capacity with a linear temperature dependence.

A number of comments are in order regarding the use of these EOS tables for modelling the experiment. An equation of state, by definition, represents the state of a material in thermodynamic equilibrium; consequently, non-equilibrium effects lie outside of this type of description. This implies that phase transformation are always in equilibrium, and that all stresses are purely hydrostatic (shear components are neglected). Both of these assumptions are probably not well approximated in reality as experiments with SiO_2 have shown that the interrelated phenomena of elastic yield and the stishovite transformation process under shock may produce material states that are quite far from thermodynamic equilibrium, but metastable. Nevertheless, the Hugoniot curves appear to be well-defined, and allow construction of an EOS description. These problems are probably most severe at lower pressures where shock heating produces insufficient thermal energy to overcome metastable equilibria, and where the elastic limit of the material is significant compared to the driving stress. These effects lead to the non-equilibrium phenomena, such as stress relaxation behind an elastic wave, or similar thermodynamic relaxation within a shock induced phase transformation which cannot be modeled since they require descriptions beyond the scope of the standard hydrodynamic equations coupled with an EOS description. As noted above, some of these effects appear to occur

in conventional shock measurements with macroscopic samples – i.e. where the measurement scales are significantly larger than the several nanoseconds and few tens of microns characteristic of the experiments described in this work.

2.6 Isentropic compression of SiO_2

SiO_2 is of great interest to geophysicists because it is a major constituent of the Earths crust and mantle. Since the discovery of stishovite, various researchers have found that the stishovite transformation serves as a prototype for similar transformations (with similar transition pressure and volume change) in many minerals of geophysical interest[85]. This has provided important experimental corroboration of theoretical models of the Earth's interior[86].

The possibility that the Earth's core could be a dense metallic phase of silica was proposed by Ramsey[87] in 1948. This hypothesis had been considered seriously by geophysicists until experimental data and theoretical advances became available either to corroborate or disprove it. Thus one of the major motivations for shock compression studies of SiO_2 to extreme pressures (many megabar†) was the possibility of discovering further high density modifications of SiO_2 beyond stishovite, with the intent to probe larger depths in the Earth (higher pressures)[56]. However, the Hugoniot for SiO_2 does not show any further density jumps. It is generally accepted that the Earth's core is mostly Fe; shock wave and other high pressure measurements have yielded data that is consistent with independently determined geophysical constraints (such as density and sound speed).

Because of the substantial volume change required to obtain the stishovite phase from the initial state in shock experiments much of the energy deposited in the material contributes to heating of the sample, and increasing the thermal contributions to the pressure, while not compressing the material much more. If an unknown higher density phase of silica were to exist at Mbar pressures and lower

† 1 Mbar = 100 GPa

temperatures it is quite possible that the Hugoniot may not pass near the region of stability for this phase because of the high temperatures. A compression method which avoids heating the sample by shock would follow an isentropic path and may effect the transformation to such a new phase, whereas shock compression to the same pressure would not. (Equivalently one might perform shock experiments from the high density initial state of stishovite; however, macroscopic quantities of stishovite are not available.) This rationale led Pavlovskii *et al.*[88] to perform isentropic compression experiments on α-quartz samples using a magnetic implosion generator. Remarkably, their results indicated that quartz transforms to a new dense phase with $\rho \sim 10$ g/cm^3 at a transition pressure of $P_t \sim 125$ GPa – this density-pressure combination is nearly exactly that inferred for the Earth's core-mantle discontinuity by independent means.

This result has not been confirmed experimentally or theoretically. An earlier experiment by Hawke *et al.*[89] using a similar implosion technique obtained a single data point for isentropically compressed fused silica at $\rho \sim 6$ g/cm^3 and $P \sim 500$ GPa. Fritz and McQueen[90] performed double shock experiments on quartz to 150 GPa and did not observe the volume collapse, although their study was by no means exhaustive. Experiments with diamond anvil cell techniques[91] to 200 GPa have also not displayed any evidence of the expected metallization. Finally, this question also motivated a theoretical band structure calculation by Carlsson *et al.*[92] for SiO_2 in the eightfold coordinated CaF_2 structure; the calculation did not yield the required density.

The possibility that a degree of isentropic compression exists in the laser-driven shock experiments presented in this work is pointed out in the theoretical calculations to be described in chapter 4. A possible interpretation of the experimental findings presented below is consistent with the volume collapse observed by Pavlovskii *et al.* Further discussion of this, as well as problems with the interpretation, will be presented in chapter 5.

CHAPTER 3

EXPERIMENT

3.1 Introduction

A description of the laser facility and associated diagnostic equipment used to obtain the experimental data is given in this chapter. Following this the experimental technique for measuring shock trajectories is described. Some representative raw data is displayed and the analysis method is described. Preliminary interpretations of the data are then made.

3.2 Laser facility

The laser facility is the same as that used for previous work[11,12,93–95], and a diagram of the laser chain is shown in Figure 3-1. It consists of a Nd-YAG/Nd-glass laser chain with a second harmonic generation crystal, beam steering optics, vacuum chamber, focussing lens and associated beam monitoring diagnostics to record the incident pulse shape and energy. The laser chain consisted of a Nd-YAG oscillator and preamplifier followed by two Nd-glass amplifiers. The rod diameter in the last amplifier was 25 mm. The oscillator was passively Q-switched with a dye cell and produced a gaussian pulse of 2 ns FWHM (nominal) at a wavelength of 1.064 μm in a TEM_{00} spatial mode. The output beam energy could be varied up to 10 J (by varying the amplifier pumping). The 1.064 μm fundamental wavelength was converted to 0.532 μm with a KDP type II conversion crystal. Output energy at

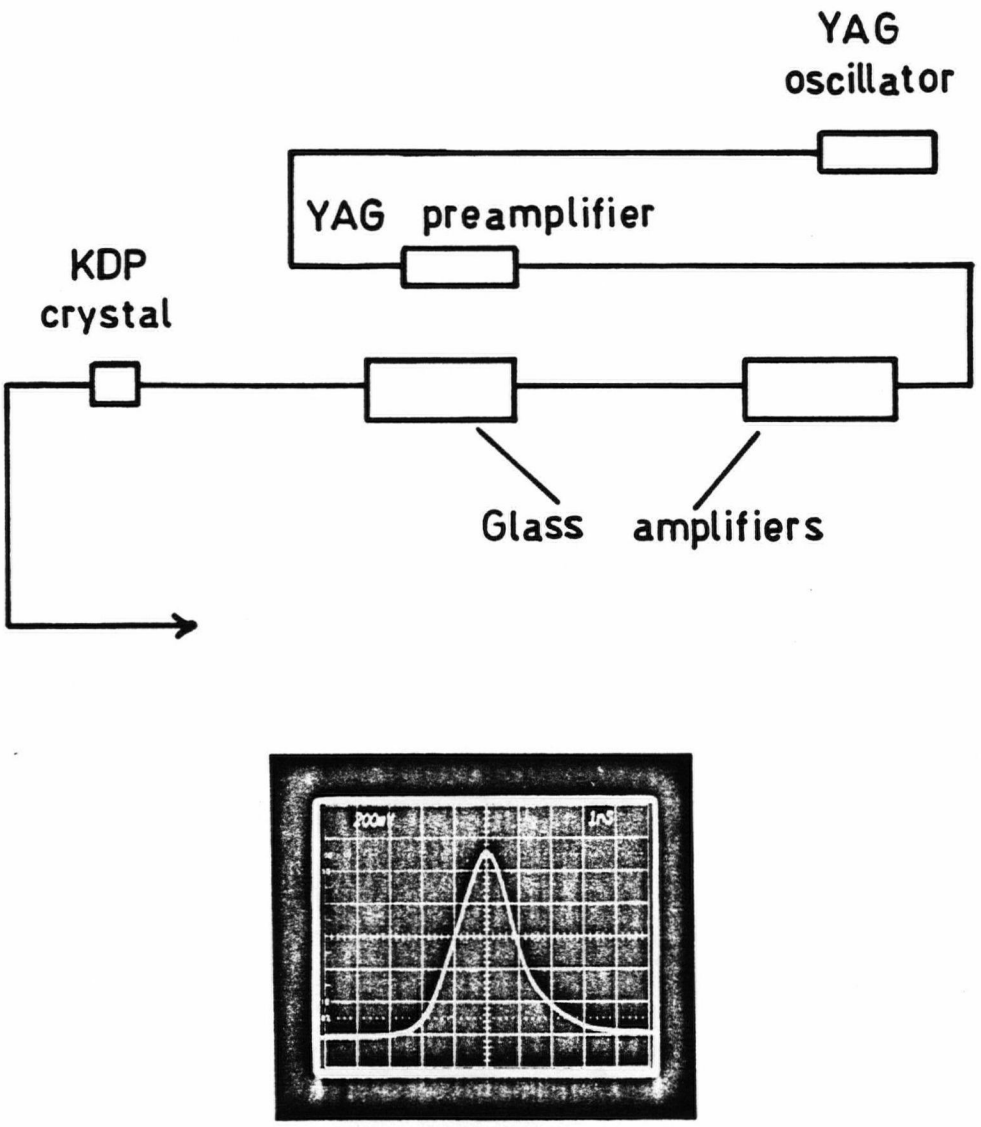

Figure 3-1 Schematic of the laser chain used in the experiments, and a typical laser pulse shape.

the 0.532 μm wavelength reached 3.5 J. The beam was steered into the vacuum chamber by a series of 3 dichroic mirrors, and was focussed onto target with a 240 mm (nominal focal length) best-form lens giving an f/10 focus.

The laser could be operated in two modes: high power with all of the amplifiers activated; and, low power with the Nd-YAG oscillator and preamplifier operating alone. The low power mode could be operated at a repetition rate of $\sim$ 0.10 Hz and was used for alignment of optics and subsystems in the experiment.

The laser focal spot was measured for the full range of experimental conditions. This was done by imaging the laser spot with an f/4 achromat onto the streak camera[96] input optics. The streak camera was operated in focus (non-streak) mode, hence was functioning essentially as a video camera to record the intensity distribution. It should be noted that the streak camera had a limited dynamic range ($\sim$ 60) and a non-linear intensity response (which was corrected for) so that the focal spot data presented below gives only a rough idea of the intensity distribution. Thus it is useful for estimating the average size but it is not adequate for resolving fine details. The laser was fired at full energy for the range of amplifier pumping levels used in the experiment. The beam was attenuated with a pair of dichroic mirrors placed in series ahead of the main focussing lens, and also with neutral density (ND) filters placed in the beam path following. The imaging system was focussed and directly calibrated for magnification by placing a grid of known dimensions in the target plane and recording the grid image obtained from the streak camera output. Images of the laser spot were then obtained conveniently in a digitized format from the streak camera output and later analyzed on a mainframe computer.

The target was generally placed at the plane of best focus to obtain a maximum in intensity. However, the laser spot size varied with the amplifier pumping. This was caused by refraction in the amplifier rods due to thermal gradient effects when the amplifiers were pumped. The spot size increased with decreasing amplifier pumping. In this experiment the spot sizes ranged from about 40 μm to 100

μm in diameter. In addition there was a systematic variation in pulse length with pumping level, although this amounted to $\sim 25\%$ over the entire range. Thus, the effective intensity varied due to the combined effects of changes in incident energy, spot size and pulse length as the pumping level was changed. These effects were monitored and taken into account in the analysis. Figure 3-2 shows an example of a contour plot of the laser spot. As can be seen from the figure the spot distribution is peaked and is approximately azimuthally symmetric. The spot intensity distributions were also analyzed into equivalent azimuthally symmetric intensity profiles which are presented in Figure 3-3.

Both the effective intensity, and the spot size are quantities that are difficult to specify for a one-dimensional analysis. The main consequence of this situation is that one-dimensional simulations of experiments have to rely on an empirical prescription to obtain the appropriate intensity for use in modelling the experiment. For a gaussian focus a simple criterion may be to take the peak focussed intensity at the centre of the focal spot to represent the intensity, and the diameter of the contours containing 50% or 90% of the energy (for example) to represent the spot size. In previous work[11,93,94] the method for specifying an average or nominal intensity has been to use the effective intensity Φ_{60} specified by,

$$\Phi_{60} = 0.6 \times \frac{E_{laser}}{\tau_\ell A_{60}}. \qquad [3-1]$$

Here τ_ℓ is the full width at half maximum of the laser pulse shape and A_{60} is the area within the focal spot containing 60% of the laser energy. From the given total energy, E_{laser}, and focal area A_{60} one may construct an equivalent gaussian focal distribution,

$$\Phi_{gaussian}(r) = \frac{(0.92)E_{laser}}{(A_{60})} \exp[-(0.92)\pi r^2/A_{60}]. \qquad [3-2]$$

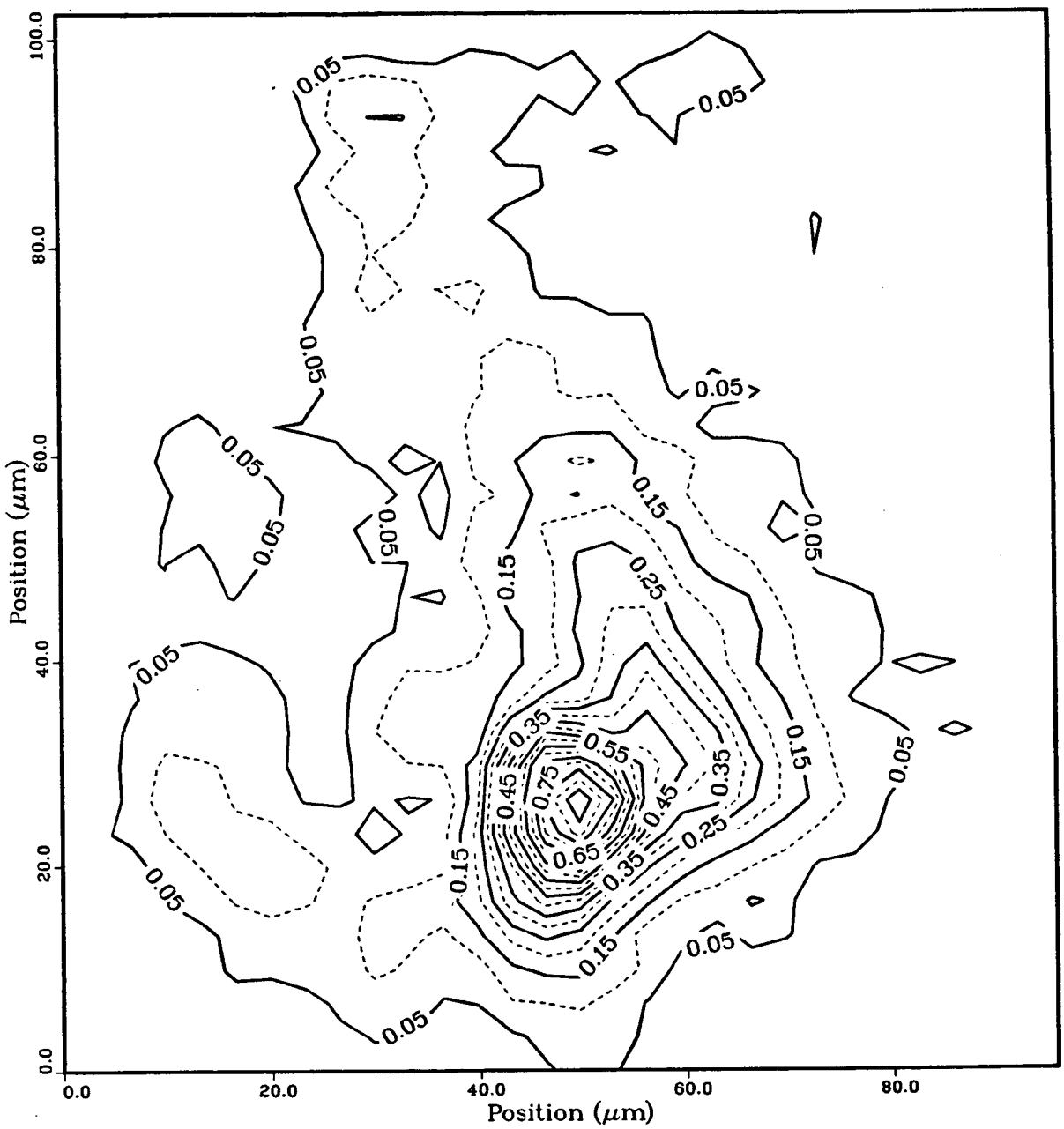

Figure 3-2 Contour plot of the laser focal spot.

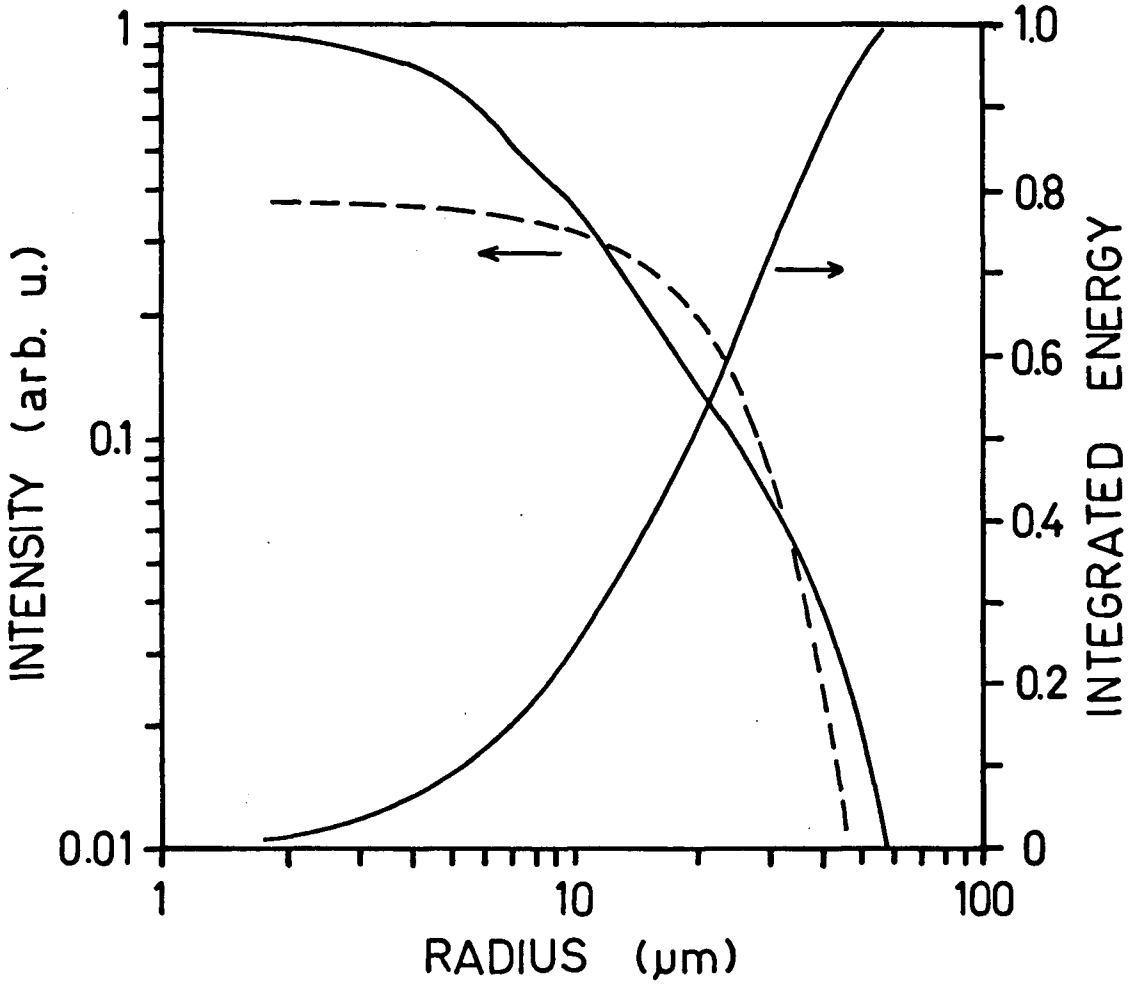

Figure 3-3 Typical intensity profile derived from focal spot measurements. The intensity profile and integrated energy contained within the radius are indicated by the solid curves. An equivalent gaussian profile is indicated by the dashed curve.

Here the parameter r is the radial distance from the centre. This gaussian distribution is equivalent to the measured distribution in that it has the same total energy and focal spot size (according to the 60% energy criterion) as the actual measured spot; an example is shown in Figure 3-3 by the dashed curve for comparison with the measured distribution. It may be noted that the gaussian appears much more uniform than the actual spot, so that the spot can not really be characterized as gaussian. The intensity within the confines of A_{60} varies by up to a factor of three from the gaussian distribution.

The empirical formula [3 – 1] for Φ_{60} has been successfully used to specify the effective intensity in one-dimensional hydrocode simulations of Al target experiments[11]. The predicted ablation pressures and shock trajectories were in good agreement thus providing justification for the use of this formula. Furthermore, shock breakout on the rear side of the foil was observed to be planar within an area roughly equivalent to A_{60}. Further discussion of this problem is given in chapter 5.

3.3 Experimental arrangement

A set of streaked shock trajectories are the subject of analysis in the rest of this thesis. These were obtained using the technique originally demonstrated by van Kessel and Sigel[7]. Figure 3-4a shows the experimental situation in the vicinity of the target. The target consisted of a slab of fused silica[97] of dimensions 1 mm × 25 mm × 75 mm. The edge of the slab was polished to a concave cylindrical curvature of radius ~ 6 mm† and mounted in the target chamber such that the main

† Probe beam light scattered from the corner of the slab obscures the field of view near the target surface. The curved surface blocks these scattered rays through a range of angles whose maximum is determined by the ray tangent to the curve at the corner (for rays in a horizontal plane). The curvature (i.e. the tangent angle) must be such that no scattered light enters the optical system.

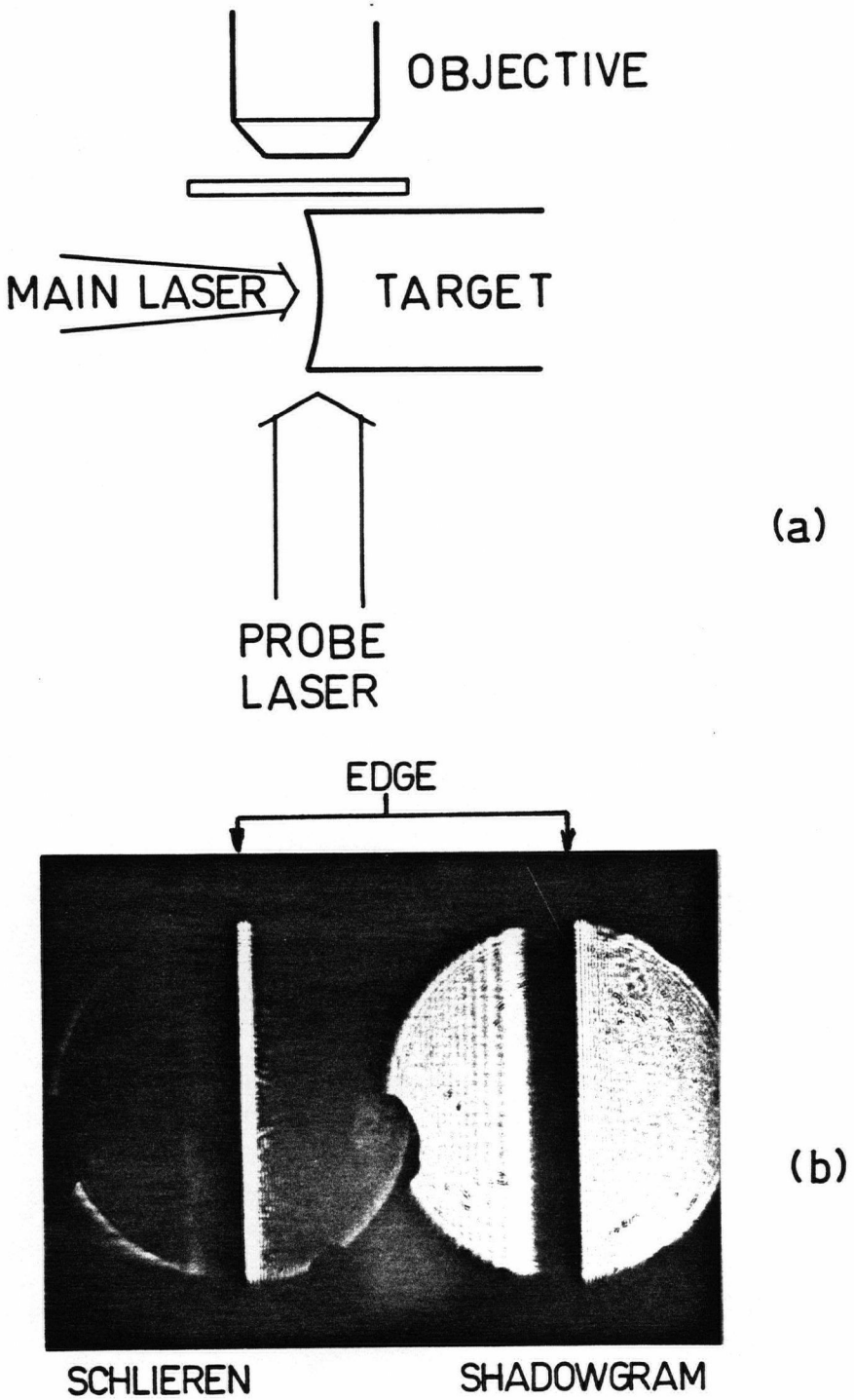

Figure 3-4 (a) Experimental arrangement for obtaining streak shadowgrams. (b) View of the target edge as seen through the imaging optics at the streak camera. In (b) the vacuum is to the left of the edge and the target is to the right.

laser beam was focussed into the centre of the concave region at normal incidence. Since the laser spot was much smaller than the edge dimension of the target this situation approximates a semi-infinite half-space. The shock disturbance propagates from the target edge at a direction normal to the edge orientation. This was viewed from the side using a 10× microscope objective which was protected from target debris by a microscope cover glass.

The concave curvature on the target edge serves to provide an unobstructed view of the region just inside the target surface underneath the laser spot. Note that the laser focal spot size is a small fraction (~ 0.1) of the edge size so that the shock disturbance inside the target does not interact with the sides of the slab during the experimental observation times. Diffraction and scattering of light from the corner of the target cannot interfere with the optical image viewed by the microscope objective since all such light is either reflected or refracted out of the field of view by the curved surface. This arrangement also serves to remove unwanted plasma emissions from view. Such an unobstructed view (of the target interior) is not possible with a square target edge: diffraction fringes from the square corners obscure the interior of the target to significant depths (~ 25 μm). Figure 3-4b shows the appearance of the unperturbed target edge as seen through the imaging optics for schlieren and shadowgram images. In the shadowgram the concavity causes a dark band to be located just ahead of the surface. In the schlieren image the target surface appears as a single bright line in a dark background.

Illumination of the target region was provided with a dye laser (Rhodamine 6G) pumped with a small amount of energy from the main laser beam. The dye laser wavelength was ~ 0.57 μm. The dye laser pulse was lengthened to approximately 12 ns duration using an etalon placed at the output coupler of the laser cavity.

Figure 3-5 shows a view of the experimental arrangement for obtaining the image on the streak camera. The optical signal was relayed through an intermediate

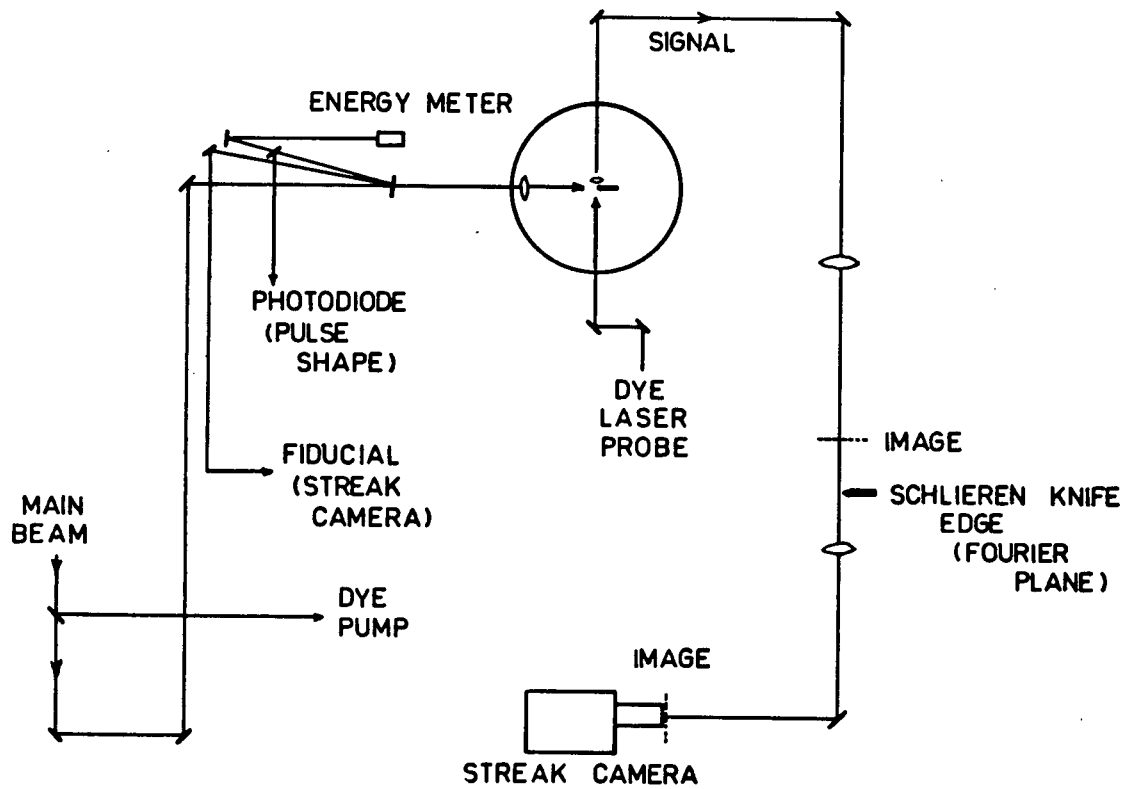

Figure 3-5 Overview of the streak shadowgraphy experimental arrangement.

image plane followed by further magnification onto the streak camera slit. Total magnification of the system was measured at the streak camera slit by placing a grid of known dimensions at the target plane. The magnification was 166 $\pm$ 1; this gave a viewing region of $\sim$ 100 μm along the length of the slit. Image resolution was estimated to be $\simeq$ 3 μm (diffraction limited) which agreed well with the dimensions of the smallest features which were observed at the streak camera image plane. Some shadowgrams were obtained using the schlieren knife-edge technique. The knife-edge was placed at a fourier plane located just ahead of the final relay lens in front of the streak camera slit. For experimental measurements two 100 Å band interference filters centred at 5700 Å were placed in series in front of the streak camera slit to reject scattered light from the main laser or plasma emissions.

Timing reference was provided by a fiducial from the main laser beam which reached the streak camera slit after traversing an optical path nearly equal to the optical path of the probe beam. Absolute timing reference was calibrated by comparing the time delay of the fiducial signal with that of the main beam scattered into the imaging system from the target surface. (This was done with the 5700 Å filters removed.) The fiducial timing accuracy is estimated to be $\pm$100 ps.

Pulse shapes from the main laser were recorded on a photodiode detector[98], as well as on the streak camera fiducial. The photodiode detector provided a more accurate measure of the pulse shape than could be obtained with the streak camera, which had a dynamic range less than 100 and a non-linear intensity response. The pulse shapes were digitized in a format suitable for input to hydrodynamic computer simulations of individual target shots. The laser energy was monitored with a Gentec model ED-200 pyroelectric detector[99] which had been cross-calibrated *in situ* against a Scientech model 364 energy meter[100]. Error in the energy measurement is estimated to be less than 5%.

3.4 Measurement technique

Alignment of the optical system was facilitated by the low power oscillator mode of operation of the main laser. The main beam was aligned to the centre of the target edge by observing the reflection of the low power beam (attenuated by $\sim$ ND 1 filters). Arranging a direct back reflection from the curved surface ensured that the main beam hit the target at normal incidence and at the bottom of the concave surface. This corresponds to the observable "edge" in the optical image (cf. Figure 3-4b). When the low power beam was unattenuated the flux at the target surface was sufficient to cause slight damage, but only in the regions of highest intensity and was observable only after many ($\sim$ 20) repeated shots. Light scattered from the damaged region was then viewed through the imaging optics at the streak camera slit to provide an accurate marker of the laser focal spot position with respect to the slit position. The image could then be aligned easily onto the slit to view the target region directly underneath the focal spot. Accuracy of image alignment with respect to the slit is estimated to be $\pm$ 5 μm. For each new shot the target was moved vertically in its mount to provide a fresh, undamaged region for the experiment.

Before every target shot the target edge position along the length of the slit was identified by streaking the image under illumination of the probe beam but without main beam illumination. The channel number corresponding to the edge position was recorded for future reference.

Examples of the streaked images obtained in the experiment are shown in Figure 3-6. These digitized images were obtained from the streak camera output in a 256 by 256 pixel array. The display was produced on a dot-matrix printer with a 7-level grey scale; the choice of levels and pattern quality is therefore arbitrary to a large extent and the image should only be regarded qualitatively.

Figure 3-6a shows a shock trajectory image obtained using the standard shadowgram arrangement, and Figure 3-6b shows the result from a similar shot obtained

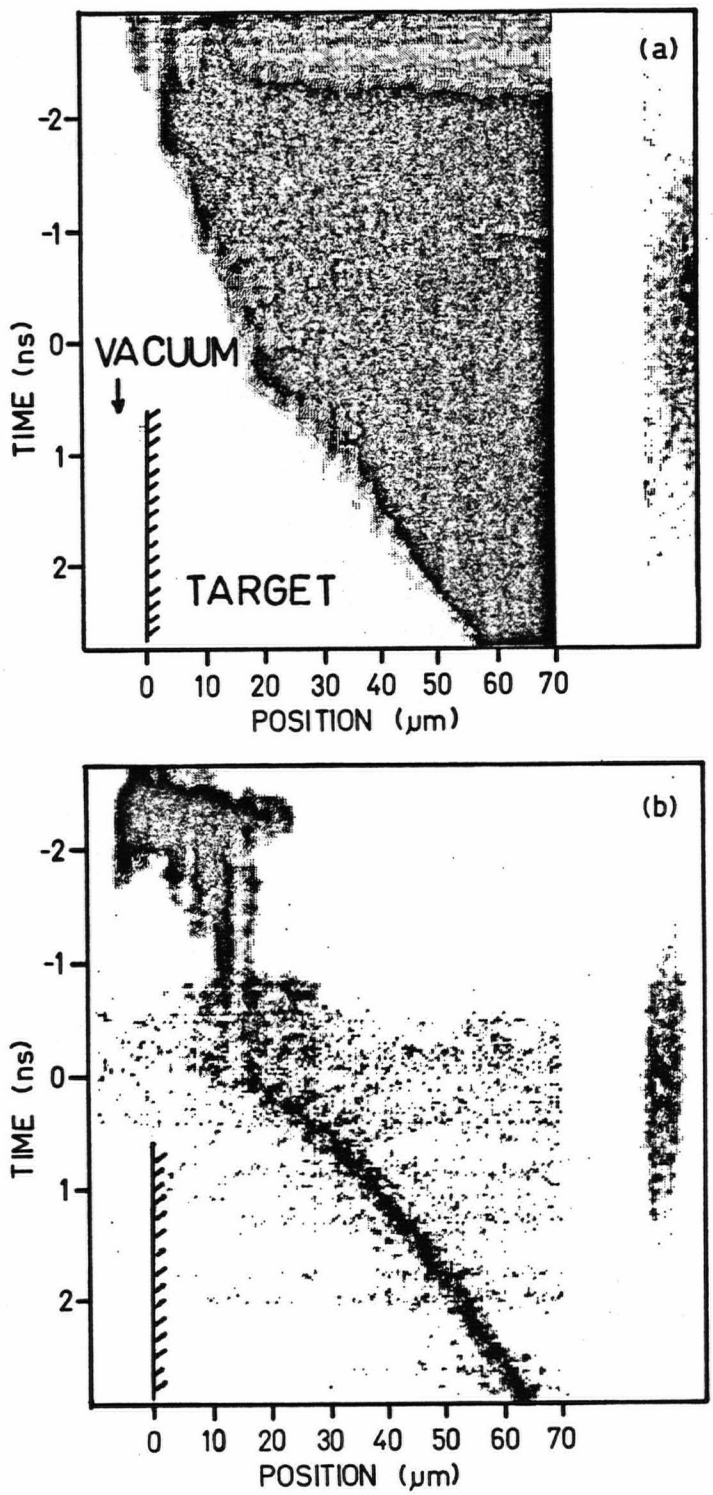

Figure 3-6 Typical streak images displaying raw data obtained from the experiment. (a) Shadowgram image; (b) schlieren image.

with the schlieren arrangement. The space and time scales are drawn such that the spatial origin is located at the edge of the target and and the time origin at the peak of the pulse. The time origin is obtained from the fiducial signal, displayed simultaneously with the data, while the spatial origin is obtained just prior to the main laser irradiation as outlined above.

Interpretation of the shadowgram data assumes that the shock disturbance propagating into the target is sufficiently strong that the material is heated and ionized such that it is rendered opaque to the probe beam. This produces a shadow region behind the shock front through which the probe beam is not transmitted. The boundary is located at the shock front itself, and therefore measurement of the position of this boundary constitutes a measurement of the shock position. With the schlieren technique, the knife edge blocks the central order of the probe beam as well as all of the spectra to one side of the spatial fourier plane. This enhances sensitivity to transmitted scattered light while not allowing unscattered light to produce a signal. If the object in view is opaque, such as a shock-ionized region, the schlieren technique produces a signal only at the boundary (the shock front), where scattering is to be expected; for a very sharp boundary the spatial size of the observed signal is limited by the resolution of the optical system. No signal is produced in regions where there is no scattering or no transmission, i.e. from fully opaque regions or completely unperturbed regions. The schlieren method will also produce a significant signal in transparent regions where there are perturbations in the refractive index, such as would be produced by a weak shock, or other types of weak disturbances. With this in mind, the schlieren data can be seen to provide more information regarding weak disturbances in the target. At early times there appear to be disturbances within the target to a depth of about 20 μm as can be seen from the schlieren signal. There is no narrow feature indicating a sharp boundary from an opaque object. The shadowgram signal confirms that the target is still transparent in this region at early times, because a significant signal is transmitted

through the target. The transparent-opaque boundary is not seen to emerge until $t \simeq -1.5$ ns.

The weak disturbances observed at early times in the laser could be due to early transmission of the laser light at low intensities before the plasma forms, resulting in weak ionization. Also the low pressure elastic wave launched in the silica at early times in the pulse is known to be transparent and could give a noticeable schlieren signal while remaining unobservable in the shadowgrams. In contrast, the signal observed at later times can be clearly interpreted as a strong (ionizing) shock front. This front is seen to emerge, in the schlieren data, at 15 to 20 μm depth within the target. This front also propagates coincident with the optical boundary observed in the shadowgram signal. In summary, although the shadowgram signal may represent the motion of the optical boundary between opaque and transparent regions, this boundary does not appear to be coincident with the leading front of the disturbances within the target until later times when a shock is seen to form clearly in the schlieren signal.

3.5 Data reduction

Most of the data obtained were streaked shadowgrams rather than schlieren images. The schlieren method required the probe beam illumination to be much more intense than for the shadowgrams in order to obtain sufficient signal at the camera; it was not possible to obtain the required intensities reliably for the entire experiment. Since the images were recorded in the form of a 256 by 256 array they were conveniently reduced to a standard representation on a mainframe computer by a simple interactive edge detection program. The program was designed to produce an x-t plot of the shadow boundary normalized to standard units (μm and ns) and appropriately shifted to the origin defined by the peak of the pulse (time

$t = 0$) and the edge of the target (position $x = 0$). This origin was obtained by supplying the known fiducial delay and the target edge position for each shot.

An example of an output from the reduction program is shown in Figure 3-7. The shadow boundary is marked by the triangular symbols. The boundary was detected by a process of differentiation (along the spatial direction) followed by peak detection to locate the rising edge. Noise or ambiguity in the original signal is reflected by the degree of scatter and roughness in the reduced trajectory. Piecewise linear fits along the trajectory were used to estimate the instantaneous slope, hence the velocity; these are indicated by the hexagons with associated error bars. The horizontal bar (temporal uncertainty) indicates the time interval over which trajectory points were included in the fit; and, the vertical bar represents the standard error in the slope for the group of points used in the fit. All points were weighted equally.

Three types of discrete data values were extracted from these trajectory measurements where possible or applicable. Two of these were shock speeds D_f and D_p. The trajectory shown in Figure 3-7 is typical of nearly all the measured trajectories in that the strong shock front which is seen to emerge somewhere in the middle of the pulse is never steady, but is strongly decelerating from a peak value attained seemingly at the moment of formation. The instantaneous speed attained at the moment of formation was recorded and labelled D_p. After several nanoseconds many of the trajectories appear to reach steady propagation speeds (near the end of the measurement). The speed at this point in the measurement was also extracted and labelled D_f. Finally, an estimate of the time period for the deceleration process to take place was made by graphically extrapolating the velocity data points from D_p to D_f as shown in the figure, and measuring the base of the triangle so constructed. This last extraction probably seems crude; a more sophisticated method such as fitting a decaying exponential was tried, but the data was too noisy

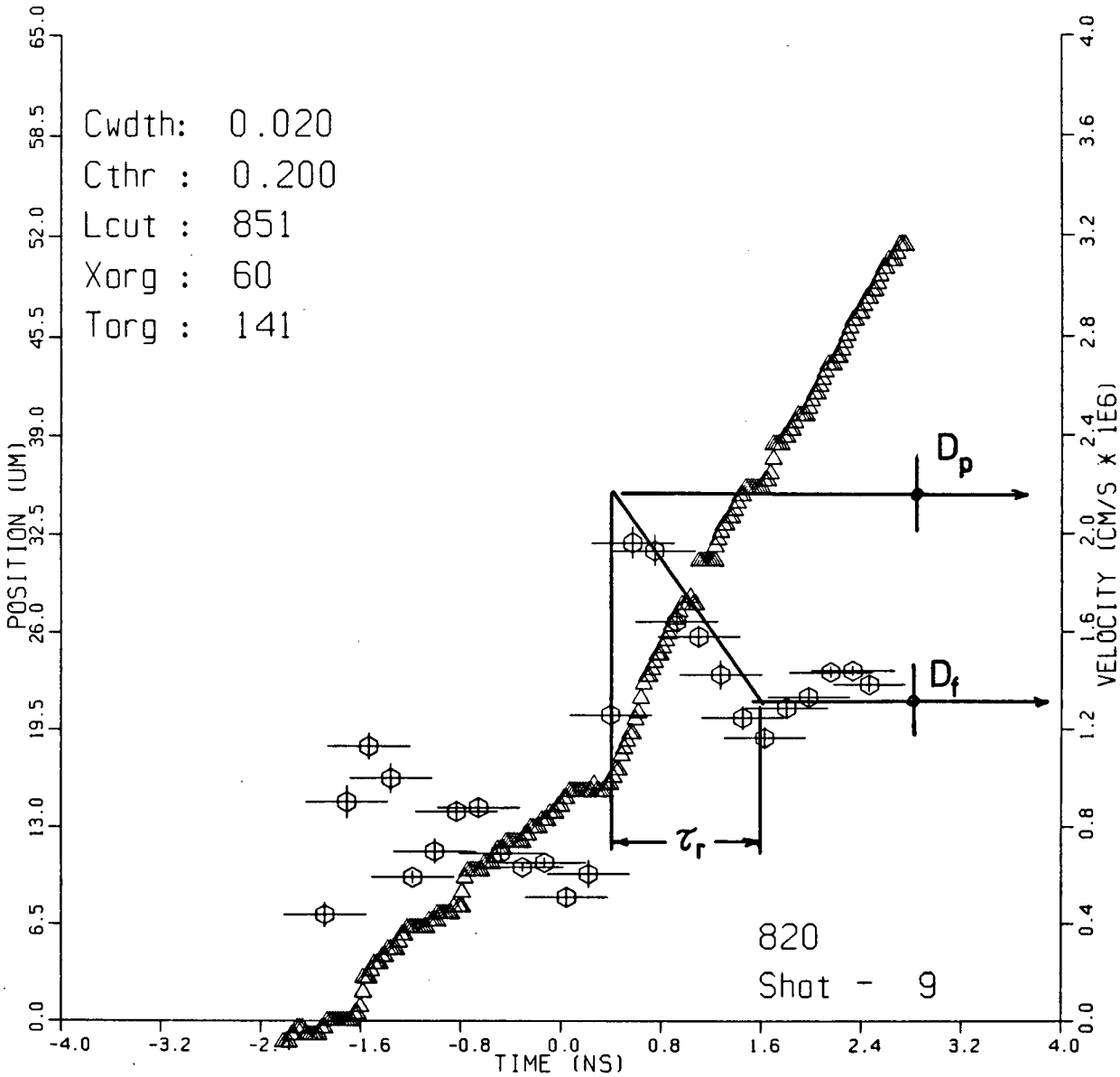

Figure 3-7 Reduced trajectory measurement as produced by edge detection analysis. Open triangles represent the shadow boundary and hexagons represent the instantaneous speed along the trajectory by piecewise linear fits. Also indicated is the method for extracting shock speeds D_f and D_p as well as a relaxation time τ_r.

to make much more sense of it than with the simple graphical method. These data for all of the shots analyzed in this thesis are tabulated in Table IV, chapter 5.

As noted above, pulse shapes were recorded with a photodiode and oscilloscope. The pulse for each shot was recorded on Polaroid film and subsequently digitized. This allowed a more accurate representation of the pulse for computer simulations. In particular it should be noted that the pulses deviated somewhat from a pure gaussian shape, especially at the lower power levels. Furthermore, the existence of a tail at the end of the pulse tended to reduce the peak power level from what would be expected by simply dividing the measured energy by the temporal full width at half maximum (FWHM). An example of a digitized pulse is shown in Figure 3-8.

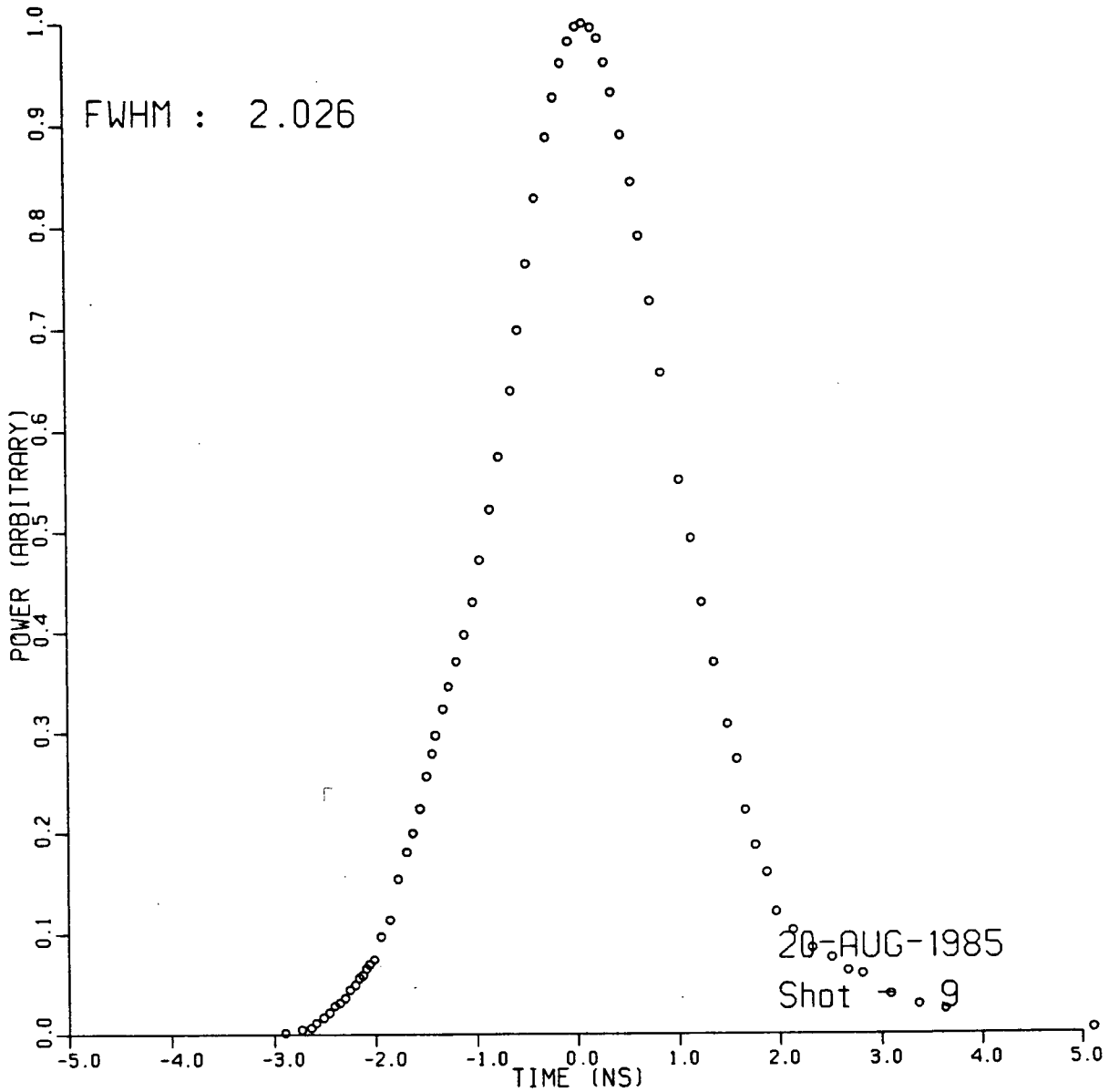

Figure 3-8 Example of a digitized laser pulse shape obtained from a photodiode measurement. Open symbols represent the digitized points.

CHAPTER 4

NUMERICAL CALCULATIONS

4.1 Introduction

In this chapter, a description of the hydrodynamic computer code used to simulate the experiment is given. This is followed by a survey of calculations performed with the code for irradiation conditions typical of our experiments. The calculations are compared with analytic scaling laws for ablation pressure and plasma temperature as a function of laser irradiance. Simulations were also made with various physical processes switched on or off to assess their effect on the shock formation process.

4.2 Hydrodynamic computer simulations

Analysis of any laser-target experiment must rely heavily on comparisons of experimental results with computer simulations. This is because there are many physical processes occuring simultaneously in the experiment which cannot be treated adequately with simpler analytic methods. Nevertheless, simulation models are still only approximate calculations, as they involve assumptions and uncertainties.

The simulations corresponding to this experiment were performed with a hydrocode LTC (Laser Target Code) developed at UBC (by the author). This hydrocode was adapted from the laser fusion code MEDUSA[101]. Substantial modifications have been made to the physical content and numerical technique so that

it is no longer appropriate to refer to the original MEDUSA description. On the other hand, much of the hydrocode is very similar to those in use in other laboratories, and the intent is to model the same basic process (laser ablation). Since the details of this code have not been described elsewhere, this section gives an outline of the physical content included in the code as well as an overview of the numerical treatment of the equations.

4.2.1 Physical content in LTC

The physics is embodied in a coupled set of differential equations which represent the conservation of mass, momentum and energy. The most important ingredients in the physical description are the EOS, the laser absorption process (inverse bremsstrahlung), and heat conduction. This basic level of description is referred to as the "standard" description in this thesis. The hydrocode is also configured to handle some additional detail namely the inclusion of radiation diffusion transport, as well as a two-temperature (electron and ion) EOS description which takes into account the non-equlibrium between electron and ion temperatures in the rarefied coronal plasma. Another effect which was explored with an *ad hoc* prescription was radiative preheat of the cold target by soft X-ray line radiation from the coronal plasma. These latter aspects turned out to be less important for modelling the experiment; however, they are all included in the following description for completeness.

LTC solves the one-dimensional plane parallel fluid equations in a Lagrangean fashion. In the most complete (three-temperature) description the target material is regarded as a compressible fluid composed of interpenetrating electron and ion components each described by a separate temperature. In addition a radiation field, characterized by a separate radiation temperature, interacts with the material

through frequency averaged Rosseland and Planck opacities (greybody approximation). In the simpler "standard" description the fluid is characterized by a single temperature, and no radiation transport is considered.

In the Lagrangean description the calculation follows the time evolution of individual fluid elements. The initial condition is always that of a slab of material of specified density and temperature profile with definite boundaries, $R_i(t)$ and $R_o(t)$ ($R_o > R_i$). The laser radiation illuminates the boundary R_0 and partially penetrates the material. A plot of the Lagrangean mesh as it evolves during the course of a typical calculation is shown in Figure 4-1. Each line represents a fluid element (meshpoint) and is fixed to the local fluid reference frame. Various hydrodynamic features of the laser plasma interaction, which are labelled in this figure, will be discussed throughout this chapter and the next.

The time, t, and Lagrangean coordinate, m, are regarded as the independent variables. The Lagrangean coordinate m is defined in terms of the density profile in laboratory coordinates, r and t, by,

$$m(r,t) = \int_{R_i(t)}^{r} \rho(r',t)dr' \qquad [4-1]$$

where $R_i(t)$ is the position of the left hand (inner) free surface of the target and $\rho(r,t)$ is the density profile.

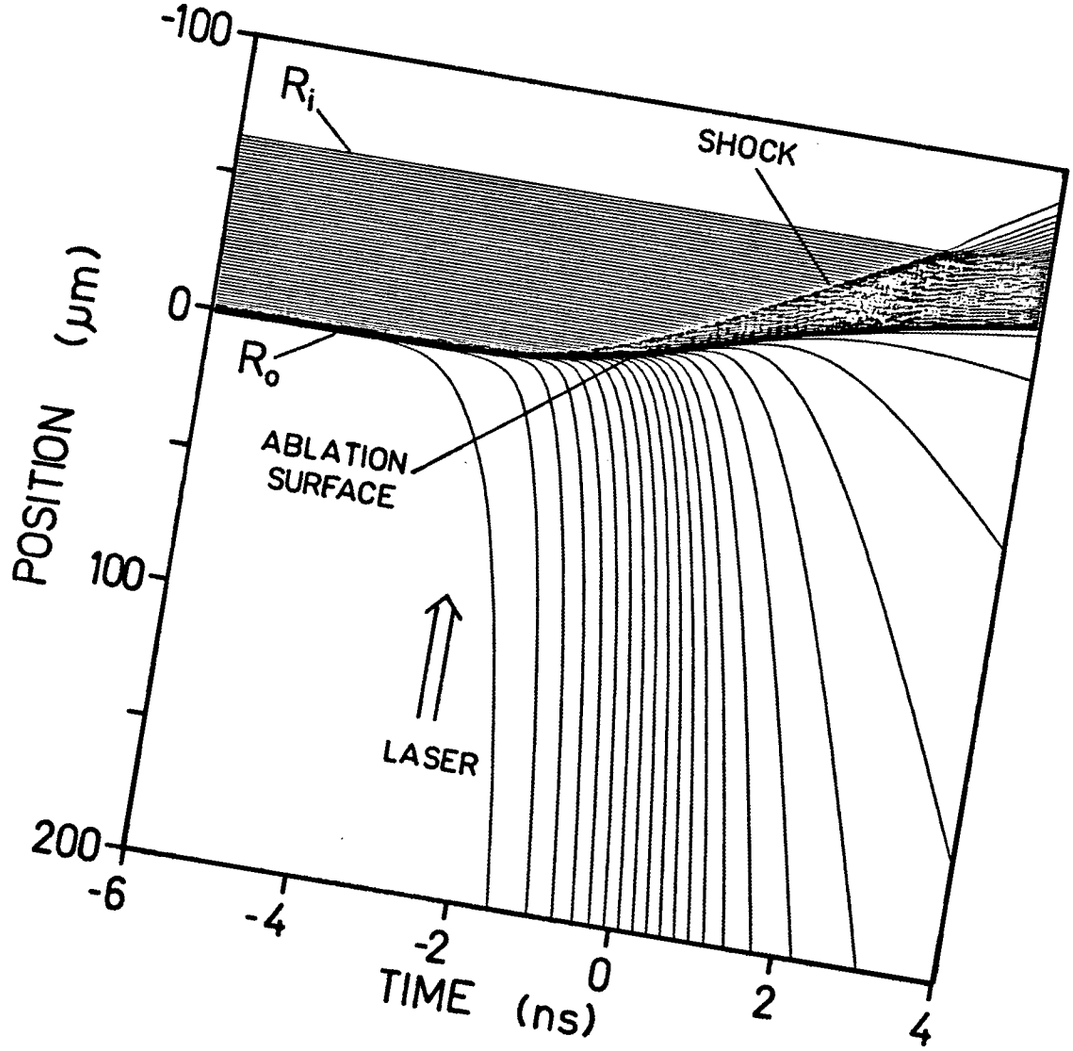

Figure 4-1 Lagrangean mesh as it evolves during the course of a calculation. Features of the laser-target interaction are labelled.

For the model used in LTC the complete set of equations describing the physical processes are:

$$\frac{\partial V}{\partial t} - \frac{\partial u}{\partial m} = 0 \qquad [4-2a]$$

$$\frac{\partial u}{\partial t} + \frac{\partial (P_e + P_i)}{\partial m} = 0 \qquad [4-2b]$$

$$\frac{\partial E_e}{\partial t} + P_e \frac{\partial V}{\partial t} = Q_e \qquad [4-2c]$$

$$\frac{\partial E_i}{\partial t} + P_i \frac{\partial V}{\partial t} = Q_i \qquad [4-2d]$$

$$\frac{\partial (U/\rho)}{\partial t} + fU \frac{\partial V}{\partial t} = -\frac{\partial F}{\partial m} + c\kappa_p (U_p - U) \qquad [4-2e]$$

$$c^{-2} \frac{\partial F}{\partial t} = \rho \frac{\partial (fU)}{\partial m} - \frac{\rho \chi}{c} F \qquad [4-2f]$$

The principal dependent variables that are solved for are specific volume, $V = 1/\rho$, fluid velocity, u, material internal energies, E_e and E_i, for the electrons and ions respectively, the radiation energy density U, and the radiation flux, F.

Equations [4-2a] and [4-2b] represent the fluid continuity and momentum equations, respectively. In the momentum equation [4-2b], the hydrodynamic pressure is composed of the electron pressure P_e, and the ion pressure, P_i. (Radiation contributions to pressure and internal energy are always neglible for the experimental conditions; radiation plays a role only in energy transport.) Conservation of energy for the electron and ion fluids is represented by the two equations [4-2c] and [4-2d]. Both of these equations express the first law of thermodynamics in which the right hand side, represented by Q, is the heat source term due to the various energy transport and deposition processes included in the model.

The radiation field is described by equations [4-2e] and [4-2f]. Detailed discussion and a derivation of this radiative transfer description can be found in Mihalas

and Mihalas[102]. Briefly these two equations are derived from the first and second equations in a moment expansion of the radiative transfer equation. Equation [4-2e] describes conservation of radiation energy and equation [4-2f] describes conservation of radiation momentum (pressure). The quantity f is known as the Eddington factor and relates the radiation energy to the radiation pressure (momentum) by the expression

$$P_r = fU$$

where P_r is the radiation pressure. The Eddington factor has a value restricted to the range $\frac{1}{3} \leq f \leq 1$ where $f = \frac{1}{3}$ is obtained in a uniform isotropic radiation field (the diffusion limit) and $f = 1$ is obtained in the free streaming limit. For the calculations here $f = \frac{1}{3}$ was used. If the term on the left hand side of equation [4-2f] is neglected then these equations can be combined to give the standard radiation diffusion approximation. The term is retained in order to limit the radiation flux at the free streaming value in optically thin regions of the plasma; this obviates the need for artificial flux-limits which is necessary in the diffusion approximation. The numerical complexity of this description is equivalent to that of the heat equation.

In the next few paragraphs the definitions of various terms of these equations will be discussed in detail. It should be noted that MKS units are used throughout the definitions of physical quantities (above and below):

time	$[t] = \mathrm{s}$;
Lagrangean coordinate	$[m] = \mathrm{kg/m^2}$;
specific volume	$[V] = [1/\rho] = \mathrm{m^3/kg}$;
pressure	$[P] = \mathrm{J/m^3} = \mathrm{Pa}$;
velocity	$[u] = [c] = \mathrm{m/s}$;
internal energy	$[E] = \mathrm{J/kg}$;
radiation energy	$[U] = \mathrm{J/m^3}$;
temperature	$[T] = \mathrm{K}$;

heat source	$[Q] = \mathrm{W/kg}$;
heat (radiation) flux	$[F] = \mathrm{W/m^2}$;
length	$[\lambda] = [r] = \mathrm{m}$;
number density	$[n] = \mathrm{m^{-3}}$; and,
opacity	$[\kappa_p] = [\chi] = \mathrm{m^2/kg}$.

A number of secondary quantities are required to complete the description, and these can be obtained once the principal dependent variables are defined. Most important is the equation of state, which is expressed in the form,

$$T_e = T_e(V, E_e), \qquad P_e = P_e(V, E_e) \qquad [4-3a]$$

$$T_i = T_i(V, E_i), \qquad P_i = P_i(V, E_i) \qquad [4-3b]$$

where T_e, T_i and P_e, P_i are the electron and ion temperatures and pressure components respectively. Other important quantities include the ion density,

$$n_i = \rho / A m_p,$$

where A is the average atomic mass number of the target material, and m_p is the proton mass; the electron density and ionization state,

$$n_e = Z n_i, \qquad Z = Z(\rho, T_e);$$

and, the Coulomb logarithm[102]

$$\ln\Lambda = 16.34 - \ln(T_e^{3/2} n_e^{-1/2} Z^{-1}). \qquad [4-4]$$

The ionization state is obtained from an appropriate model of atomic physics; the most valid such model is the collisional radiative (CR) model[103], however, a Saha[104] equation or coronal model[105] are often used as approximations. For the calculations

performed in this thesis Z was obtained from a SESAME data table[106] which was generated from a Saha-type calculation. The laser wavelength is λ, and this is needed to define the critical density,

$$n_{cr} = 1.1 \times 10^{15} \lambda^{-2} \qquad [4-5]$$

which is the electron density at which the laser frequency is resonant with the plasma frequency and the light is reflected. Other atomic and material dependent data such as conductivities and opacities can be specified in tabular form (from the SESAME data library) and thus the code can be applied equally well to a wide range of target materials.

The energy source terms, Q, in the fluid energy equations contain all the (non-hydrodynamic) energy transport processes. This includes heat conduction, laser energy deposition, and energy exchange between the various fluids (electron, ion and radiation). In particular,

$$Q_e = H_e + X_{ei} + A_{las} - c\kappa_p(U_p - U), \qquad [4-6a]$$

and

$$Q_i = H_i - X_{ei}. \qquad [4-6b]$$

These terms will be briefly described.

Electron and ion heat conduction are given by the terms H_e and H_i. These are defined by

$$H = \frac{1}{\rho} \nabla \cdot \kappa \nabla T \qquad [4-7]$$

where κ is the thermal conductivity. For the electrons the thermal conductivity can be specified in a tabular form (such as from the SESAME library). Alternatively

(or when a table is not available) the Spitzer form of conductivity is used[107],

$$\kappa_e = 1.955 \times 10^{-9} \epsilon\delta_t \frac{T_e^{5/2}}{Z ln\Lambda} \qquad [4-8]$$

where

$$\epsilon\delta_t = 0.095 \frac{(Z + 0.24)}{(1 + 0.24Z)}.$$

Ion heat conductivity is given by a similar expression[101],

$$\kappa_i = 4.3 \times 10^{-12} \frac{T_i^{5/2}}{Z ln\Lambda} \qquad [4-9]$$

Electron-ion energy exchange is governed by the term X_{ei}. This is given by[101]

$$X_{ei} = 0.59 \times 10^{-8} n_e (T_i - T_e) T_e^{3/2} M^{-1} Z^2 ln\Lambda \qquad [4-10]$$

where M and Z are the atomic mass number and charge state of the ions, respectively.

Absorption of the laser energy is assumed to occur via inverse bremsstrahlung up to the critical density. The absorption coefficient, α, is[101]

$$\alpha = \frac{13.51}{\lambda^2} \frac{\beta^2}{(1-\beta)^{1/2}} \frac{Z \ln\Lambda}{T_e^{3/2}} \qquad [4-11]$$

where $\beta = n_e/n_{cr} < 1$. The laser power reaching a point r approaching from the boundary R_o is given by

$$\Phi_{las}(r,t) = \Phi_{las}(R_o,t)\left(1 - \exp \int_r^{R_o} -\alpha(r',t)\, dr'\right), \qquad [4-12]$$

where $\Phi_{las}(R_o, t)$ is the laser flux incident on the target at time t. The absorbed power (per unit mass) for a cell of size Δr and mass Δm at point r is

$$A_{las}(r,t) = \Phi_{las}(r,t)\frac{exp(-\alpha\Delta r)}{\Delta m} \qquad [4-13]$$

For all the simulations the the laser energy reaching the critical density surface was arbitrarily deposited (absorbed) in that cell, so that absorption is always 100%.

The coupling to the radiation field (emission and absorption) is given by the last term in equation $[4-6a]$,

$$c\kappa_p(U_p - U)$$

Here κ_p is the Planck mean opacity and c is the speed of light. U_p is the energy density of a radiation field in equilibrium with the matter temperature, and U is the actual energy density of the radiation field. U_p is given by the expression:

$$U_p = 4\sigma T_e^4 \qquad [4-14]$$

where σ is the Stefan-Boltzmann constant. Using an equivalent definition the radiation field is characterized by a radiation temperature, T_r, which is related to U by,

$$T_r = \left(\frac{U}{4\sigma}\right)^{1/4} \qquad [4-15]$$

The radiation temperature, T_r, is not necessarily in equilibrium with the matter temperature. The radiation transport opacity, χ, in equation $[4-2f]$, is the Rosseland mean opacity, which gives the mean free path of the photons.

In the single temperature description the electron and ion components are assumed to have the same temperature. In this case the fluid is described by a

single internal energy, E, which yields the pressure P and temperature T from a single temperature EOS,

$$P = P(V,E), \qquad T = T(V,E).$$

and equations $[4-2c,d]$ are replaced with a single equation:

$$\frac{\partial E}{\partial t} + P\frac{\partial V}{\partial t} = Q_e + Q_i. \qquad [4-16]$$

The single temperature description is equivalent to setting the electron-ion coupling term X_{ei} to a very large value (note that it cancels out in the expression $Q_e + Q_i$). For calculations neglecting radiation transport, equations $[4-2e]$ and $[4-2f]$ are dropped and the radiative coupling term in equation $[4-6a]$ is set to zero.

4.2.2 Numerical methods in LTC

The mesh used in LTC is similar to that described for MEDUSA. It consists of a set of cells of mass Δm_j identified by subscript j. Associated with each cell is an average value of each principal dependent variable, identified by the subscript j, to indicate a cell-centred quantity. Quantities defined on the cell boundaries have half-integer subscripts, e.g. $j+\frac{1}{2}$. Thus the coordinates of the cell boundaries are labelled $r_{j+\frac{1}{2}}$. Time steps are denoted by a superscript n, and are separated in time by the discrete interval Δt. At the beginning of the nth computational time step ($t = t^n$) it is assumed that average values of the principal hydrodynamic quantities u, V, E_e, E_i and U are known for each cell, and F and r are known on each cell boundary. All other secondary quantities needed in the calculation (opacities, conductivities etc.) are expressed as functions of these variables and are therefore known. The calculation of a timestep advances these quantities from time t^n to time $t^{n+1} = t^n + \Delta t$.

Solution of the equations is accomplished in two phases for each timestep. In the first phase the hydrodynamic motion of the mesh is calculated by advancing the coordinates, r, and velocities, u, with an explicit hydrodynamic scheme. This defines the variables r (hence V and ρ), and u at the advanced time level. In the second phase the energy and radiation transport equations are then solved implicitly for E_e, E_i, U, and F, and iterated to convergence. Iteration is necessary to account for nonlinear dependences of equation of state functions, transport coefficients and othe secondary quantities on the thermodynamic variables.

4.2.2A Hydrodynamics

The first phase of the solution involves advancing the mesh coordinates r and velocities u one time level. This is accomplished by solving a simplified version of the system given in equations $[4-2]$. These are,

$$\frac{\partial V}{\partial t} - \frac{\partial u}{\partial m} = 0 \qquad [4-17a]$$

$$\frac{\partial u}{\partial t} + \frac{\partial p}{\partial m} = 0 \qquad [4-17b]$$

$$\frac{\partial e}{\partial t} + \frac{\partial (up)}{\partial m} = 0 \qquad [4-17c]$$

In this system $e = E_e + E_i + u^2/2$ is the total energy of the fluid and $p = P_e + P_i$ is the hydrodynamic pressure. These equations are written in conservation form (the conserved quantities being mass, momentum and energy). Note that all of the heat source terms, Q, have been dropped, and the fluid is treated as being effectively single temperature. Hence, only adiabatic hydrodynamic motion is described. This description is sufficient to conserve mass and momentum, but proper accounting of the energy equation requires the adiabatic solution to be corrected to include transport and source terms by treating the full energy equations implicitly, hence the need for the second phase of calculation.

The method of solution follows the piecewise parabolic method (PPM), a scheme developed by Colella and Woodward[108]. This is a higher order version of the original scheme due to Godunov[109]. The technique involves obtaining average values of the velocity and pressure on each side of the cell interfaces. These are used as initial conditions for solving a Riemann shock tube problem at each interface. The solution yields average values for the pressure $\bar{p}$ and particle velocity $\bar{u}$ at the interface which are then used to construct the hydrodynamic momentum and energy fluxes on all the interfaces. The coordinates and velocities can then be advanced in time using the solutions to the Riemann problem at each interface:

$$r_{j+\frac{1}{2}}^{n+1} = r_{j+\frac{1}{2}}^{n} + \Delta t \bar{u}_{j+\frac{1}{2}}; \qquad V_j^n = \frac{1}{\Delta m_j}[r_{j+\frac{1}{2}}^n - r_{j-\frac{1}{2}}^n]; \qquad [4-18a]$$

$$u_j^{n+1} = u_j^n + \frac{\Delta t}{\Delta m_j}[\bar{p}_{j+\frac{1}{2}} - \bar{p}_{j-\frac{1}{2}}]; \qquad [4-18b]$$

$$e_j^{n+1} = e_j^n + \frac{\Delta t}{\Delta m_j}[\bar{p}_{j+\frac{1}{2}}\bar{u}_{j+\frac{1}{2}} - \bar{p}_{j-\frac{1}{2}}\bar{u}_{j-\frac{1}{2}}]. \qquad [4-18c]$$

For two-temperature calculations the change in total energy $e_j^{n+1} - e_j^n$ has to be separated into electron and ion contributions. In LTC this is done by assuming that all hydrodynamic processes affect the electrons isentropically, hence,

$$\Delta E_{e_j}\Big|_{hydro} = -P_{e_j}[V_j^{n+1} - V_j^n]. \qquad [4-19]$$

The remainder is assigned to the ion fluid,

$$\Delta E_{i_j}\Big|_{hydro} = (e_j^{n+1} - e_j^n - \frac{1}{2}[(u_j^{n+1})^2 - (u_j^n)^2]) - \Delta E_{e_j}\Big|_{hydro} \qquad [4-20]$$

In these definitions the subscript *hydro* denotes adiabatic hydrodynamic processes including shocks. In smooth flow $d(e-u^2/2)/dt$ is identically equal to the adiabatic work term $-pdV/dt$. It also contains contributions due to shock heating in regions

of steep gradients. Note that shock heating processes are therefore assigned to the ion component. This prescription is no different from that used in MEDUSA, in which shock heating due to artificial viscosity is assigned to the ion component[101]. For the single temperature description there is no separation of electron and ion contributions so that the change in internal energy is given simply by,

$$\Delta E_j\Big|_{hydro} = e_j^{n+1} - e_j^n - \frac{1}{2}[(u_j^{n+1})^2 - (u_j^n)^2] \qquad [4-21]$$

In this scheme the main difficulty lies in solving the Riemann problem efficiently and reliably. The Riemann shock problem is summarized in Figure 4-2. At time $t = 0$ one assumes that the region around the interface between adjacent cells can be approximated by constant distributions of pressure, density and velocity on each side of the interface. These are usually denoted (p_l, ρ_l, u_l) and (p_r, ρ_r, u_r) where the subscripts denote the regions to the left and to the right of the interface. For the general case this initial condition represents an arbitrary discontinuity and the profiles must decay into two waves propagating away from the interface in opposite directions. The boundary condition at the interface for $t > 0$ is that the pressure and particle velocity must be equal on each side of it (continuous functions across the interface). The solution is self-similar (a function of x/t, where $x = 0$ at the interface) and the propagating waves may be shocks or centred rarefactions. The three cases shown in Figure 4-2 correspond to decay of the discontinuity into: (a) two shocks; (b) a shock and a rarefaction; and, (c) two rarefactions.

For the numerical problem the quantities of interest are simply $\bar{p}$ and $\bar{u}$ at the interface. A graphical solution can be found in the $p - u$ plane. This is shown in Figure 4-3 which demonstrates the solution $\bar{p}$ and $\bar{u}$ for initial conditions corresponding to the three cases above. The curves shown in the figure are Hugoniots centred on the initial states. (For rarefaction waves a Riemann integral gives the

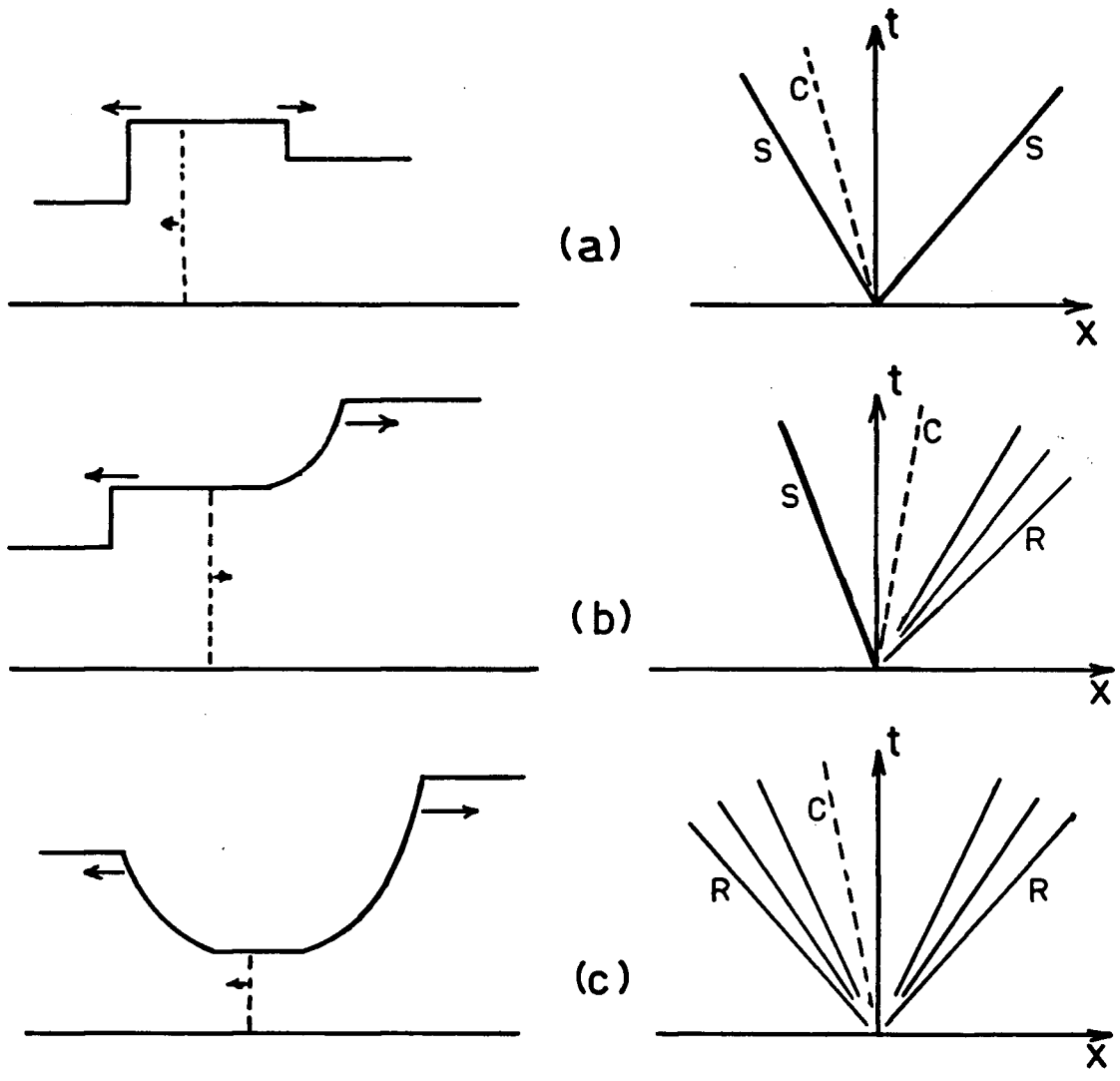

Figure 4-2 Schematic picture of Riemann shock tube problem. The diagrams on the left represent pressure profiles of the waves produced from the decay of the discontinuity at the interface. On the right are $x - t$ diagrams showing the self-similar propagation of the waves. 'R' denotes rarefaction fan, 'S' denotes shock, and 'C' denotes contact surface, which shows the motion of the interface. The three cases are: (a) decay into two shocks; (b) decay into a shock and a rarefaction; and (c) decay into two rarefactions.

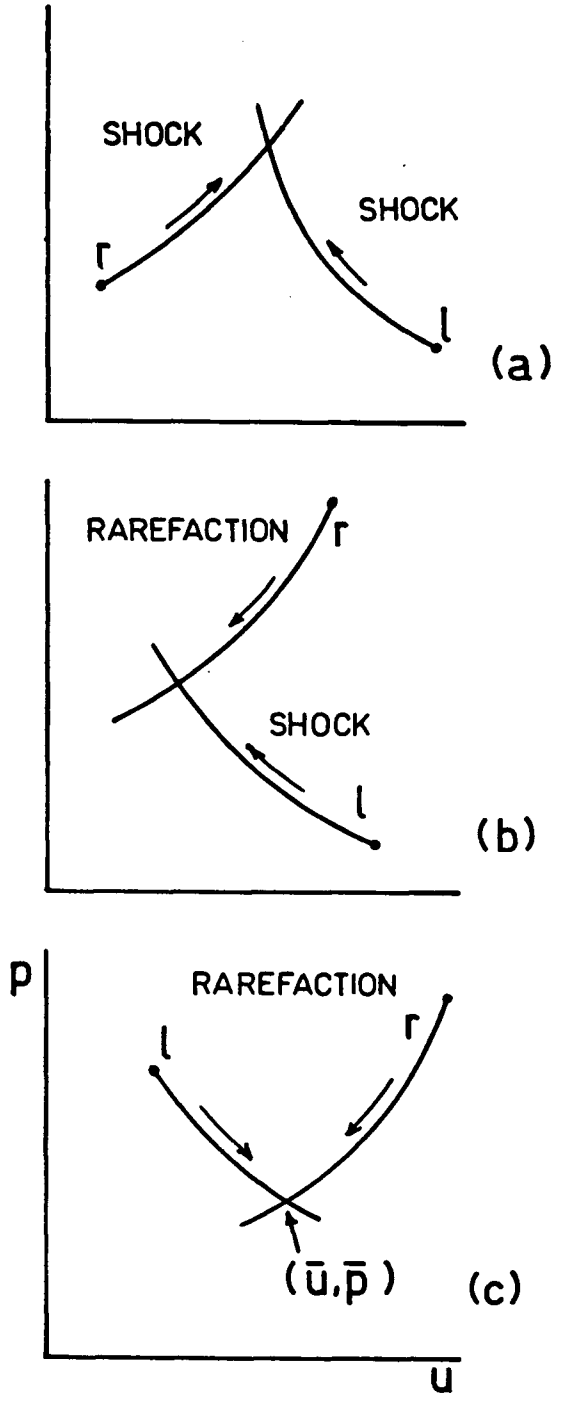

Figure 4-3 Solution of the Riemann shock tube problem in the p-u plane. Initial states on the left 'l' and the right 'r' of the interface are indicated. The Hugoniot curves are the solid lines and the value of $(\bar{u}, \bar{p})$ at the interface is given by the intersection of the curves. The three cases (a), (b) and (c) correspond to those shown in Figure 4-2.

exact solution; however, a rarefaction shock approximation is commonly used in numerical schemes[108,110].)

In general the numerical solution has to be performed iteratively to obtain the intersection point $(\overline{u}, \overline{p})$. For analytic equations of state (e.g. polytropic gas laws) a linear interpolation technique, or Newton's method can be iterated to convergence, usually with only a few iterations. Futher complexities arise for tabular or non-analytic equation of state representations because the Hugoniot curves are not represented analytically. This requires another level of iterations to obtain points on the Hugoniot (solution of the Rankine-Hugoniot relations). For LTC it was desired to have an algorithm that worked for an arbitrary EOS, specified by a table or otherwise, and in which a two-temperature description is optional.

LTC uses an approximation due to Colella and Glaz[110] which allows extension of the original PPM method to an arbitrary EOS or to the two-temperature description in a simple manner. The goal is to obtain an accurate *analytic* representation of the Hugoniot curve in the $p-u$ plane so that the Riemann problem can be solved quickly without the inner iteration loop and EOS evaluations needed to obtain the Hugoniot points. In this method the fluid EOS is approximated locally with two parameters,

$$\Gamma = \frac{\rho c_s^2}{p}, \qquad [4-22]$$

$$\gamma = 1 + \frac{pV}{E}. \qquad [4-23]$$

where c_s is the sound speed. This is given by, $c_s^2 = \partial p/\partial \rho \,|_S$ where S is the entropy. For polytropic gases, γ is the ratio of specific heats and $\gamma = \Gamma$; neither statement is true in general. Using this parameterization Colella and Glaz have derived a Hugoniot formula which is correct to second order in the weak wave limit,

$$\left|\frac{\Delta p}{\Delta u}\right|^2 = \frac{(p_* - p_s)(p_* + \frac{1}{2}(\gamma_{*s} - 1)(p_* + p_s))}{p_* V_s - p_s V_s(\gamma_{*s} - 1)/(\gamma_s - 1)} \qquad [4-24]$$

where

$$\gamma_{*s} = \max(\gamma_{min}, \min(\hat{\gamma}_{*s}, \gamma_{max})),$$

$$\hat{\gamma}_{*s} = \gamma_s + (1 - \frac{\overline{\gamma}}{\overline{\Gamma}})(\overline{\gamma} - 1)\frac{p_* - p_s}{\frac{1}{2}(p_* + p_s)},$$

and

$$\overline{\gamma} = \frac{1}{2}(\gamma_l + \gamma_r), \quad \overline{\Gamma} = \frac{1}{2}(\Gamma_l + \Gamma_r).$$

Here the subscript s denotes the l or r states and the subscript $*$ denotes a point on the Hugoniot. The sign of the term $\Delta p/\Delta u$ is assigned according to the direction of the wave. This is positive for waves travelling to the right ($s = r$) and negative for waves travelling to the left ($s = l$). The Riemann solution is then obtained by simultaneous solution of this Hugoniot formula for a common p_* behind the two waves propagating from each side of the interface. γ_* is an estimate of the value of γ at the Hugoniot point p_*. The terms γ_{max} and γ_{min} are included to keep the estimated value of γ_* from exceeding physically reasonable limits. These limiting values are determined from the local flow conditions (up to a few cells away from the interface being solved). Further details of the derivation and implementation of this approximation can be found in reference 110.

The Colella and Glaz approximation was implemented in LTC using the following formulas to define the variables in the definitions of γ and Γ in equations $[4-17]$ and $[4-18]$. The hydrodynamic pressure p and internal energy E are given by,

$$p = P_e + P_i, \qquad E = E_e + E_i. \qquad [4-25]$$

(Contributions to p and E due to the radiation field are neglected, and are indeed negligible for the temperatures reached in the experiment and calculations.) The

isentropic sound speed is given by,

$$c_s^2 = \left.\frac{\partial p}{\partial \rho}\right|_S = \left(\frac{\partial P_e}{\partial \rho} + \frac{P_e}{\rho^2}\frac{\partial P_e}{\partial E_e}\right) + \left(\frac{\partial P_i}{\partial \rho} + \frac{P_i}{\rho^2}\frac{\partial P_i}{\partial E_i}\right) \qquad [4-26]$$

which follows from the second law of thermodynamics for adiabatic processes. The partial derivatives in [4 – 26] are obtained from the EOS. For single temperature calculations the equivalent definitions are obvious.

The main advantage of the PPM formulation is that it has allowed a straightforward implementation of Lagrangean hydrodynamics to second-order accuracy. It uses a five-point interpolation scheme to construct profiles of the hydrodynamic variables; the left and right states used in the Riemann problem are obtained from these interpolated profiles rather than the piecewise constant profiles which are used in the standard Godunov method. The original Godunov method is accurate to first order only, and is highly dissipative. A common test of the accuracy of a numerical scheme is to compare it with an exact calculation of a standard problem. A Riemann problem was solved for an aluminum slab divided equally into two 50 μm regions with the following initial conditions: for the left region, $\rho_l = 4000$ kg/m^3,$T_l = 20000$ K and $u_l = 0$; for the right region, $\rho_r = 2698$ kg/m^3, $T_r = 300$ K and $u_r = 0$. The equation of state was taken from the SESAME library, table 3712. The material states specified in these initial conditions are similar to those found in laser-compressed foils. 60 cells were assigned to the left region and 40 cells to the right region, which gives a uniform mass per cell. Calculations were performed using the PPM method and the standard Godunov method. The Hugoniot approximation due to Colella and Glaz[110] was used in both calculations. Figure 4-4 shows the hydrodynamic profiles (ρ, p, u, and T) as they appear at $t = 3$ ns after the discontinuity was released. The higher order accuracy of the PPM scheme is immediately apparent in comparison with the first order Godunov method. The PPM method resolves details of the rarefaction wave, and produces a much sharper

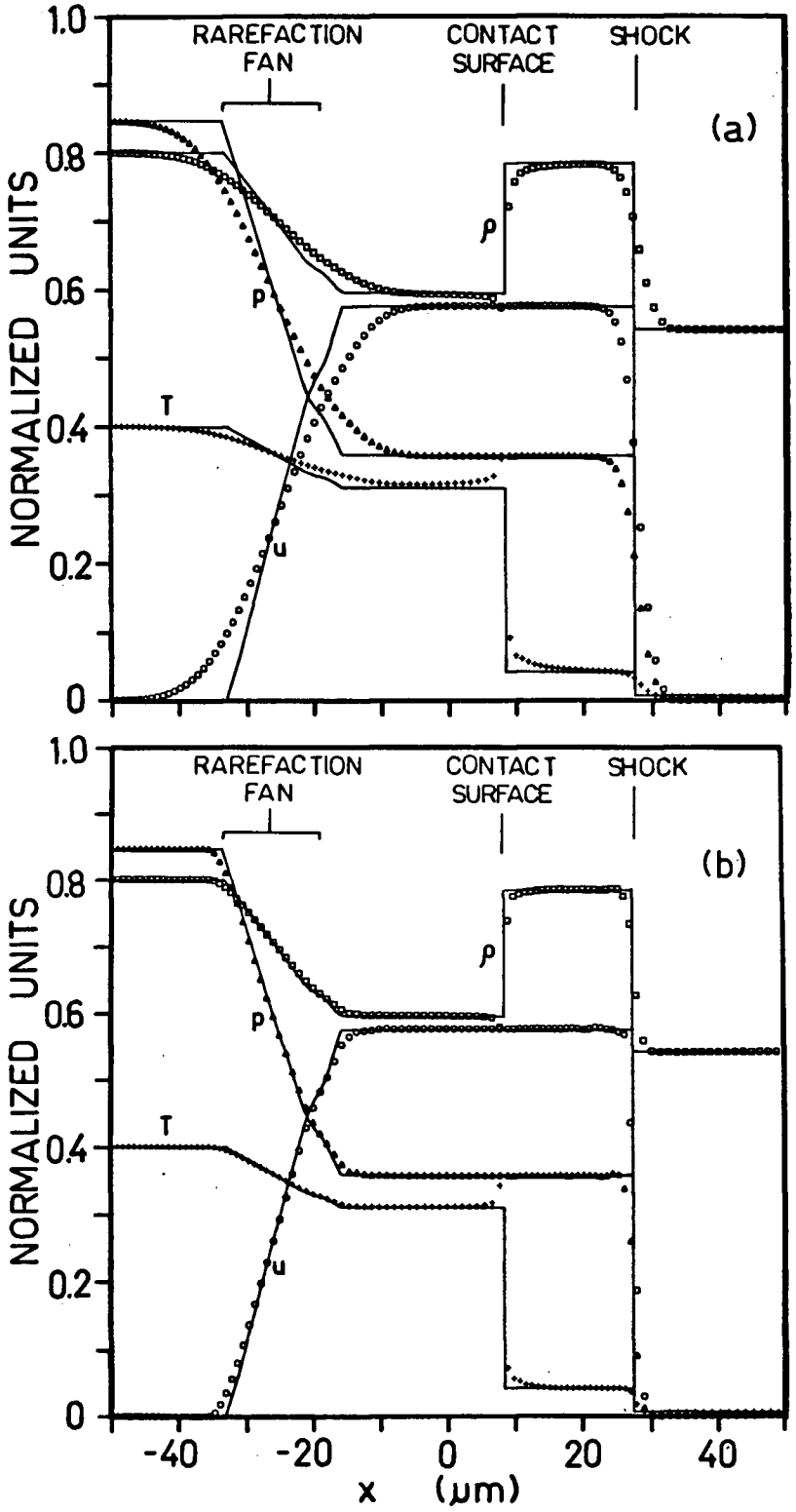

Figure 4-4 Numerical solution of a Riemann shock tube problem. Shown are two calculations: (a) Godunov method; and, (b) PPM method. Solid curves are exact solutions, symbols are from the calculations of the hydrocode.

shock front than does the standard Godunov method. This is important for laser-target calculations where it is important to resolve a broad range of features such as the high density shocked target and the low density coronal plasma with a limited number of cells. The most severe test of the algorithm occurs at the initial discontinuity before the two waves have propagated more than a few cells; here there is a noticeable error in the temperature and density profiles at the contact discontinuity. This is due to the approximate Hugoniot used in the Riemann solver. This type of error is most noticeable at very large arbitrary discontinuities, which do not appear in typical laser-target calculations except in special situations.

4.2.2B Energy Transport

In the second stage of the calculation the goal is to solve the energy equations self-consistently by including all of the temperature and density dependent source terms (Q). Both the electrons and ions are treated identically in the numerical method and will not be distinguished in the following description.

Solution of the electron and ion energy equations is only slightly changed from the original method in MEDUSA. The energy equations are written in the form,

$$C_V \frac{dT}{dt} + B_T \frac{d\rho}{dt} + p\frac{dV}{dt} = Q \qquad [4-27]$$

Here, the coefficients C_V and B_T are defined by the EOS,

$$C_V = \frac{\partial E}{\partial T}\Big|_V, \qquad B_T = \frac{\partial E}{\partial \rho}\Big|_T$$

The first two terms on the left hand side of $[4-27]$ represent the total time derivative of internal energy. The heat equation arises from the term H (contained within Q) on the right hand side, which involves the second spatial derivative of T. Rearranging this,

$$C_V \frac{dT}{dt} - \frac{1}{\rho}\frac{d}{dr}\kappa\frac{dT}{dr} = Q', \qquad [4-28]$$

where

$$Q' = Q - H - B_T \frac{d\rho}{dt} + \frac{dE}{dt}\Big|_{hydro}.$$

The term pdV/dt has been replaced by $-dE/dt|_{hydro}$ which represents adiabatic work; this term is obtained from the hydrodynamic phase of the calculation as outlined above (equations $[4-19]$ and $[4-20]$), and automatically includes (adiabatic) shock heating contributions.

To solve the heat equation the Crank-Nicholson time-centred differencing scheme is used, as in MEDUSA[101], which yields a tridiagonal system in the unknown T which is solved using Gauss elimination. Both the electron and ion components are treated identically in the numerical method, the only differences being the terms comprising the source function Q'.

Solution of this equation must be accomplished iteratively because several terms within Q' depend on T^{n+1} which is the unknown being solved for in the calculation. At the beginning of each iteration all of the temperature dependent quantities are evaluated with the current estimate of T^{n+1} (the first iteration uses T^n). After each iteration the new temperature solutions are used to evaluate the heat conduction term H and solve for E^{n+1} with the prescription,

$$E^{n+1} = E^n + \Delta E\Big|_{hydro} + Q\Delta t. \qquad [4-29]$$

Convergence of the solution is tested on E, not on T.

The radiation diffusion equations are treated using the method described in detail by Mihalas and Mihalas[102]. A backwards differencing scheme is applied to equation $[4-2f]$ to obtain an expression for F^{n+1} in terms of U^{n+1} and F^n,

$$F^{n+1} = -\rho c \lambda_r \frac{\partial(fU)}{\partial m} + \frac{\lambda_r}{\lambda_t} F^n \qquad [4-30]$$

where λ_r is an effective mean free path given by,

$$\lambda_r^{-1} = \lambda_t^{-1} + \rho\chi, \qquad \lambda_t = c\Delta t$$

Equation $[4-30]$ is substituted into equation $[4-2e]$ to eliminate F^{n+1} and obtain an expression similar in complexity to the heat equation for the unknown U^{n+1}. Differencing of the resulting expression gives a tridiagonal system which is solved by Gauss elimination. Once U^{n+1} is obtained then F^{n+1} is defined automatically by the relation in $[4-30]$. A boundary condition of $F(R_o,t) = cU(R_o,t)$ is imposed on the solution. This is equivalent to a free streaming radiation flux leaving the plasma towards the vacuum. This is the expected situation for the coronal plasma which is optically thin. An iterative solution is necessary to obtain a self-consistent solution, for similar reasons as for the electron and ion energy equations. Convergence of the iterations is tested on U.

The three energy equations corresponding to electrons, ions and radiation are solved within the same iteration loop. This guarantees a self-consistent treatment of energy conservation and exchange among the electron fluid, the ion fluid and the radiation field. Usually 1 to 3 iterations are sufficient for convergence to accuracies of the order of 1%.

4.2.3 Comments on the numerical model

The level of description used in LTC is fairly simple and similar to that of many routine hydrodynamic simulations performed at other laboratories. Since the objective of this study was to examine shock formation and propagation deep in a target, an emphasis was placed on accurate modelling of hydrodynamic compression. Although the transport processes in the corona can become quite complicated, the specific details have surprisingly little effect on the pressure pulse which drives the compression. Much recent work in the field of laser-target interactions has concentrated on improving the understanding of these transport processes using much

more sophisticated, closer to exact, theoretical treatments. This section contains a few comments regarding some of these aspects.

The radiation field from laser-produced plasmas on planar or spherical targets is strongly non-Planckian[111], and is usually not in equilibrium with the plasma (non-LTE or non-local thermodynamic equilibrium). Conversion of the laser energy into soft X-ray radiation varies strongly with the laser intensity and target material, Z. Conversion efficiencies in excess of 50% have been measured and calculated for high Z targets (such as Au)[112–115] Radiative effects appear to be of marginal importance for $Z < 10$, which is the case for SiO_2. Accurate theoretical models of the radiative properties of the plasma require a non-LTE description of the atomic physics[116]. The main physical features revealed by experiments and models are the dominating contributions of line radiation (bound-bound transitions) and recombination radiation (free-bound transitions) in the radiative spectrum[116,117]. For our experiments the most important aspect of the non-thermal radiation field are several intense spectral features which occur at photon energies with significant mean free paths in the cold target material. Correct modelling of the radiation spectrum with a non-LTE multigroup radiative transport model (or equivalent) was not possible. However, this question was considered using a plausible *ad hoc* model for estimating the spectrum and its effects on target preheat. Further discussion is presented in more detail in §4.4.2. Aside from the effects of preheat, the other main radiative effects are thermal losses, and some modification of the hydrodynamic profiles.

Electron thermal transport in laser-produced plasmas has undergone intensive study in recent years, particularly towards understanding the mechanisms governing electron thermal flux inhibition[118]. Hydrodynamic codes usually account for this by limiting the heat flux to some fraction of the free streaming limit[107]. For our experimental conditions the intensity level and scale lengths were well within the classical heat transport regime so that heat flux inihibition is not an issue, thus a flux limit was not used.

Finally, the validity of the calculation regarding the shock compression process is only as good as that of the equilibrium EOS description. It was noted in chapter 2 that non-equilibrium relaxation effects related to the Hugoniot elastic yield process and the stishovite phase transformation appear to be important; they are not incorporated into the physical description. Such effects are usually not addressed in laser plasma experiments, largely because most experiments operate in a regime of much higher temperature (1 eV and larger in the condensed material), much thinner targets (foils), and often much higher pressures (TPa). Solid state phase transformations and the elastic deformation region occupy a very small portion of the wide parameter space available to laser plasma experimenters.

4.3 Survey of Experimental Conditions

A number of test problems relevant to the experimental conditions have been calculated with LTC. These have been performed with different physical effects turned on or off to assess their relevance to the model. The results given in the following sections are intended to present the reader with a reasonable feel for the important physical processes and parameters in the context of the problem of interest: the shock formation process in thick targets. A detailed discussion of a "standard" calculation is presented first, followed by exploration of the effects of various modifications to the physics on the calculated results. In particular, runs were made with the radiation transport processes switched on and off, comparisons of the two-temperature versus one-temperature descriptions, and effects of different EOS (tables). The calculations were performed for fused silica targets initially at standard conditions ($\rho_0 = 2.2$ g/cm^3, $T_0 = 100$ K). The laser wavelength was chosen to be 0.532 μm and the laser pulse was gaussian with a 2.2 ns FWHM pulse length. Irradiances of $2 \times 10^{12}, 1 \times 10^{13}$, and 5×10^{13} W/cm^2 were used to span the intensity range covered in the experiments.

4.3.1 Standard calculation

All of the simulations of the experiment share a number of common features which are characteristic of the laser parameters (intensity, pulse length, pulse shape, and wavelength) and the target. This section gives a detailed description of the compression process for our experiment as predicted by the hydrocode.

Much understanding can be gained by examining the results of a "standard" calculation using the single temperature fluid model, inverse bremsstrahlung absorption and electron thermal conduction. From a large number of calculations it was found that the one-temperature and two-temperature versions of the model produce virtually identical results, and that the simple radiation diffusion model constitutes a small perturbation to the compression process (a reduction of the ablation pressure). Radiative preheat cannot be treated properly in the context of the radiation diffusion approximation, and has to be considered separately. Most of the basic physics can therefore be understood within the context of the standard description. For the purposes of the following discussion the "standard" calculation is performed for a gaussian laser pulse of 2.2 ns FWHM and peak intensity of 1.0×10^{13} W/cm^2 at 0.53 μm wavelength. The SESAME EOS table 7380 in the single temperature description was always used, unless otherwise stated.

For all the calculations a mesh of 150 cells was used. The mesh was finely zoned near the surface where the laser light is absorbed, and more coarsely zoned deeper in the target where the compression takes place. This was done by dividing the mesh into three regions as shown in Figure 4-5. Region 3 at large depths was zoned into 95 cells of uniform mass, region 1 at the target surface into 25 cells of uniform mass; and, region 2 consisted of 30 cells connecting these two in which the ratio of adjacent cell masses was set to a value of 0.90 to provide the transition from the fine to coarse zoning. This prescription assigns roughly 90% of the target mass to region 3 and 10% to regions 1 and 2. The total mass (or size) assigned to the initial mesh was varied according to the problem: a larger mass was used for higher

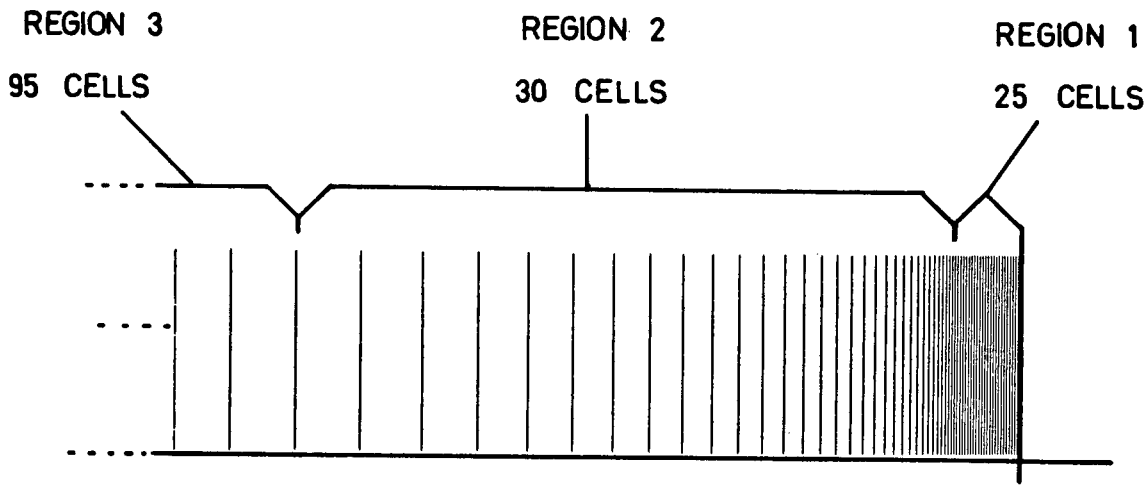

Figure 4-5 Mesh zoning scheme used in LTC calculations. The laser is incident from the right.

intensities for which the shock is faster and penetrates deeply, and smaller mass for lower intensities. The total size never exceeded 65 μm as the measurements did not extend to depths much more than this. Furthermore this maximum size is comparable to the spot size, beyond which the one-dimensional model is not a valid description of the experiment. This ensures that the maximum resolution afforded by the given mesh is used for each calculation.

4.3.2 Laser-driven ablation

Figure 4-6 shows a snapshot of the calculated profiles of various hydrodynamic and thermodynamic variables at the time of peak laser intensity ($t = 0$). These profiles are typical of the laser ablation process. Three regions can be distinguished in the figure. The laser is incident from the right and is absorbed in the low density hot plasma by inverse bremsstrahlung absorption. Nearly all of the laser energy is absorbed before the beam reaches the critical density surface. This absorption process is expected to be dominant for the relatively low intensities and the sub-micron laser wavelength used in the experiment. Even though there is an arbitrary deposition of 100% of the laser energy reaching the critical density surface, the calculation shows no indication of significant energy deposition at the critical surface. (The critical surface is easily identified by the point where A_{las} vanishes.) In the region beyond the critical density surface the density and temperature profiles vary rapidly before they join onto the cold high density solid. The dominant transport process in this region is electron thermal conduction. This region is commonly called the conduction or ablation region. The heat transported from the laser heated coronal plasma causes material at the solid surface to be ablated which then expands and accelerates into the vacuum. There is a rough energy balance between the electron thermal flux from the coronal plasma and the enthalpy flux of the heated material ablated from the surface of the target. The energy balance

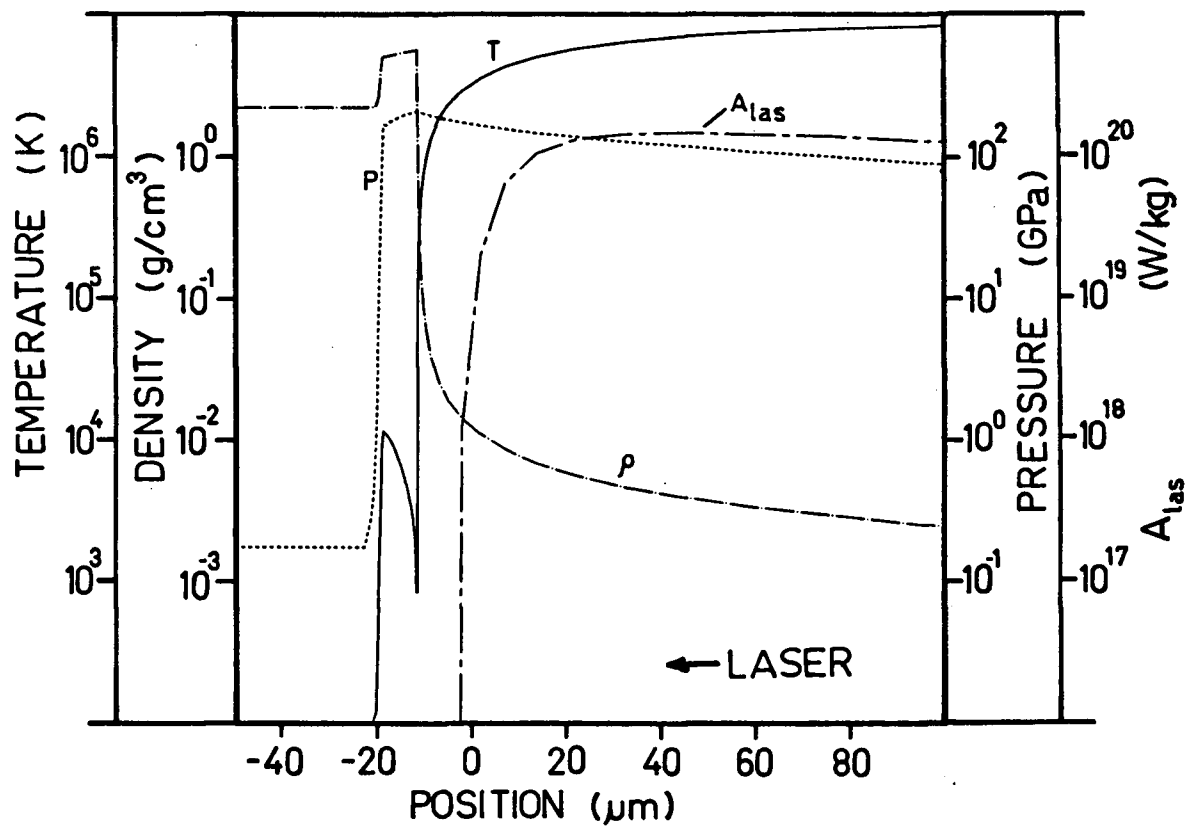

Figure 4-6 Snapshot of hydrodynamic profiles at the peak of the laser pulse for the "standard" calculation. Shown in the figure are the profiles of density, ρ, pressure, P, temperature, T, and laser energy deposition A_{las}.

is not exact because there is also a large momentum flux associated with the ablation process. This is coupled into the dense regions of the target through the high pressure shock which propagates ahead of the ablation front, carrying away some of the energy.

For a very wide range of laser intensities this type of ablation structure is always produced. The propagation of the ablation front is slow (subsonic) and thus the pressure signal outruns the heat wave to form the shock. The heat front is very steep and well defined near the cold solid because the mean free path of the coronal plasma electrons becomes very small in the cold solid. Thus the ablation surface can be regarded as a boundary between two distinct regions of the target. In the hot coronal plasma and the ablation region the material is at very low density and high temperature (compared to solid). Here, many different energy transport processes are operating including electron transport, radiative emission and absorption, radiation diffusion and laser absorption. The material is highly ionized and an ideal gas type of equation of state applies. The electron density and temperature of the coronal plasma are strongly dependent on the laser parameters and but only weakly material dependent. In contrast the shocked solid is at very low temperatures (≤ 1 eV) and high densities (larger than solid density). With the exception of preheat, no transport processes, other than shock propagation, are significant during the experimental time scale so that adiabatic hydrodynamics is sufficient to describe the motion of the dense regions of the target. The equation of state, characteristic of the target material under compression, is very important in understanding the material response at large depths in the target.

The ablation process establishes itself on a time scale small compared with the laser pulse time. This time scale is the time it takes for the ablative flow to adjust itself to changes in the laser intensity. A good estimate for this is the time for a fluid element to flow from the solid target across the ablation zone and into the laser heated coronal plasma. For our laser parameters this time scale is roughly

100 ps, compared to a pulse length $\geq$ 2 ns. The ablation pressure, which drives the shock, therefore tends to follow the laser pulse. This is important for understanding the nature of the compression process in the target, as will be described next.

4.3.3 Scaling laws

The ablation process is modelled numerically by LTC. However, several authors[119,120] have proposed analytic models which predict power law dependences of the basic hydrodynamic quantities such as plasma temperature, mass ablation rate and ablation pressure on the basic input parameters such as laser intensity and laser wavelength. The importance of the analytic models lies mainly in the physical insight they provide towards understanding the ablation process, and in providing simple analytic guides for predicting experimental conditions.

Briefly, the scaling law relationships are derived from energy balance considerations. The laser deposits energy at a characteristic electron density, n_a (and corresponding mass density ρ_a). Usually $n_a \simeq n_{cr}$, depending on the absorption process. The coronal plasma, to a good approximation, expands as an isothermal rarefaction wave with the wave head located at the absorption surface. In order to maintain isothermal conditions within the rarefaction wave a heat flux, $Q_r = \rho_a c_T^3$, must flow out towards the vacuum in the expanding plasma[119,120]. Here c_T is the isothermal sound speed given by $c_T = (ZkT_e/Am_p)^{1/2}$, which depends only on temperature (k is Boltzmann's constant). Beyond the critical surface the heat flux flows in the other direction towards the cold solid to drive the ablation process. The energy transported by this heat flux is carried off by the heated fluid flowing from the solid surface into the vacuum, $Q_a = \rho_a u^3/2 + 5\rho_a u c_T^2/2$. Here u is the plasma flow speed at the absorption surface.

The energy and mass flow for this process must be matched at the absorption surface to provide a steady state ablative process. Firstly, since the isothermal rarefaction head propagates into the ablative flow at the sound speed, the steady

state condition requires that the ablated material reaches sonic flow velocity, i.e. $u = c_T$, at the absorption surface. This leads to $Q_a = 3\rho_a c_T^3$. Secondly, the heat flux driving the ablation and the isothermal rarefaction must be supplied by the laser source so that $\Phi = Q_a + Q_r = 4\rho_a c_T^3$. This provides a simple relation between the laser flux and the plasma conditions if an equation of state is provided. For a plasma of atomic number A and charge state Z, $n_a = \rho_a Z/Am_p$. The material dependence arises from the parameters A and Z which always appear in the combination $\mu = A/Z$ in the analytical models. The absorption density is roughly proportional to the critical density n_{cr}, as noted above, which is in turn fixed by the laser wavelength, equation $[4-5]$. Thus, using these relations one finds a simple relationship between the laser flux Φ and the density and temperature of the plasma. This leads to predictions also of the pressure and mass ablation rate.

Without pursuing futher details of this analysis, the basic results from models due to Manheimer *et al.*[119] and Mora[120] are summarized in Table II. The different derivations apply slightly different approximations regarding the flow geometry and absorption mechanisms; however, they both use similar analytic treatments as described above. The model of Manheimer *et al.* assumes planar expansion and that the laser energy is all deposited at the critical density layer. The two models due to Mora assume strong inverse bremsstrahlung absorption so that the laser energy is deposited over a broad range of densities less than the critical density; the density of maximum absorption depends on a characteristic scale length, L. In the first model, here referred to as Mora–A, the plasma expansion is assumed planar and the scale length is given by $L \sim c_T \tau_\ell$ where c_T is the sound speed, and τ_ℓ the laser pulse length; in the second model, Mora–B, the expansion is assumed to be spherical with a scale length L which is determined by a characteristic dimension such as the laser spot size or the diameter of a microballoon target. The parameters $Z\tilde{\Lambda} \propto Z\ln\Lambda$ in

Table II. Laser ablation scaling laws

Model	P_{abl}	$\dot{m}$	T
Manheimer	$\Phi^{\frac{2}{3}}\lambda^{-\frac{2}{3}}\mu^{\frac{1}{3}}$	$\Phi^{\frac{1}{3}}\lambda^{-\frac{4}{3}}\mu^{\frac{2}{3}}$	$\Phi^{\frac{2}{3}}\lambda^{\frac{4}{3}}\mu^{\frac{1}{3}}$
Mora – A	$\Phi^{\frac{3}{4}}\lambda^{-\frac{1}{4}}\mu^{\frac{7}{16}}(Z\tilde{\Lambda}\tau)^{-\frac{1}{8}}$	$\Phi^{\frac{1}{2}}\lambda^{-\frac{1}{2}}\mu^{\frac{7}{4}}(Z\tilde{\Lambda}\tau)^{-\frac{1}{4}}$	$\Phi^{\frac{1}{2}}\lambda^{\frac{1}{2}}\mu^{\frac{1}{8}}(Z\tilde{\Lambda}\tau)^{\frac{1}{4}}$
Mora – B	$\Phi^{\frac{7}{9}}\lambda^{-\frac{2}{9}}\mu^{\frac{7}{18}}(Z\tilde{\Lambda}L)^{-\frac{1}{9}}$	$\Phi^{\frac{5}{9}}\lambda^{-\frac{4}{9}}\mu^{\frac{7}{9}}(Z\tilde{\Lambda}L)^{-\frac{2}{9}}$	$\Phi^{\frac{4}{9}}\lambda^{\frac{4}{9}}\mu^{\frac{2}{9}}(Z\tilde{\Lambda}L)^{\frac{2}{9}}$

Mora's models arise from the inverse bremsstrahlung absorption mechanism; in all three models $\mu = A/Z$.

The model due to Manheimer *et al.* is most appropriate for long wavelength, high intensity experiments with large spot size. Inverse bremsstrahlung is dominant at low intensities and short laser wavelengths, where Mora's models apply. Spherical expansion (Mora–B) is more appropriate to small laser spots and long pulses, while planar expansion (Mora–A) applies in the opposite case. Our experimental conditions fit the Mora–B model; however, the simulations are constrained to planar geometry and therefore should be represented more accurately by the Mora–A model.

As can be seen from the table, there is remarkably little variation of the power law coefficients among the different models for the intensity scaling. The ablation pressure, the quantity of the most interest, is found to scale as, $P_{abl} \sim \Phi^{0.7-0.8}$. As noted above, the material dependence enters through the factor $\mu = A/Z$; however, for moderate Z materials which are fully ionized $A \simeq 2Z$, so $\mu \simeq 2$ is a constant. The fact that the scaling laws are relatively insensitive to details of the specific model used to derive them suggests that the ablation process depends only on the *laser* parameters in a very general fashion, and it is also largely material independent. This is an important aspect because it was not possible to obtain a direct measure of the ablation pressure in the experiment (independent of the shock measurement).

On the other hand, an effective laser intensity (Φ_{60}) can be measured. This is used to yield an estimate of the pressure using the models. Comparison of the computer code with analytic models is therefore useful to assess the accuracy of this estimate.

In Figure 4-7 the predictions of LTC are compared to the analytic models of Mora in Table II which are most appropriate for the conditions in the simulations and the experiment. Simulations were performed at 3 different intensities ($2 \times 10^{12}, 1 \times 10^{13}$, and 5×10^{13} W/cm^2) spanning more than a an order of magnitude. The peak values of the ablation pressure, temperature at the point of peak laser absorption, and mass ablation rate were determined from the simulations and plotted as the open symbols in the figure. The solid lines indicate the predictions of Mora's analytic models. As can be seen there is agreement in both the exponents and magnitudes of the predictions, thus lending support to the numerical model. The circles are from simulations run without radiation transport and losses, while the squares correspond to the set of simulations which included radiation diffusion. It should be noted that radiative effects were not explicitly included in any of the analytic models, so that the agreement should be better for the simulations without this effect. When radiation is included the ablation pressure and plasma temperature are slightly lowered owing to the cooling effect of the radiative losses. The mass ablation rate increases however because of the additional heat flux due to radiative transport into the cold solid.

4.4 Target Compression

4.4.1 Details of compression

The profiles presented in Figure 4-6 give a picture of the target condition at a single instant in time. Much qualitative insight can be obtained by examining how several of the hydrodynamic variables such as ρ and T vary as a function of both

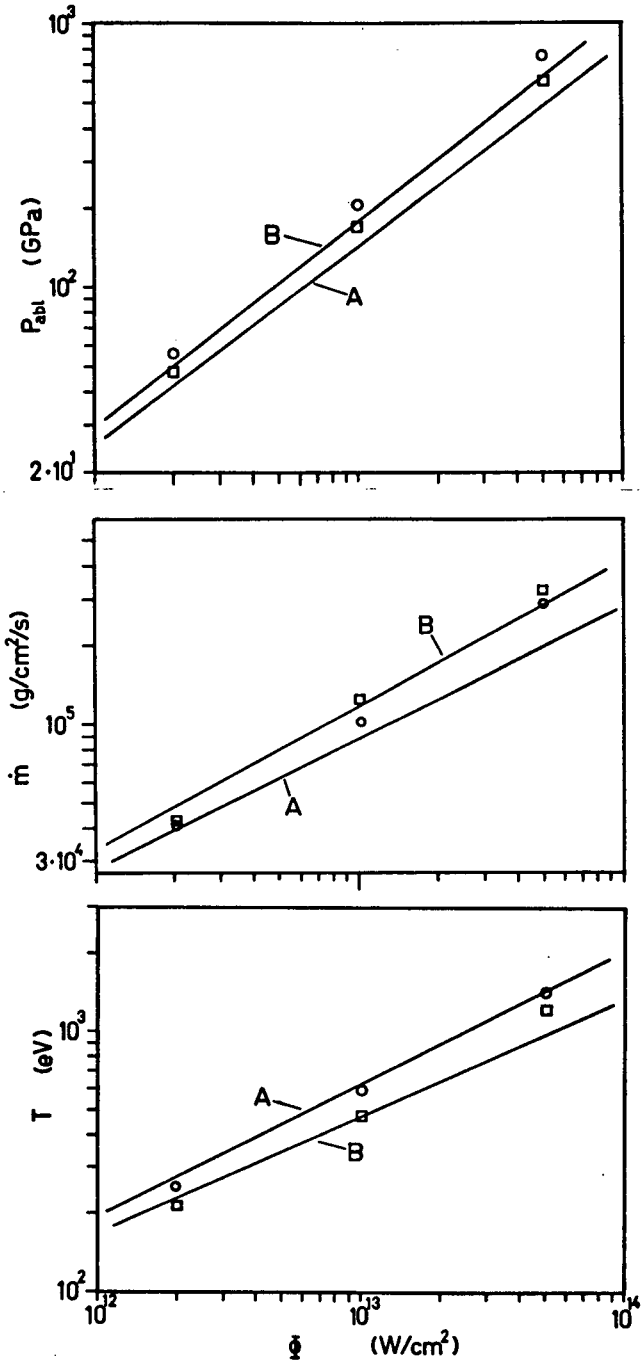

Figure 4-7 Comparison of LTC predictions with analytic scaling laws for ablation pressure P_{abl}, mass ablation rate, $\dot{m}$ and corona temperature, T. Solid curves corresponding to Mora–A and Mora–B models are indicated. Open circles are from the "standard" calculation, open squares are from the "standard" calculation with radiation diffusion added.

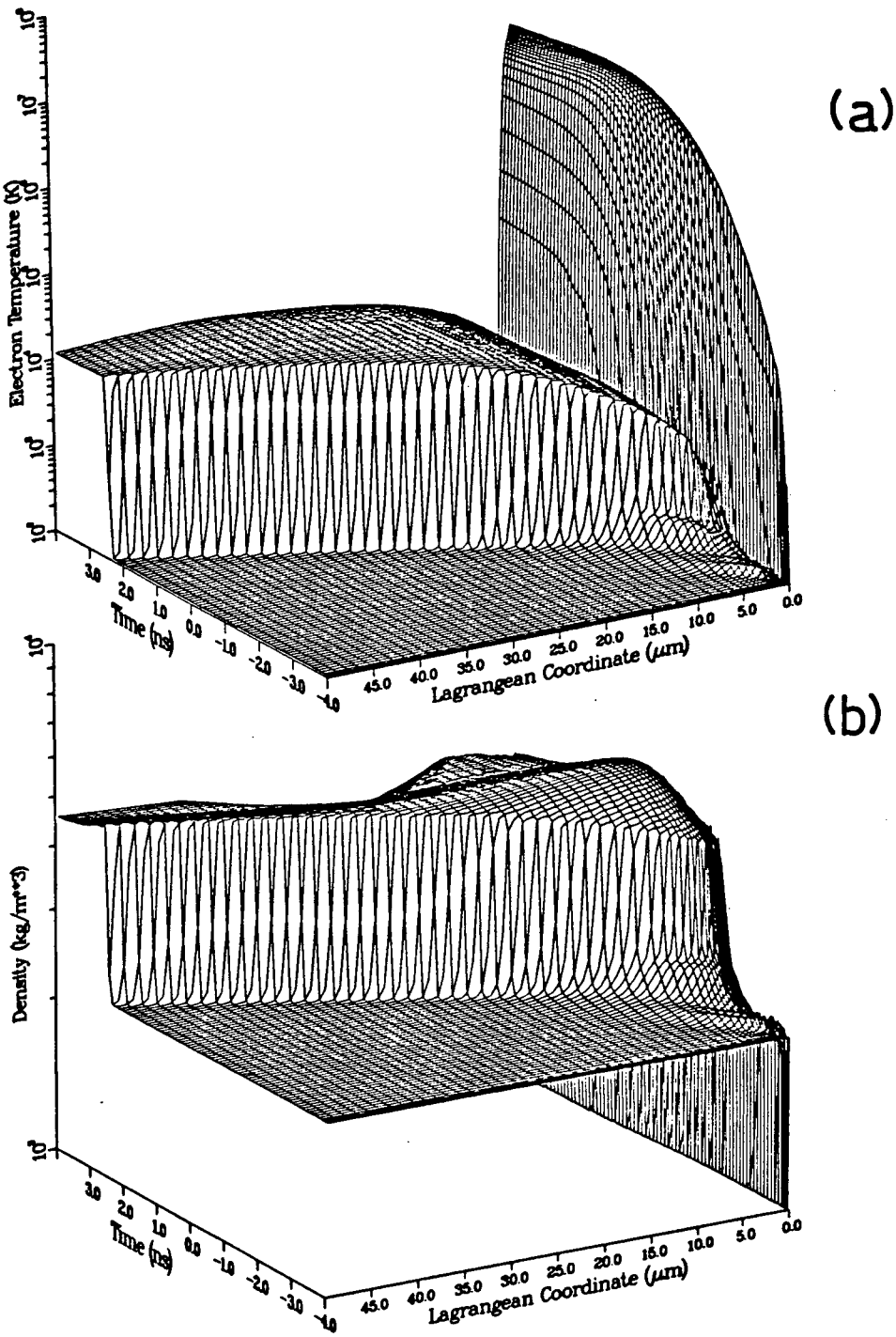

Figure 4-8 Three-dimensional plots of (a) temperature, and (b) density throughout the target and during the duration of the laser pulse.

time and space throughout the target. This information is plotted conveniently in Figure 4-8 in the form of a three dimensional surface. The vertical axis represents the quantity of interest (such as ρ in Figure 4-8b) while the horizontal plane is formed by the time axis and the Lagrangean coordinate representing different regions of the target. At the surface of the target (Lagrangean coordinate ~ 0) is the ablation region and coronal plasma. In Lagrangean coordinates this comprises a very small fraction of the total mass as the ablation front penetrates only a few microns into the target. The spatial dimension of the ablation plasma extends hundreds of microns from the surface due to the low densities. Clearly evident in these plots is the shock wave which is formed soon after the heating begins. Of particular importance is the fact that the shock wave is not steady in the early stages of its formation. This is because the ablation pressure is nearly proportional to the instantaneous laser intensity which is not constant in time: the laser pulse has a gaussian shape, and the driving pressure rises and falls on the same time scale with a similar pulse shape. The most important consequence of this kind of pressure loading is that the pressure at the shock front does not reach its peak value until the wave has propagated several tens of microns into the target. The layers near the surface of the target are not shocked to the peak pressure, but are shocked initially to a lower pressure and then compressed nearly isentropically as the pressure continues to rise. The clearest indication of this is shown in Figure 4-8a where the temperature distribution within the target is not uniform, but increases from a very low value to a plateau essentially at the Hugoniot value for the peak pressure. Thus, a substantial portion of the target is compressed quasi-isentropically rather than by shock. The plot of density shows a much more uniform distribution since density is not a very strong function of temperature (or entropy) in the solid state. Even then, the effect of the isentropic compression near the surface is evident in the slightly higher densities reached there.

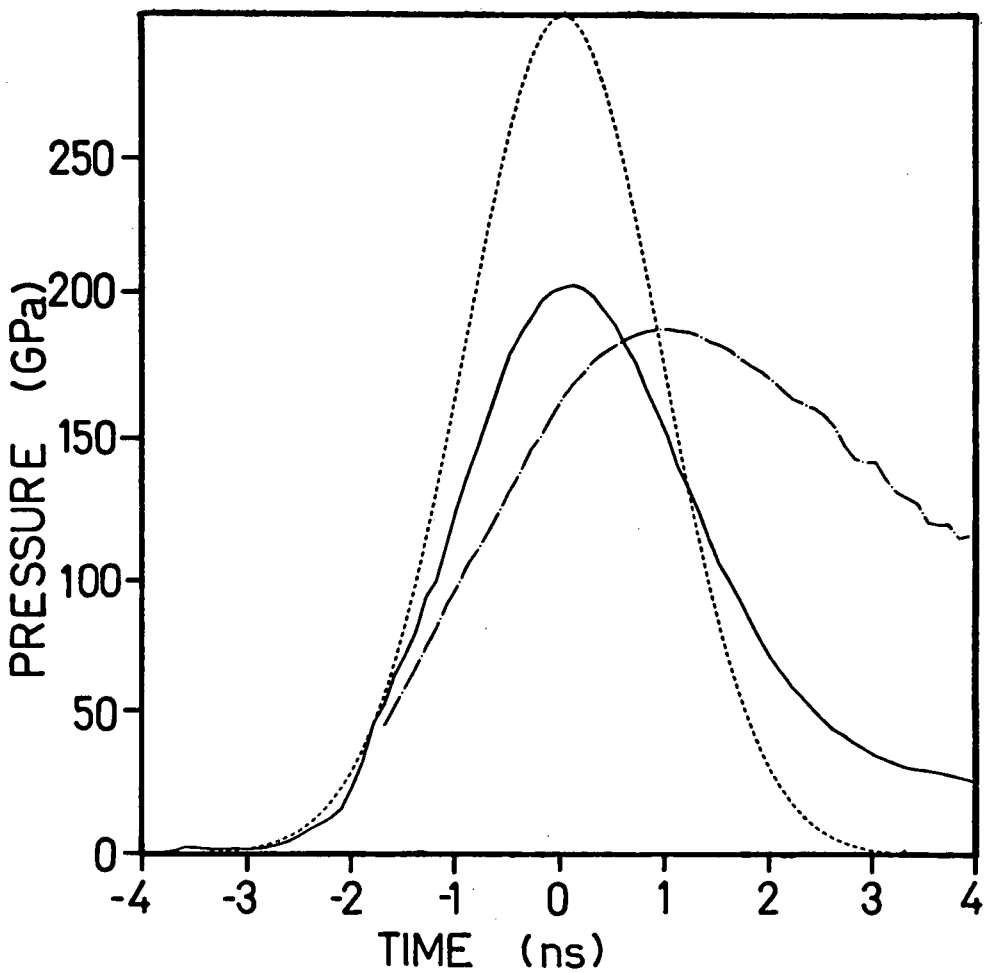

Figure 4-9 Pulse shapes of laser intensity, ablation pressure and shock pressure. The solid curve is the ablation pressure; the dot-dashed curve is the shock pressure; and, the laser pulse is shown for comparison (arbitrary units) by the dotted curve. The peak laser intensity was 1.0×10^{13} W/cm^2.

The plots in figures 4-9 and 4-10 give more quantitative information related to the compression process. In Figure 4-9 is a plot of some pulse shapes derived from the simulation. The gaussian laser pulse is represented by the dotted curve. The ablation pressure shown by the solid curve was defined to be the pressure in the target at the bottom of the heat front. As can be seen from Figure 4-6, this is the region where the maximum pressure develops. Also shown is the pressure at the shock front (dot-dashed curve) propagating into the target. Note that at early times before the peak of the laser pulse the shock pressure is substantially less than the pressure at the ablation front. The shock front is spatially separated from the ablation front and material between the shock and ablation front sustains a smooth pressure gradient defined by these two values. After the peak of the laser pulse the ablation pressure drops quickly, but the pressure at the shock front drops more slowly. At late times a decaying shock propagates into the target.

Figure 4-10 gives a quantitative picture of the density, temperature and pressure time histories of selected Lagrangean fluid elements or cells within the target (this information is already present in Figure 4-8). This plot illustrates clearly the nature of the compression process for Lagrangean elements near the target surface. The initial temperature rise occurs mainly due to the shock transition. The smooth compression to the peak pressure at later times is accompanied by a relatively small temperature increase. The peak density of the cooler layers is also higher. The pressure profile near the surface follows the ablation pressure profile, because of the close proximity of the ablation surface. In the deeper layers the pressure history more closely approximates that of a decaying shock.

As another variation, the same information can be presented as in Figure 4-11 which shows a plot of the trajectory of selected Lagrangean cells on the $T - P$ plane for simulations at 1×10^{13} and 5×10^{13} W/cm^2. Also plotted is the temperature along the principal hugoniot (dot-dashed curve). Compression of a Lagrangean element begins on or near the principal Hugoniot and then follows an isentrope

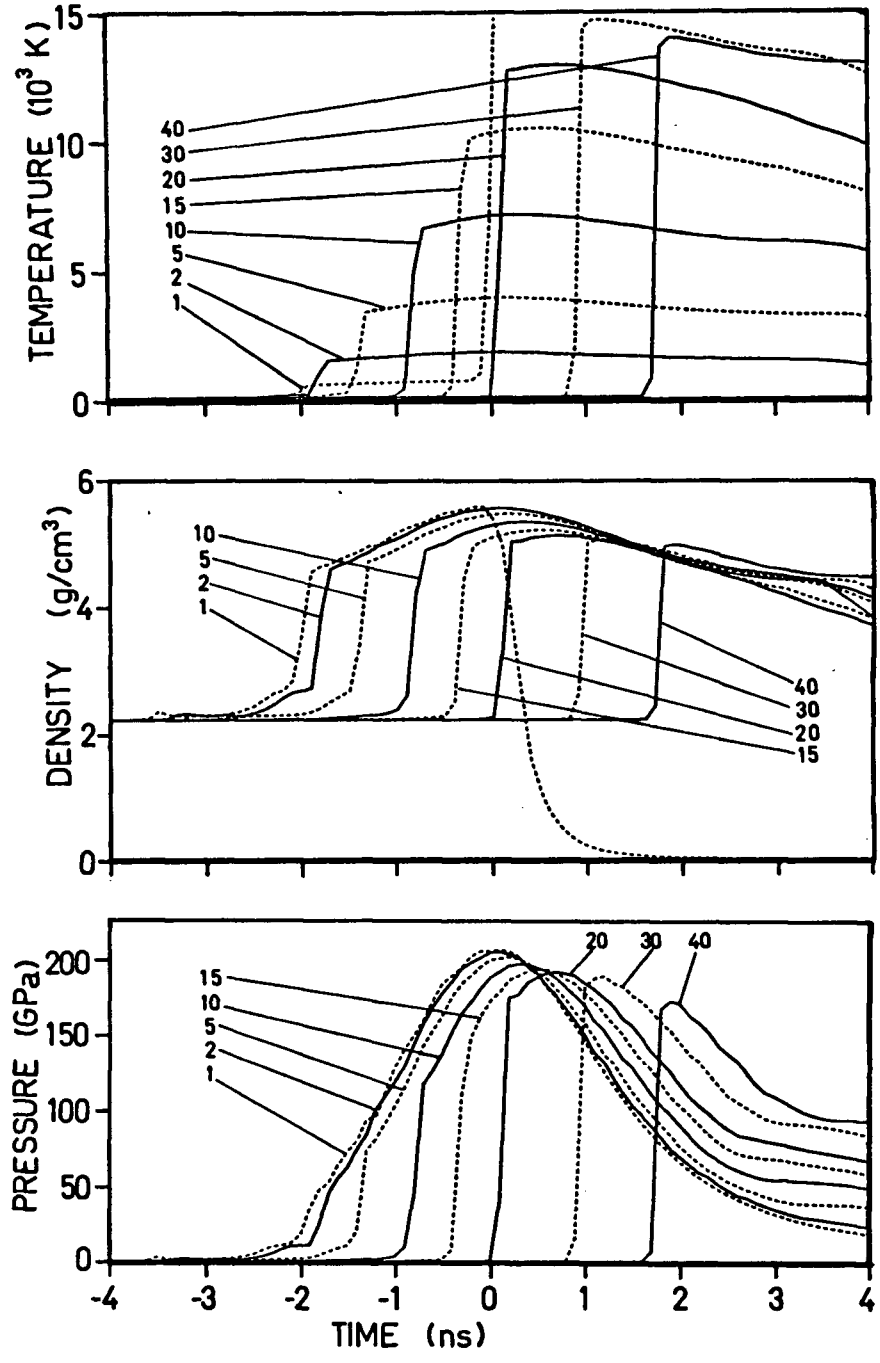

Figure 4-10 Density, temperature and pressure as a function of time for selected lagrangean elements within the target. The lagrangean coordinate (depth in the target in μm units) is indicated for each curve.

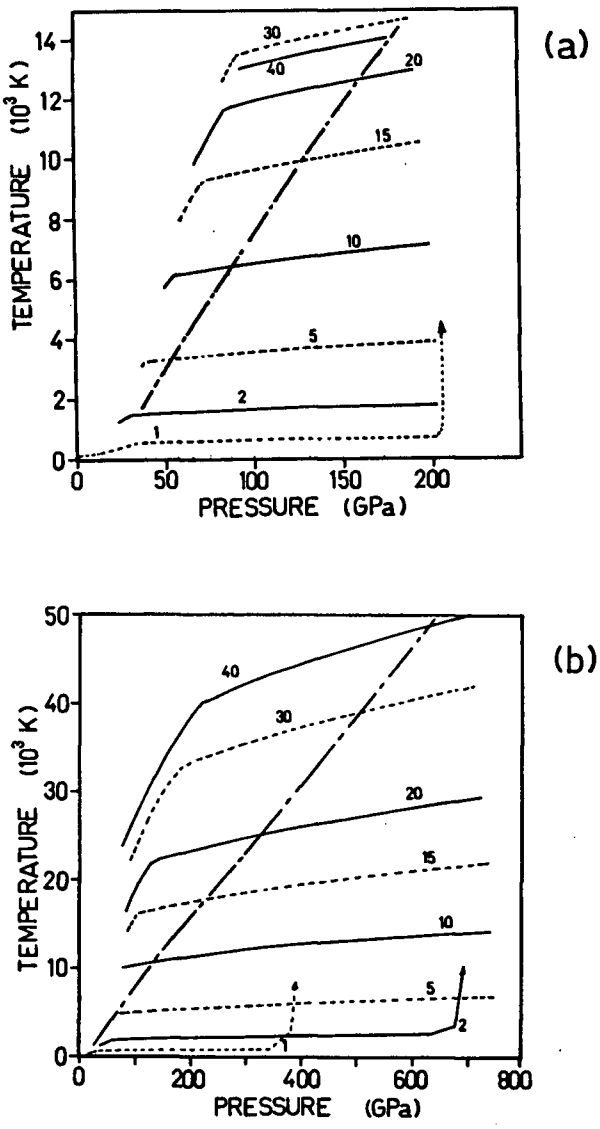

Figure 4-11 Trajectory of Lagrangean elements in the it T-P plane during the laser pulse. (a) 1×10^{13}W/cm^2 and (b) 5×10^{13}W/cm^2. The Lagrangean coordinate depth in μm units is indicated for each curve. Temperature along the principal Hugoniot is indicated by the dot-dash curve. Note the difference in scales between the two plots.

to the peak pressure ($\sim$ 200 GPa in 4-11a and $\sim$ 700 GPa in 4-11b). Following the peak of the pulse the trajectory follows the isentrope back down towards low pressures. The main point of interest in this representation of the compression process is the fact that a very wide range of thermodynamic states is sampled. Conventional shock experiments reach single states on the Hugoniot (dot-dashed curve), or a locus of states along isentropes to lower pressure (released states). Double shock experiments can be used to extend the region of phase space that is sampled, (since the second shock hugoniot is close to the isentrope passing through the first shock state). The ramp wave loading, such as with the gaussian laser pulse, is analogous to an ensemble of double shock experiments since it drives a shock of gradually increasing amplitude with further compression behind the shock following an isentrope. Thus it samples a wide range of isentropic paths *in compression* up to the peak pressure in a single shot.

The $T - P$ plot is also of particular relevance to the question of a new phase transition in SiO_2, which was discussed briefly in §2.6. The isentropic paths shown in the figure are well-suited to exploring high pressure, low temperature regions of the $T - P$ plane where phase boundaries may exist well away from the principal Hugoniot. However, the plot shown in Figure 4-11 is only an idealized version of the gaussian pulse compression process. Other effects need to be considered in experiments. It will be seen in chapter 5 that the experimental data indicates that the compression process appears to be much more complicated, beset with non-equilibrium effects. Moreover, radiative preheat can modify the picture because layers closest to the target surface, which are on the lowest isentropes, are also the ones heated most strongly. Radiative preheat will be discussed in §4.5.3.

4.4.2 Trajectories

The main experimental observable in this work is the shock trajectory. However, extracting shock trajectories from the simulations is somewhat arbitrary due

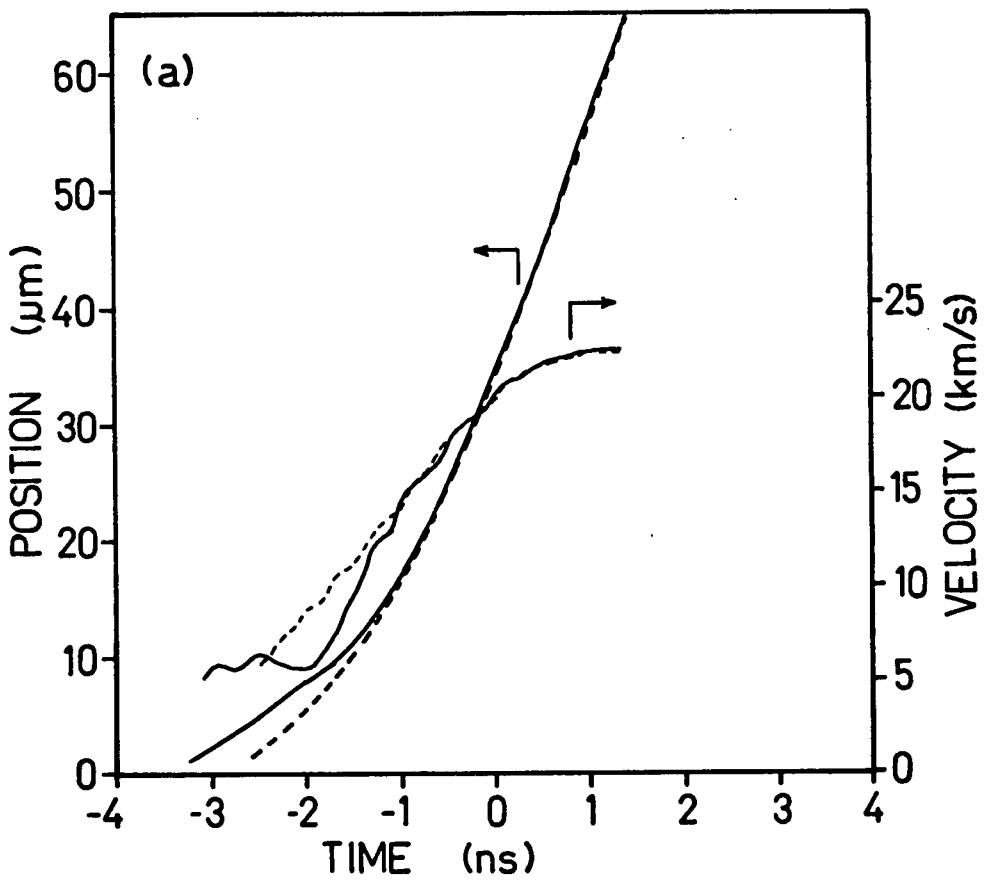

Figure 4-12 Shock trajectories on the x-t plane. The solid curve is approximately the leading front of the compression, at $\rho = 2.3$ g/cm^3; the dashed curve represents the stishovite compression wave, at $\rho = 4.0$ g/cm^3. (a) Laser intensity 5×10^{13} W/cm^2. (b) and (c) shown on the next two pages.

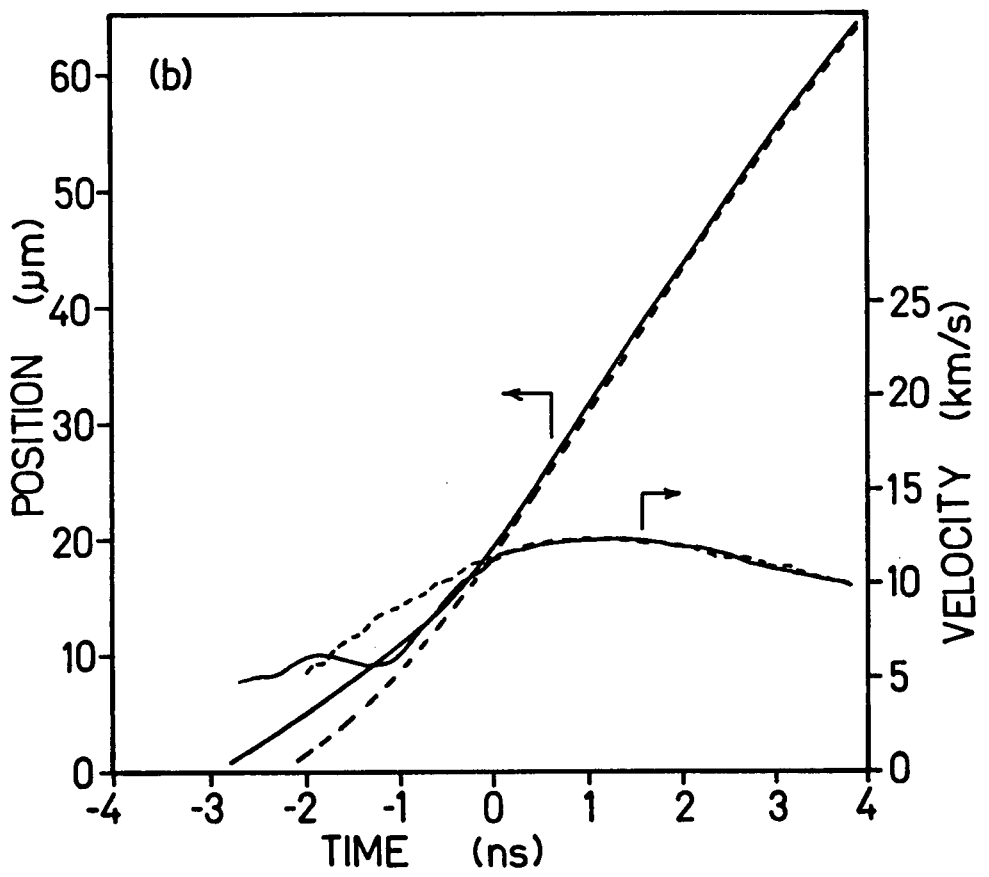

Figure 4-12 (continued) (b) Laser intensity 1×10^{13} W/cm^2.

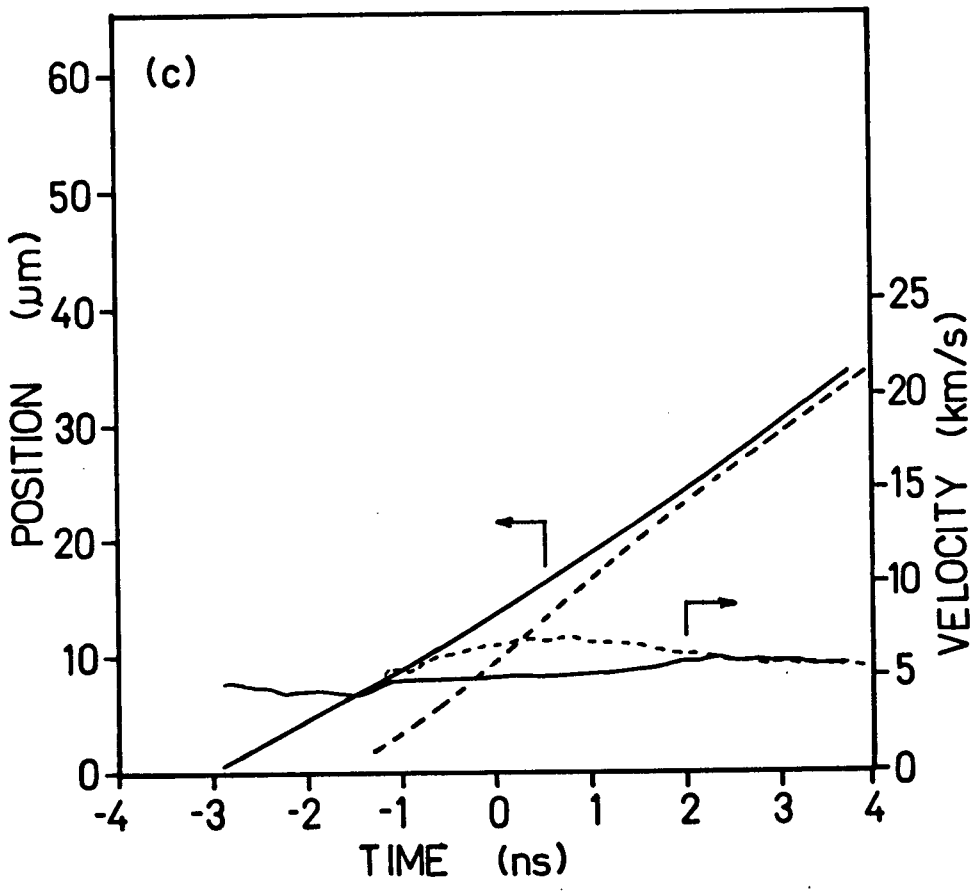

Figure 4-12 (continued) (c) Laser intensity 2×10^{12} W/cm^2.

to the complexities introduced by the stishovite transition, and the fact that the shock forms gradually in its early stages. In Figure 4-12 is a plot of shock trajectories obtained at intensities of 2×10^{12}, 1×10^{13}, and 5×10^{13} W/cm^2, which span the experimental intensity range. In this figure, as well as all subsequent trajectory plots, the spatial origin is at the target surface (position $x = 0$), and the time origin at the peak (or centroid) of the laser pulse (time $t = 0$). This is the same convention used for the display of all the reduced data trajectories, such as the example in Figure 3-7. The figure shows trajectories and velocities corresponding to the $\rho = 2.3$ g/cm^3 and $\rho = 4.0$ g/cm^3 density contours on the $x - t$ plot. The lower density reflects the low pressure elastic wave propagating into the target during the initial portion of the laser pulse, while the higher density is characteristic of a point midway through the stishovite transition. Beyond a certain point both trajectories coalesce and only a single shock front propagates into the material.

Some details of this figure should be noted, for comparison with the experimental measurements later. The elastic-plastic flow regime (or mixed phase region), where a two-wave structure exists, appears to be of little significance in the simulations at high intensities. Evidently the early transient phase, where the elastic wave outruns the main pressure front, lasts for a very short time for intensities of 10^{13} W/cm^2 or greater. This is simply because the peak pressures reached at these intensities (> 150 GPa) are quite large compared to the characteristic pressure of the stishovite transition, which is 10 - 30 GPa. The ablation pressure exceeds the stishovite transition pressure at a very early time in the laser pulse. This would imply that one should observe a smoothly accelerating, well-defined shock front emerging at a depth of 10 - 15 μm in the target. At the lowest intensities the peak pressures exceeds the stishovite transition pressure only marginally, so that the high density front catches the elastic front quite late in the laser pulse. By this time the applied pressure is decaying rapidly so that the shock front only barely becomes a single step transition (if at all). The propagation speed of the shock front at

these intensities is slightly above the sound speed. The transition between the two-wave behaviour and the high pressure single wave behaviour occurs at intensities somewhere around 2×10^{12} W/cm^2.

4.4.3 Shock speed scaling

For high enough shock pressures $P \sim D^2$. This may be combined with the ablation pressure scaling, $P \sim \Phi^{0.78}$, to obtain a scaling for shock speed against laser intensity, roughly, $D \sim \Phi^{0.39}$. Figure 4-13 shows a plot of the peak shock speed versus laser intensity derived from the simulations in similar fashion as Figure 4-12. The solid line drawn through the points fits a $\Phi^{0.37}$ dependence. This representation of the simulation results is useful because it can be compared directly to the experimental data as a means of assessing consistency between experiment and simulation. This comparison will be made in chapter 5.

4.5 Modifications to the standard calculation

Several variations on the standard calculation were tested to assess their effect on the experiment. These variations included calculations using the two-temperature description, calculations with the radiation diffusion transport, calculations with X-ray preheat terms added to the energy deposited, and finally calculations using the other two EOS tables, 7381 and 7382. Although some of these variations may produce significant effects in the coronal plasma, the main concern was to evaluate the effects on the main experimental observable, i.e. the shock trajectory. It is found that all of these variations produced little effect on the final computed trajectories, thus justifying the assumption that the "standard" calculation contains the most important ingredients in the physical model and thus provides a reasonably complete picture of the laser-target interaction.

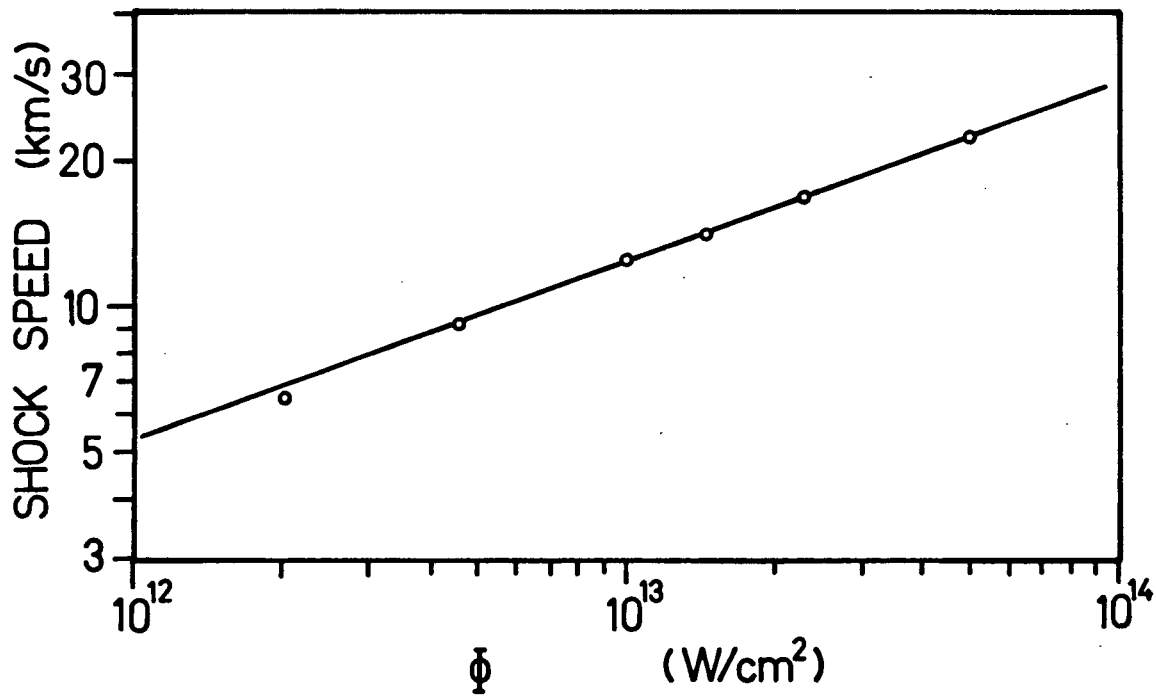

Figure 4-13 Shock speed scaling with incident laser intensity from LTC calculations.

4.5.1 Two-temperature calculations

Several two-temperature plasma calculations were performed. Figure 4-14 shows a plot of the hydrodynamic profiles for a calculation with laser parameters identical to that used in the standard calculation, but with the EOS in the two-temperature version. This may be compared with the profiles in Figure 4-6. In the two-temperature description the ions and electrons exchange energy at a rate given by equation $[4-10]$. This rate is density dependent and is very high for the dense solid. In the rarefied coronal plasma the rate is much lower. In fact it is insufficient to maintain thermal equilibrium between the two species so that the ion temperature in the expanding plasma is lower than that of the electrons. The main difference expected in comparing this with the single temperature description is that the electron component, which absorbs the laser energy, would have a higher temperature since the heat capacity of the electron component is less than the total heat capacity. This would lead to modifications in the absorption, pressure, and density profiles since a variety of coefficients and processes are temperature dependent in the model.

In practice, the two-temperature and single temperature results are nearly indistinguishable. This is because the electron component contributes to nearly all of the heat capacity in the plasma. For moderate to high values of atomic number, $Z \geq 10$, the plasma is ionized to the extent that the electron number density in the corona is a factor of ten or more larger than that of the ions. The two-temperature description is only important for low Z plasmas (e.g. CH), or for studying processes where the ion temperature is needed for the interpretation (e.g. some parametric instabilities).

4.5.2 Radiation Transport

The simple radiation diffusion model that was incorporated into the code was used to estimate the magnitude of radiation transport effects on the experiment.

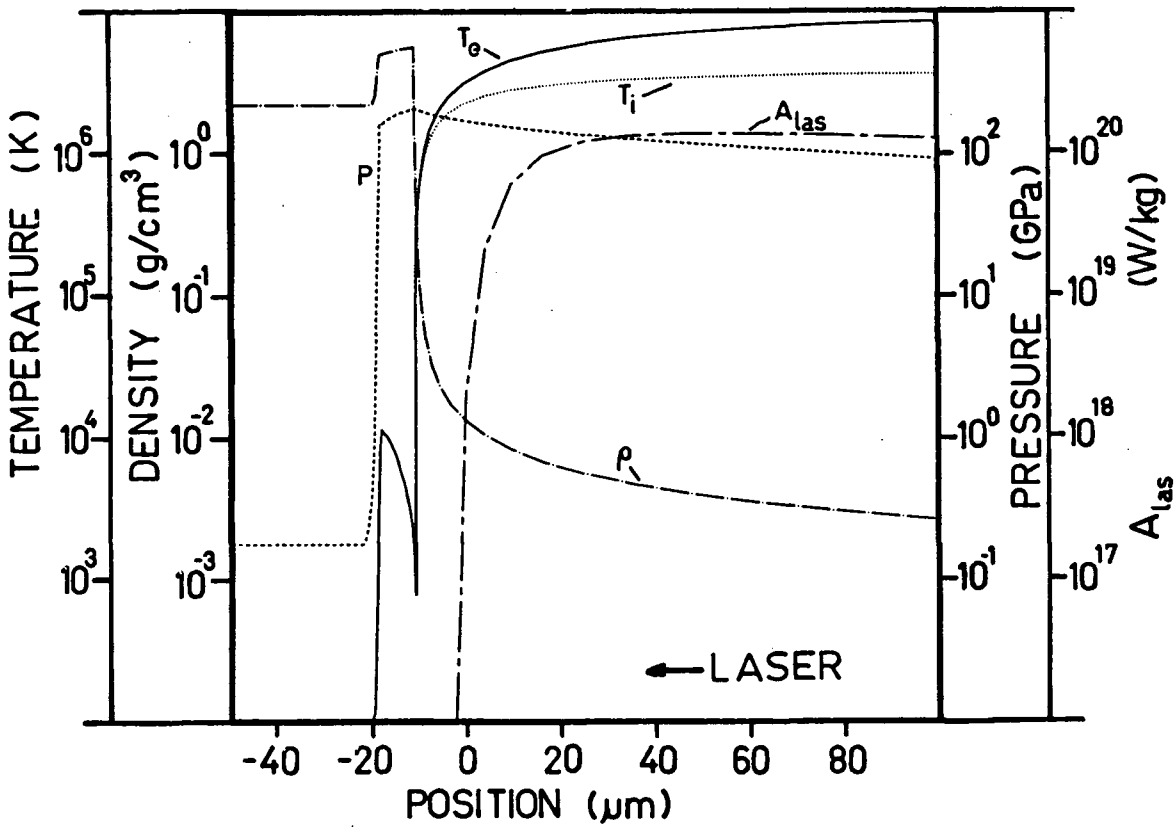

Figure 4-14 Snapshot of hydrodynamic profiles at the peak of the laser pulse for the two-temperature version of the "standard" calculation. Indicated are: electron temperature T_e; ion temperature, T_i; density, ρ; pressure, P; and, absorbed laser power, A_{las}.

Radiation effects begin to become important for short wavelength laser irradiation ($\lambda \leq 1$ μm) and for high Z targets ($Z > 10$). For our conditions of $Z = 10$ and $\lambda = 0.53$ μm these effects may still be regarded as a perturbation of the standard calculation.

The diffusion model used in LTC ignores most of the rich detail of the radiation spectrum and energetics in the plasma, which can become quite complex to treat accurately. In general the accuracy of this description may therefore be inadequate. On the other hand, Schmalz *et al.*[121] believe that this approximation is adequate for estimating global quantities such as radiative loss, effective radiation temperature, and ablation pressure, as well as the heating of the dense target due to radiation diffusion. A detailed discussion and comparison of this radiation diffusion model with more detailed calculations is given in their work[121]. The main purpose of the calculation here was to estimate the effects of radiative losses and transport on the shock compression processes deep in the target.

Figure 4-15 shows a plot of the hydrodynamic profiles obtained from the standard calculation with the radiation diffusion approximation included. The main feature introduced by radiative transport is a radiation heat wave[122–124] propagating into the cold target. This modifies the density and temperature profiles to produce the double jump in temperature and density. The reason for this structure is that the radiation mean free path exceeds the electron mean free path in the dense heated region between the low density corona and the cold solid. This pronounced structure is partially an artifact of the use of a single Rosseland averaged mean free path. Calculations with a more detailed method, such as a multi-group diffusion model or equivalent, divide the spectrum into a set of discrete wavelength ranges corresponding to a broad range of mean free paths. This tends to smooth out the sharp structure of the radiation heat wave produced with the single group approximation.

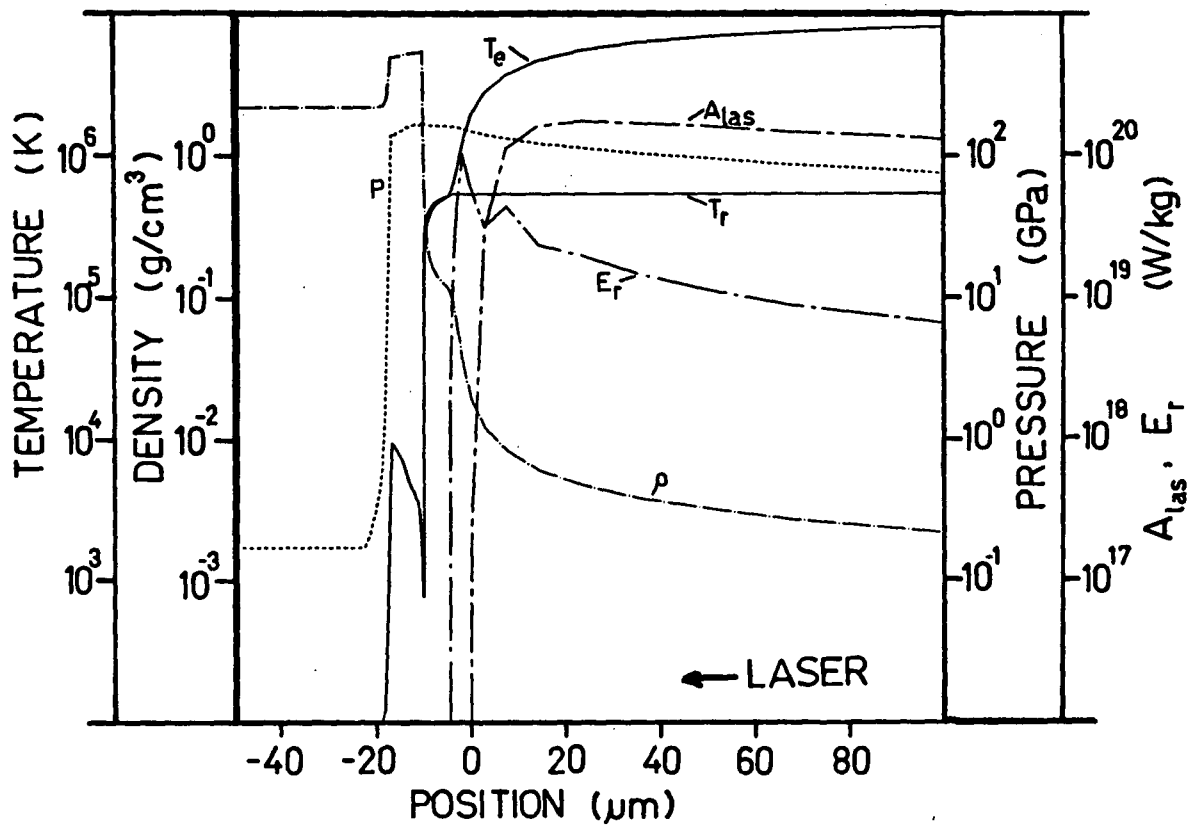

Figure 4-15 Snapshot of hydrodynamic profiles at the peak of the laser pulse for the calculation including radiation transport. Indicated on the figure are: density, ρ; temperature, T; pressure, P; absorbed laser power, A_{las}; radiation temperature, T_r; and, radiative emission power, E_r.

Also shown in Figure 4-15 is the radiative emission profile ($E_r = \partial F/\rho\partial r$). The emission tends to be most intense near and slightly above critical density. Beyond that it drops off sharply towards the cold solid which is strongly absorbing. Radiative emission is a significant loss mechanism and tends to cool the critical density layer to lower temperatures than are predicted without taking into account the radiative processes.

Within the radiation heat wave the radiation temperature and matter temperature are nearly equal, indicating that the material and radiation are close to LTE (local thermodynamic equilibrium) conditions. This is because the radiation heat wave is an optically thick region. In contrast, the low density corona is optically thin, and the radiation field is nearly completely decoupled from the material: the radiation propagates in a free streaming mode outwards into the vacuum. The maximum radiation temperature is restricted to a range of less than $\sim$ 80 eV for the range of intensities examined. This can be understood quite simply: the maximum blackbody flux is $Q_r = 4c\sigma T_r^4$. This value cannot exceed the energy flux, Φ deposited by the laser, so $Q_r < \Phi$, which places a limit on T_r. Thus T_r always tends to be significantly smaller than the matter temperature in the coronal plasma.

Aside from the modification to the density and temperature profile in the ablation region, the addition of radiation to the calculation changes few of the details relating to compression of the target. Radiative losses amount to about 25% of the incident laser energy. These losses remove some of the laser energy from contributing to the thermal pressure in the corona. It should be noted that in experiments with finite focal spot size the radiative losses for low atomic number targets (Z $\sim$ 10), is closer to 10%[114,115,125] of the incident energy. This is probably due to the competing cooling effect of two-dimensional plasma expansion. In the simulations the peak ablation pressure is reduced by a factor comparable to the radiative losses ($\sim$ 25%) because of the cooling effect. The radiation heat wave ablates slightly more of the target material, but the amount of ablated material remains an insignificant

fraction of the total target mass. In the solid shock compressed region, the main difference is simply a slightly lower peak pressure due to the reduced ablation pressure. The basic compression process outlined above remains unchanged because the pressure pulse shape is unaffected by the radiative transport.

4.5.3 Soft X-ray target preheat

In the previous section it was shown that the radiation diffusion model introduces nothing new to the target compression process. However, this model does not take into account the non-LTE aspects of the radiation spectrum, particularly in the high energy tail where long mean free path photons can penetrate deep into the target. Laser-produced plasmas are well-known to produce intense line radiation due to resonant transitions (bound-bound) in ion species characteristic of the plasma conditions[111,113] In aluminum plasmas ($Z_{Al} = 13$) detailed experimental and theoretical studies indicate that up to 1 - 2 % of the laser energy can be converted into line radiation in the energy range 1.5 keV to 2 keV[114–117,125]. These intense features can have significant mean free paths in the solid target (1 - 10 μm) so that radiative preheat is a valid concern in studying target compression. The Si - O plasma ($Z_{Si} = 14$) produces a similar spectrum, thus one may draw on the extensive work done on aluminum to estimate the radiative effects in the SiO_2 targets.

In Table III is a list of the important bound-bound and free-bound transitions expected in the radiating plasma. We are interested primarily in the highest energy photons that are produced in abundance in the plasma. The most abundant ionic species which contribute to the spectrum in the high energy range are the hydrogen-like Si XIV and Helium-like Si XIII. The most important transitions are those between the ground state configuration and single electron excited states. These are the resonant transitions between the electronic configurations indicated in

the table. The strongest lines are the Si XIII $1s^2 - 1s2p$ and the Si XIV $1s - 2p$ transitions, the principal lines in the series. Also associated with the Si XIII $1s^2 - 1s2p$ transition are satellites and intercombination transitions (density and temperature dependent) which also contribute significantly to the radiation field. Another significant radiative process in this energy range is radiative recombination (free-bound) into the ground states of the Si XIII and Si XIV ions. The recombination radiation has a spectral intensity $\propto \exp(-h\nu/kT)$ for $h\nu > h\nu_0$, where $h\nu_0$ is the ionization energy. The spectral range for the recombination radiation is indicated in Table III. Note that all of these emissions are concentrated in the energy range 1860 - 2500 eV. The next major emitting region of the Si spectrum occurs at much lower energy from ionization stages in the L-shell, producing emissions in the range of 50 - 600 eV. Similarly the oxygen K-shell spectra (helium- and hydrogen-like) are near 600 eV as well. Thus there is a large gap in the radiation spectrum below 1860 eV in which only bremsstrahlung emission is present; bremsstrahlung emission is a relatively weak contribution compared to that of the line and recombination emissions.

The cold material opacity for fused silica is shown in Figure 4-16. The energetic line radiation occupies a region of the spectrum where the mean free path (e-folding distance) approaches several microns. Although the radiation field is intense at lower energies as well, the mean free path becomes much less than 1 μm and such radiation cannot penetrate the dense material; hence it need not be considered as a source of preheat. (It is, in fact, this part of the spectrum which is much closer to a thermal distribution and is already partly accounted for in the radiation diffusion approximation.) Therefore, to assess the amount of radiative preheat it is necessary only to consider the effects of the intense line radiation with mean free path of the order of 1 μm or more. This narrows the spectral range of interest to the K-shell transitions of Si XIII and Si XIV, which are listed in Table III.

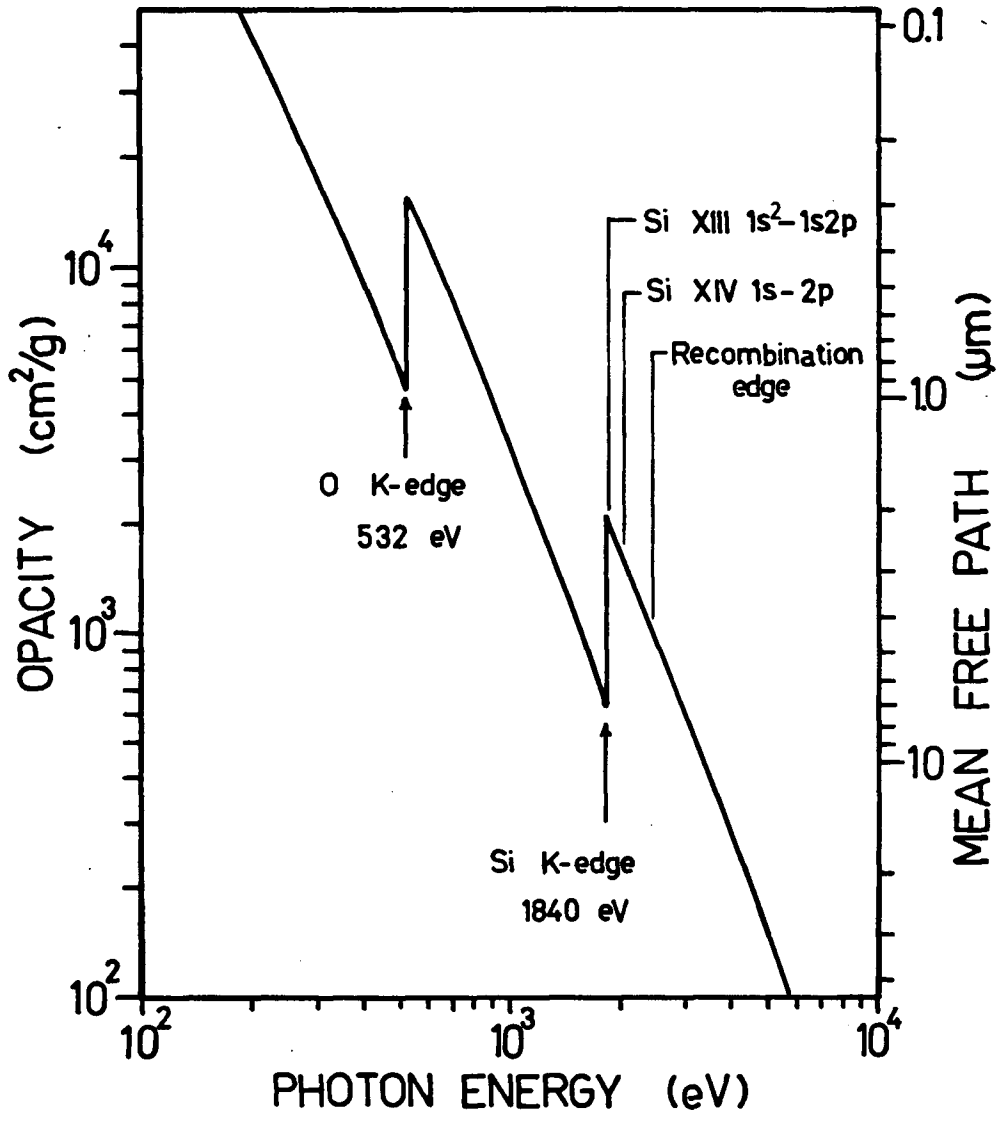

Figure 4-16 Cold material opacity, and X-ray features used in the preheat model.

Table III. Radiative preheat spectral features

Ion	Transition	Energy (eV)
Si XIII	$1s^2 - 1s2p$	1865
	$1s^2 - 1s3p$	2183
	$1s^2 - 1s4p$	2294
Si XIV	$1s - 2p$	2006
	$1s - 3p$	2378
	$1s - 4p$	2508
Si XV	recombination to Si XIV	> 2673
Si XIV	recombination to Si XIII	> 2438

Conversion effciencies of laser energy into radiation for aluminum have been measured to be $\sim$ 10% for total conversion, with $\sim$ 1 - 2 % occupying the K-shell band[114,115,125]. These were measured for conditions similar to those of our experiment. The most detailed planar (one-dimensional) radiation-hydrodynamic calculations available indicate total conversion to be $\simeq$ 27%, with about 3 - 4% occupying the K-shell band, for similar conditions[116,117]. The calculations with planar geometry (one-dimensional) hydrocodes appear to overestimate the conversion. Cooling of the plasma due to two-dimensional expansion probably accounts for a large part of this discrepancy.

An *ad hoc* preheat model was incorporated into the computer calculations in order to estimate the effect of the long mean free path photons originating from the K-shell transitions in the Si ions. Although the model is to a large extent arbitrary, it allows a reasonable assessment of the main effects of X-ray preheat on the compressed target. In this model a power flux, expressed as a fraction of

the incident laser intensity, is assigned to the two strongest features. These are (i) the Si XIII $1s^2 - 1s2p$ resonance line, intercombination and satellites grouped at 1865 eV; and, (ii) the Si XIV $1s - 2p$ resonance line at 2006 eV. In addition a fraction was assigned to the Si XIV - Si XIII recombination spectrum with the recombination edge located at 2438 eV. This scheme distributes the preheat energy over most of the spectral range where there is significant energy; this is important because the effects of preheat are highly sensitive to the opacity (mean free path) which is a strongly varying function of photon energy. It should be noted that this prescription is consistent with two empirical facts: (i) that the emissions of non-thermal radiation tend to follow the laser pulse in time; and (ii), that the radiated energy fraction scales nearly linearly with the laser intensity.

The preheat energy was deposited into the dense region of the target using the known cold material opacity to calculate the deposition as a function of depth. It was assumed that the source geometry was planar, isotropic and located at the critical density surface. For a monochromatic line radiation source of intensity I_0 (power/unit area radiated into a hemispherical solid angle) the deposition into a Lagrangean element Δm, at optical depth τ, and of optical thickness $\Delta\tau = \kappa_\nu \Delta m$ is given by,

$$X_d(\tau) = I_0[E_2(\tau) - E_2(\tau + \Delta\tau)] \qquad [4-31]$$

where X_d is the deposited power and E_2 is the second order exponential integral, which arises from angular averaging of an isotropic source function over the planar geometry. The optical depth τ is given by,

$$\tau(m) = \int_m^{m_{cr}} \kappa_\nu dm$$

where κ_ν is the opacity, and m_{cr} is the Lagrangean coordinate of the critical density surface, which is assumed to be the location of the source.

Deposition of the recombination radiation is slightly more complicated because it must be integrated over frequency dependent source and opacity functions. In this case the opacity has a power law fequency dependence $\kappa(\nu) = \kappa_{\nu_0}(\nu/\nu_0)^{-\alpha}$ where κ_{ν_0} is the opacity at the recombination edge energy, $h\nu_0$. Near the recombination edge the opacity function is fitted accurately by $\alpha = 8/3$. The source spectrum has an exponential frequency dependence $\propto \exp(-h\nu/kT)$. With these relations the generalization of the monochromatic deposition function becomes,

$$X_d(m) = I_0 \frac{h\nu_0}{kT} \exp(h\nu_0/kT) \times \int_{\nu_0}^{\infty} d\nu \exp(-h\nu/kT) \left\{ E_2\left(\tau_0(\nu/\nu_0)^{-\alpha}\right) - E_2\left((\tau_0 + \Delta\tau_0)(\nu/\nu_0)^{-\alpha}\right) \right\}, \quad [4-32]$$

where the optical depth τ_0 is obtained using the opacity value at the recombination edge,

$$\tau_0(m) = \int_m^{m_{cr}} \kappa_{\nu_0} dm$$

Here I_0 should be interpreted as the total power flux radiated over the spectral range $h\nu > h\nu_0$ due to the recombination process. (The exponential factor $(h\nu_0/kT) \times \exp(h\nu_0/kT)$ is a normalization constant to account for the fact that the frequency integral is not over the whole spectrum.)

The intensities (conversion efficiencies) assigned to the lines and recombination spectrum have to be estimated based on empirical knowledge of measured and calculated spectra of Al and Si plasmas. For the Si - O plasma the K-shell emission is expected to be less than that for Al plasmas for two reasons. The overall population density of Si atoms is reduced roughly by a factor of 3 due to the 1/3 molar fraction of Si atoms within the SiO_2 target material. Furthermore, because of its higher atomic number, the Si K-shell spectrum occcupies a higher energy band, $h\nu >$ 1.86 keV, as compared with Al, $h\nu >$ 1.56 keV. This aspect tends to reduce the

populations of the excited levels in the H- and He-like ions roughly in proportion to the Boltzmann factor $\exp[-(h\nu_{Si} - h\nu_{Al})/kT]$, assuming all else being equal.

The preheat model was incorporated into the "standard" problem. Numerical calculations are shown for two cases: (a) total deposited power equivalent to 0.5% of the incident laser power with 0.3% residing in Si XIII $1s^2 - 1s2p$ ($h\nu = 1865$ eV), 0.15% in Si XIV $1s - 2p$ ($h\nu = 2006$ eV), and 0.05% in radiative recombination to Si XIII ($h\nu_0 = 2438$ eV); and, (b) total deposited power equivalent to 1.0% of the incident power composed of the same features listed in case (a) but with the conversion fractions doubled to 0.6%, 0.3% and 0.1% respectively. These conversion efficiencies are roughly consistent with the measured Al values, taking into account the reductions expected due to lower ion populations and larger photon energy. Hydrodynamic profiles at the peak of the laser pulse are displayed in Figure 4-17 for the case of 0.5% total conversion. The preheat affects primarily the layer of material located within approximately two mean free paths of the source region – in this case up to about 5 - 8 μm of the target. The heating drops off very rapidly with depth in the target so that layers much beyond this are largely undisturbed. Figures 4-18 and 4-19 show quantitatively the compression histories of selected Lagrangean elements in the target. These figures may be directly compared with Figure 4-10, which shows the equivalent information for the "standard" problem (no preheat).

One of the motivations for examining the effects of preheat was to see if it would modify the calculated shock trajectory. Several simulations, besides those described here, were performed with various (arbitrary) opacities and conversion efficiencies. In general, the calculated shock trajectories were nearly identical to those obtained without preheat at depths larger than the characteristic depth of the deposition function. That is, preheat has negligible effect on the asymptotic shock trajectory deep in the target. This is simply because the amount of heating produced by the preheat mechanism (up to a few percent of the laser energy) is

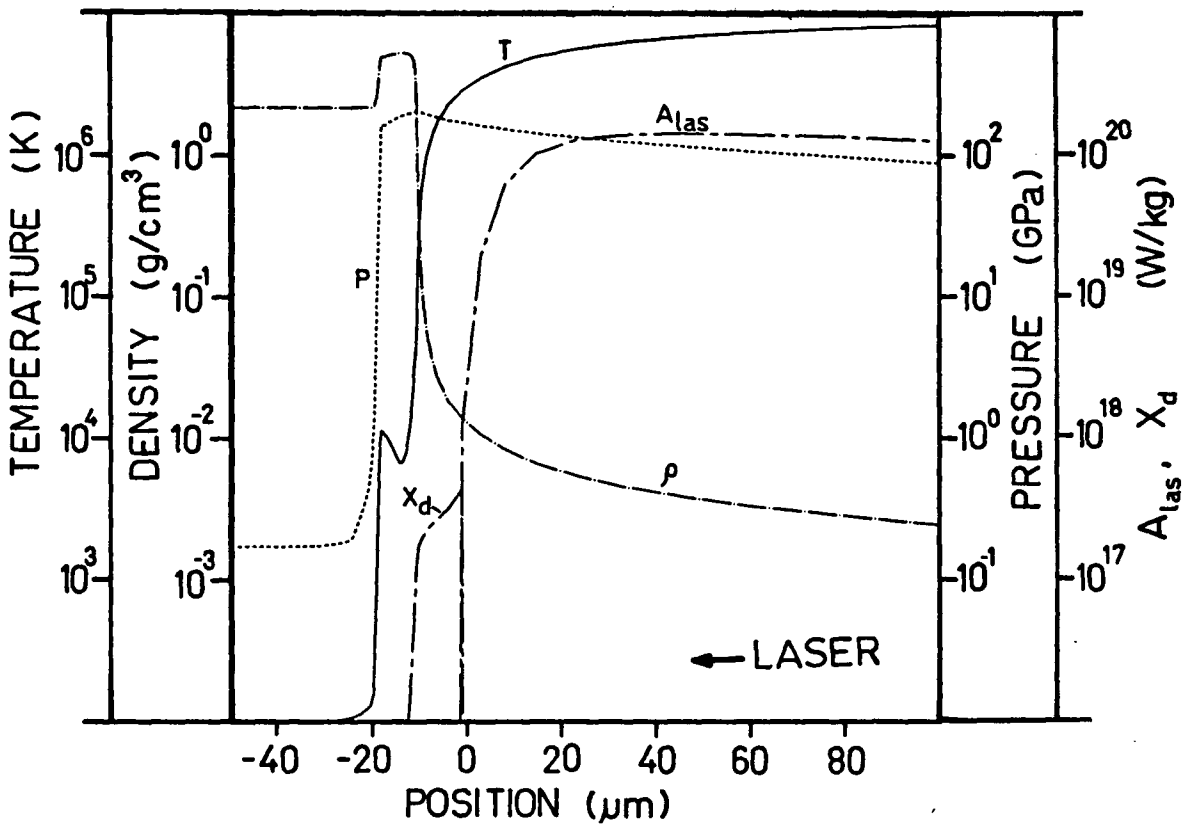

Figure 4-17 Snapshot of the hydrodynamic profiles modified by preheat deposition. Indicated on the figure are: density, ρ; temperature, T; pressure, P; absorbed laser power, A_{las}; and X-ray preheat deposition power, X_d.

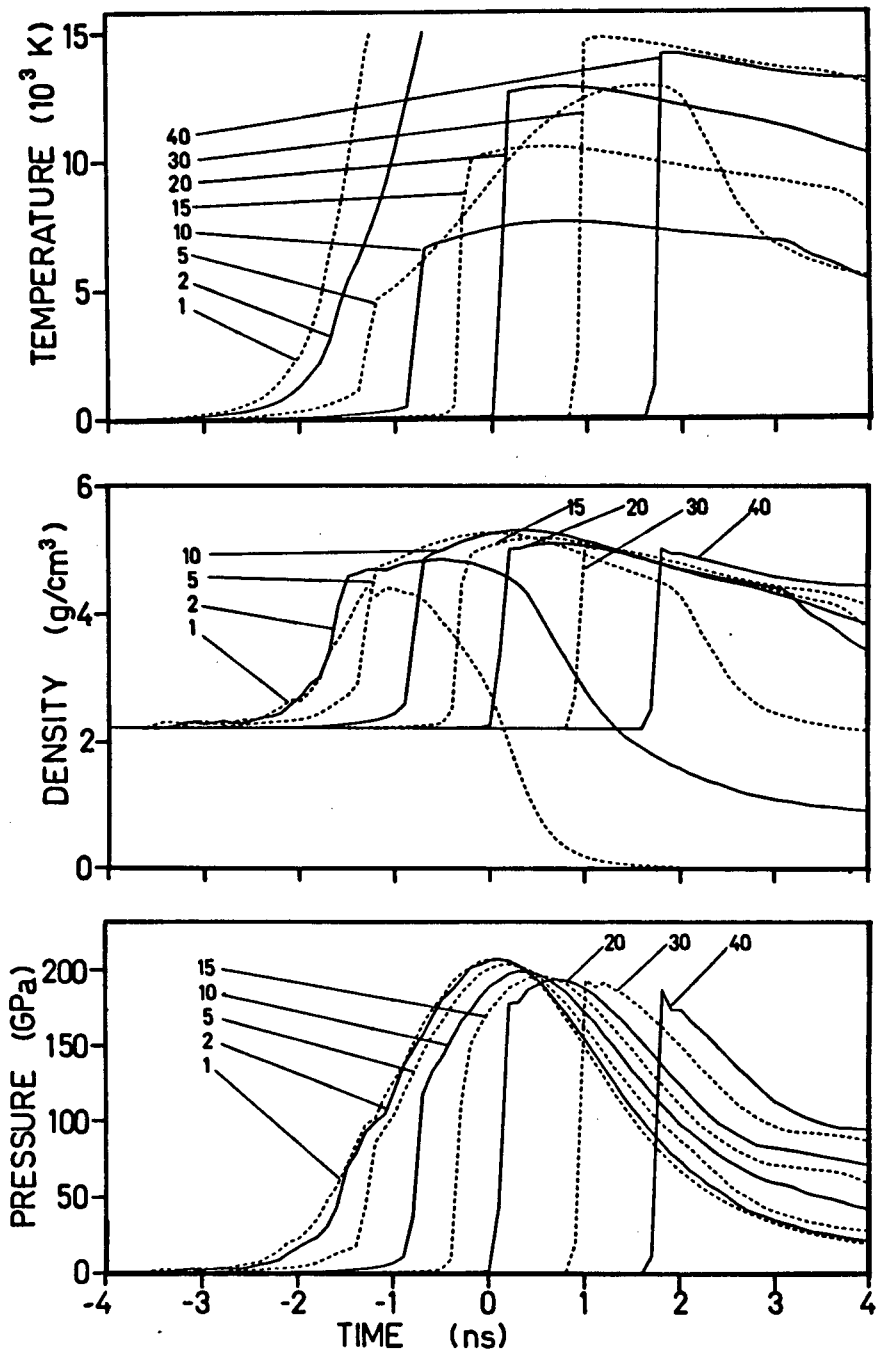

Figure 4-18 Density, temperature and pressure profiles modified by preheat with 0.5% of the laser energy deposited into the dense target region. Each curve represents the evolution of a Lagrangean cell within the target labelled by depth in μm units.

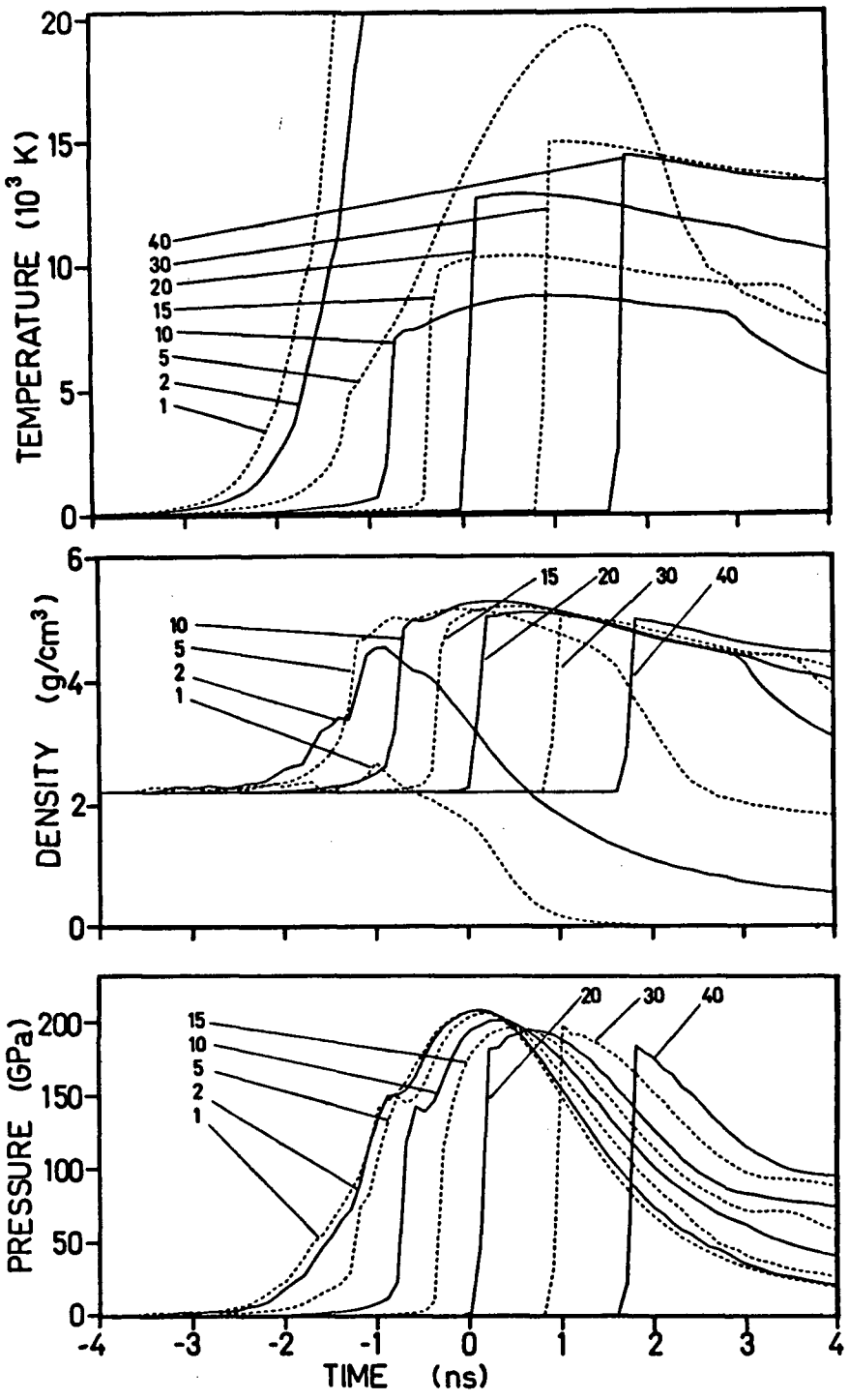

Figure 4-19 Density, temperature and pressure profiles modified by preheat with 1.0% of the laser energy deposited into the dense target region. Each curve represents the evolution of a Lagrangean cell within the target labelled by depth in μm units.

insufficient to change the density of the heated layers while in the compressed state. (This is not true once the pressure is released at the end of the laser pulse.) Of course at the shallow depths where the heating is important, the formation of the shock front appears to be "washed out" by the heating. A true shock does not form until the pressure wave has propagated past the heated layer. Since the heated layer is not very thick this should not be very noticeable in the experiment.

One area where preheat does have a noticeable effect is in modifying the picture of isentropic compression discussed above for the "standard" calculation. In the "standard" calculation the layers closest to the target surface, but not ablated, follow the lowest isentropes. With preheat this is no longer true since these layers are also the most strongly heated. Beyond the 5 - 8 μm preheat depth the isentropic compression process is much less affected, and this is where the lowest isentropes are obtained. The shock does not strengthen to its peak until 20 - 30 μm, so that a significant thickness of material does follow an isentropic compression path once the shock has passed, albeit on isentropes much higher than the lowest ones displayed in the "standard" calculation (*cf.* Figure 4-11).

4.5.4 Comparison of different EOS tables

All the calculations presented so far have used the SESAME EOS table 7380. Two calculations are presented here using tables 7381 and 7382 in place of 7380 for the conditions specified in the "standard" calculation. Table 7382 was designed for α-quartz, hence its reference density is 2.65 g/cm^3. For the calculation the initial density was set to that of fused silica, 2.2 g/cm^3, and the initial temperature to 1430 K (to give a reasonable sound speed and pressure at this density – this temperature is close to the melting temperature of quartz at zero pressure). A comparison of the Hugoniot calculated with the 7382 table centred on this initial state with the Hugoniot curves generated with tables 7380 and 7381 is shown in Figure 4-20. This is plotted on the shock speed-pressure plane, since shock speed is the quantity which

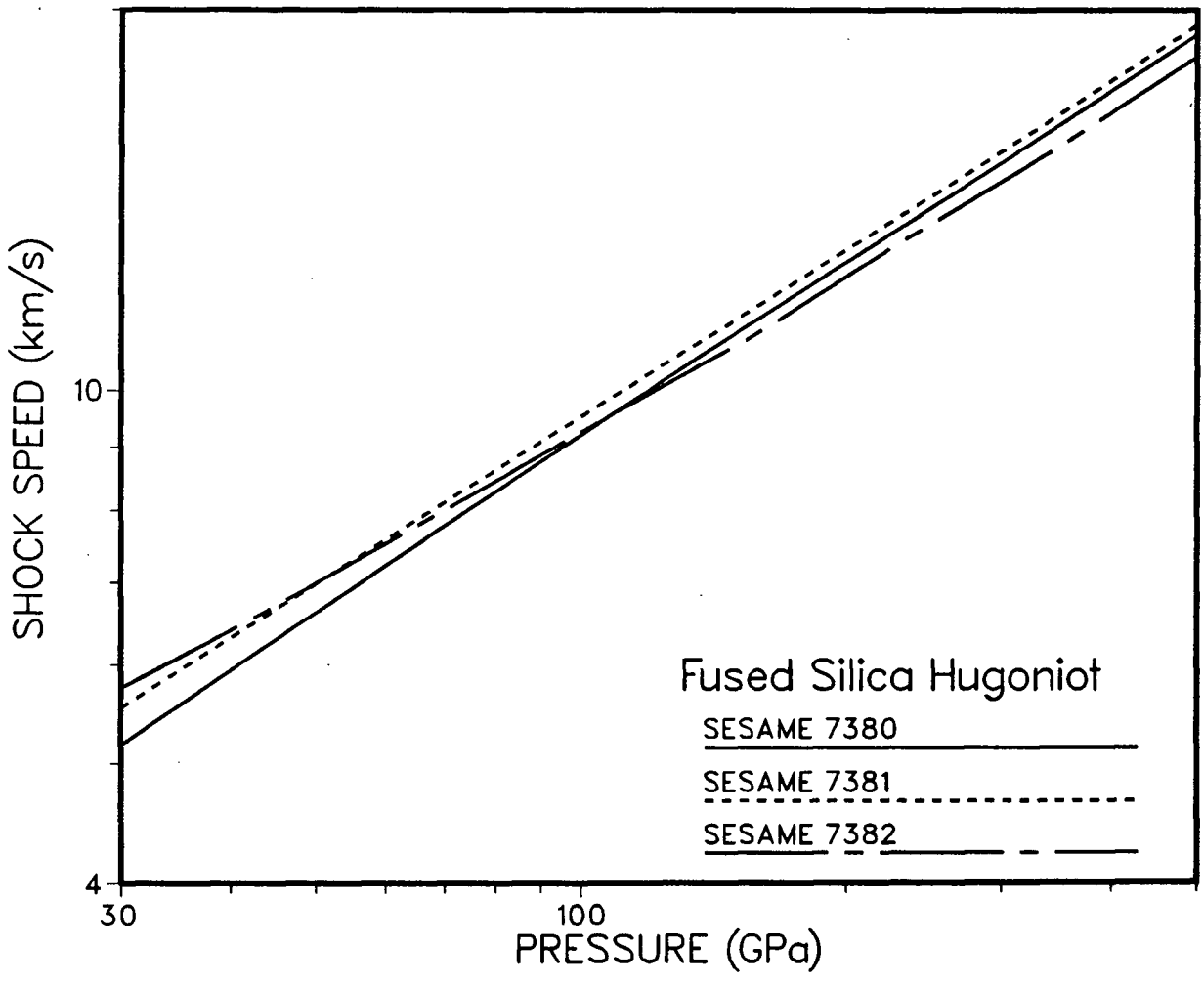

Figure 4-20 Comparison of shock speed versus pressure for Hugoniots generated with SESAME tables 7380, 7381 and 7382 centred on the initial density of fused silica ($\rho_o = 2.2$ g/cm^3).

is directly observed in the experiment. As can be seen from the figure, table 7382 gives a reasonable representation of the fused silica Hugoniot when centred on this initial state.

Detailed comparison of these calculations showed small differences but nothing of any significance. In particular, comparisons were made of the hydrodynamic profiles at the peak of the laser pulse (*cf.* Figure 4-6), the pulse shapes of ablation pressure and shock pressure (*cf.* Figure 4-9) and also the shock trajectory and velocity in x-t space. The comparisons indicate that the simulations produce results that are relatively insensitive to the differences in detail among the EOS tables. The profiles in the coronal plasma were nearly identical among all three calculations, which indicates that the plasma state is well characterized (which is not surprising since it is very nearly an ideal gas). The compressed solid density was slightly higher with the 7382 table, owing to the fact that the Hugoniot of this table is slightly soft above 100 GPa as compared with tables 7380, 7381 and experimental data. This tends to result in a slightly slower shock. Comparison among calculations with tables 7380 and 7381 revealed only very minor differences overall.

Calculated shock trajectories comparing the three calculations are shown in Figure 4-21. The very slight differences among the calculations are insignificant in comparison to experimental uncertainty. For all other calculations in this work only table 7380 was used. The comparisons with the other tables show that no significant differences would be introduced if the calculations were repeated using the other tables.

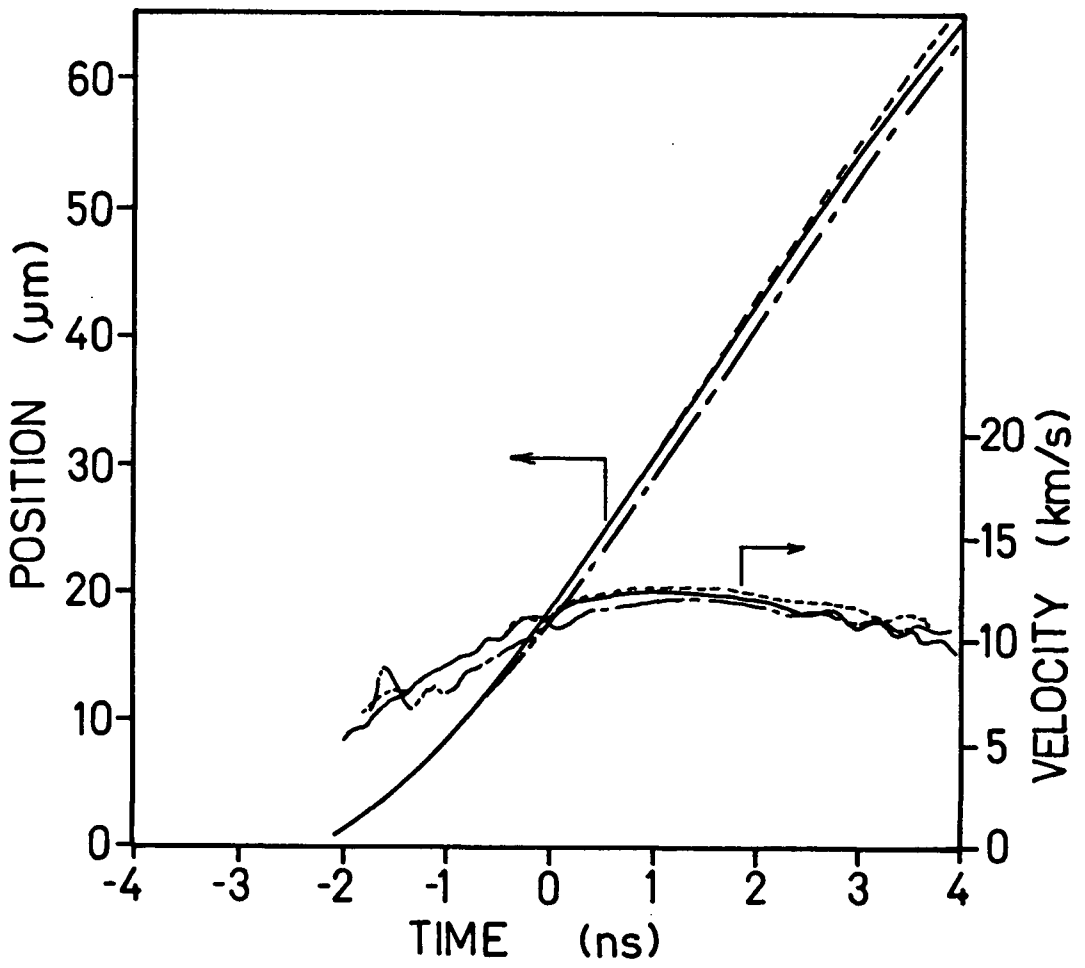

Figure 4-21 Comparison of trajectories among the three SESAME EOS tables, 7380, 7381 and 7382. The trajectories shown represent the $\rho = 4.0 \mathrm{g/cm^3}$ contour, which is near the stishovite transition density. This trajectory also corresponds to the shock front for $t > -1$ ns. Velocities for each trajectory are also shown. Solid curves, 7380; dotted curves, 7381; dot-dashed curves, 7382.

CHAPTER 5

COMPARISON OF EXPERIMENTAL RESULTS WITH SIMULATIONS

5.1 Introduction

This chapter attempts to examine and interpret the simulation results and the experimental results. Shock trajectory data is presented for a large number of shots. In addition a detailed comparison of experiment and simulation among several individual shots is presented. The experimental results contained several features that were not predicted by the simulations. A detailed discussion and interpretation of these important differences is presented.

5.2 Trajectory measurements

5.2.1 Measurement details

The experimental measurements analyzed here consist of a set of 23 trajectories. These were recorded for laser intensities ranging from $10^{12} \leq \Phi_{60} \leq 5 \times 10^{13} \mathrm{W/cm^2}$. Table IV displays detailed quantitative data measured for each shot. Most of the data were streak shadowgrams taken in a single day. Some additional shots taken on a later day are also included.

The beam spot size, D_{spot}, varied with the amplifier flashlamp pumping voltage. The value for Φ_{60} indicates the nominal peak intensity. This value is calculated

Table IV. Summary of experimental data

Shot	D_{spot} (μm)	E_L (J)	τ_ℓ (ns)	Φ_{60} (W/cm^2)	D_f (km/s)	D_p (km/s)	P_Φ (GPa)	P_{D_f} (GPa)	τ_r (ns)
2-20	45	3.75	2.8	4.8×10^{13}	19	27	590	500	1.0
17-20	45	3.49	2.9	4.4	—	31	550	—	—
18-20	45	3.57	2.6	4.8	17	28	590	390	0.9
3-20	45	2.83	2.6	3.8	15	26	490	300	1.0
4-20	45	3.03	2.6	4.1	17	27	530	366	1.0
5-20	45	2.18	2.6	3.0	<18	27	410	<440	1.0
6-20	45	2.12	2.4	3.1	<18	28	420	<440	> 0.8
5-22	45	2.03	2.4	2.9	16	23	400	340	0.9
7-22	45	2.03	2.4	2.9	16	23	400	340	1.1
7-20	47	1.66	2.2	2.3	15	21	340	290	1.1
8-20	47	1.66	2.2	2.3	14	21	340	230	1.3
9-20	50	1.10	2.0	1.5	13	22	240	210	1.2
9-22	50	0.99	1.9	1.4	12	23	220	190	1.3
10-22	50	1.10	1.9	1.5	12	—	240	180	1.3
12-20	64	0.579	2.1	0.46	<10	19	96	<120	1.6
22-20	64	0.714	2.1	0.58	9.1	21	120	97	1.5
23-20	64	0.579	2.1	0.46	8.7	20	96	89	1.6
13-20	73	0.393	2.1	0.24	6.0	18	58	41	2.2
21-20	73	0.354	2.1	0.23	7.7	15	55	69	1.7
15-20	100	0.185	1.9	0.067	4.7	—	21	25	—
16-20	100	0.185	1.9	0.069	4.5	—	22	22	—
19-20	100	0.108	1.9	0.040	4.5	—	14	22	—
20-20	100	0.121	1.9	0.045	5.0	—	16	28	—

from E_L, D_{spot} and the digitized pulse shape (*cf.* Figure 3-8). The shock speeds, D_p and D_f, were extracted from most trajectories as described in §3.2.3; these are listed in the table. The pressure-intensity scaling law discussed in §4.3.3 was used to estimate the peak ablation pressure applied to the target, given Φ_{60} and are listed in the table under P_Φ. For this value the specific equation,

$$P_\Phi = 175\left(\Phi_{60}\right)^{7/9}$$

was used to obtain P_Φ; here P_Φ is in GPa units and Φ_{60} is in units of 10^{13} W/cm^2. This is the scaling law corresponding to the Mora–B model which fits the simulation results. The pressure, P_{D_f}, corresponding to the the asymptotic shock speed, D_f, was obtained from the principal Hugoniot generated from the SESAME 7380 EOS table. These pressures are listed in a column beside P_Φ for comparison. Finally, the approximate relaxation time for the shock speed decay from the peak value, D_p to the asymptotic value D_f is listed under the column τ_r. The data is grouped in order of decreasing intensity (laser pumping level) so that shots of similar irradiation conditions can be compared amongst each other and with appropriate simulations. It should be noted that due to shot-to-shot fluctuations associated with the high power laser beam the set of shots contained within each group are similar but not identical in irradiation conditions. In this case the comparisons among similar shots give an indication of the overall reproducibility of the laser-driven shock loading method.

Experimental uncertainties (error estimates) are not listed in the table, however, they are by no means negligible. In particular the values for Φ_{60} have uncertainties of roughly $\pm$ 25%. The largest contribution is a $\pm$ 10% uncertainty in D_{spot}, and a $\pm$ 5% uncertainty in E_L. Note that due to the scaling laws discussed in §4.3.3 the 25% uncertainty in Φ_{60} leads to a 20% uncertainty in P_Φ, and in turn a 10% uncertainty in the value of D based on the shock speed scaling. The values for

D extracted from the trajectory curve have typically $\pm$ 1 to $\pm$ 2 km/s uncertainties, owing mainly to the difficulty of taking a derivative (the slope) of a curve which is noisy to start with. The errors in τ_r are around $10-25\%$. Furthermore, it should be noted that the crude method for extracting these relaxation times precludes making much more of them beyond an order of magnitude estimate. These uncertainties can probably be improved significantly with improved facilities (particularly the laser) and changes in some details of the measurement (such as a shorter probe beam wavelength, more probe beam intensity, and a better streak camera readout).

Simulations were performed for a set of representative shots in the data set and will be discussed in detail below. All the simulations were performed with the "standard" calculation as described in chapter 4, incorporating inverse bremsstrahlung absorption, Spitzer heat conduction and the SESAME table 7380 EOS in the single temperature form. The laser pulse was taken directly from the digitized photodiode signal as input to the code. Since the pulses were always slightly asymmetric, the centroid of the pulse was used as the time zero reference in the calculations. The calculation for the centroid used only the region of the pulse which exceeded 10% of the peak intensity. In the analysis of the experimental trajectories a similar averaging method was used to determine the centre of the streak camera fiducial signal. In general the centroid differed from the peak by no more than 200 ps and often much less.

5.2.2 General features

A set of trajectories selected to be representative of the range of intensities are displayed in Figure 5-1. Simulations were performed for the same shots and the predicted trajectories are shown in Figure 5-2.

A number of basic features common to nearly all of the measured trajectories are evident in Figure 5-1. Very clear in the figure is the prominent two-wave structure for all but the lowest intensity. As noted in the discussion of §3.2.2 the

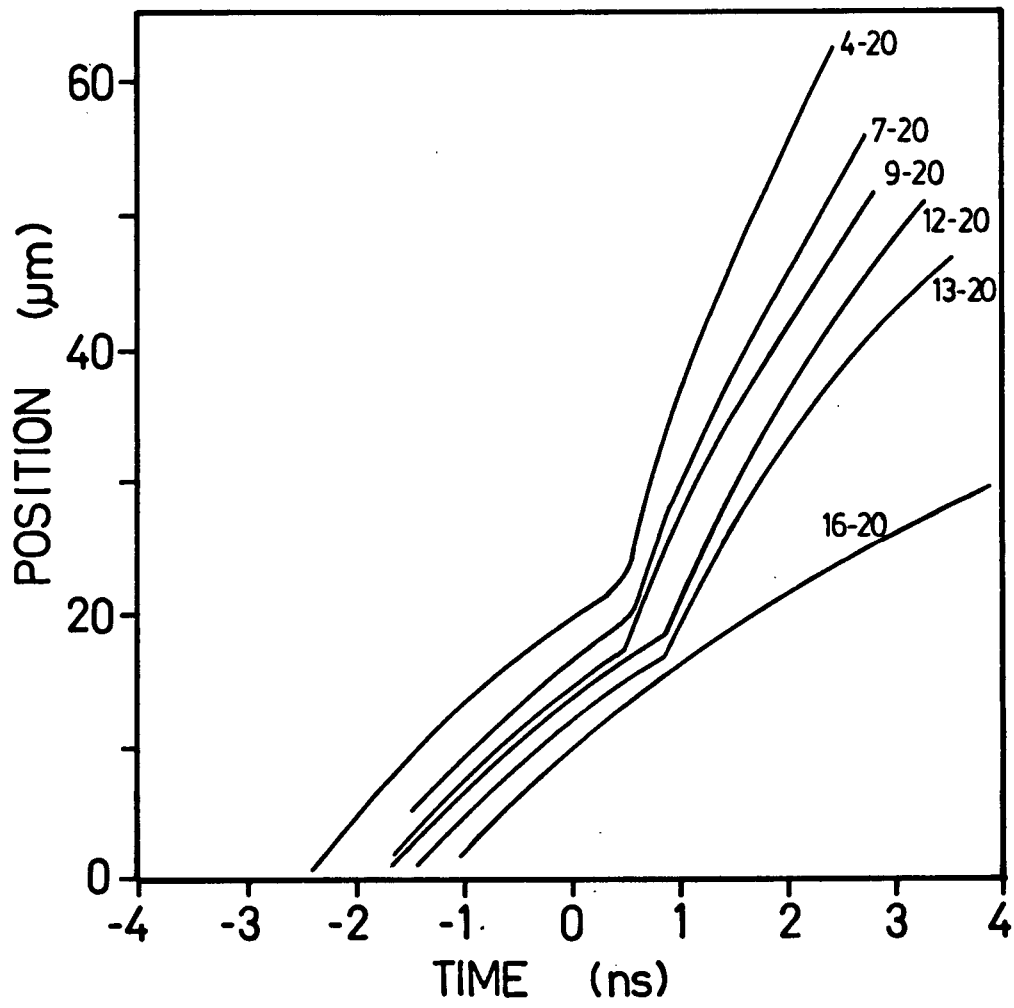

Figure 5-1 Measured trajectories spanning the range of laser intensities sampled in the experiment. Each curve is identified by a shot number.

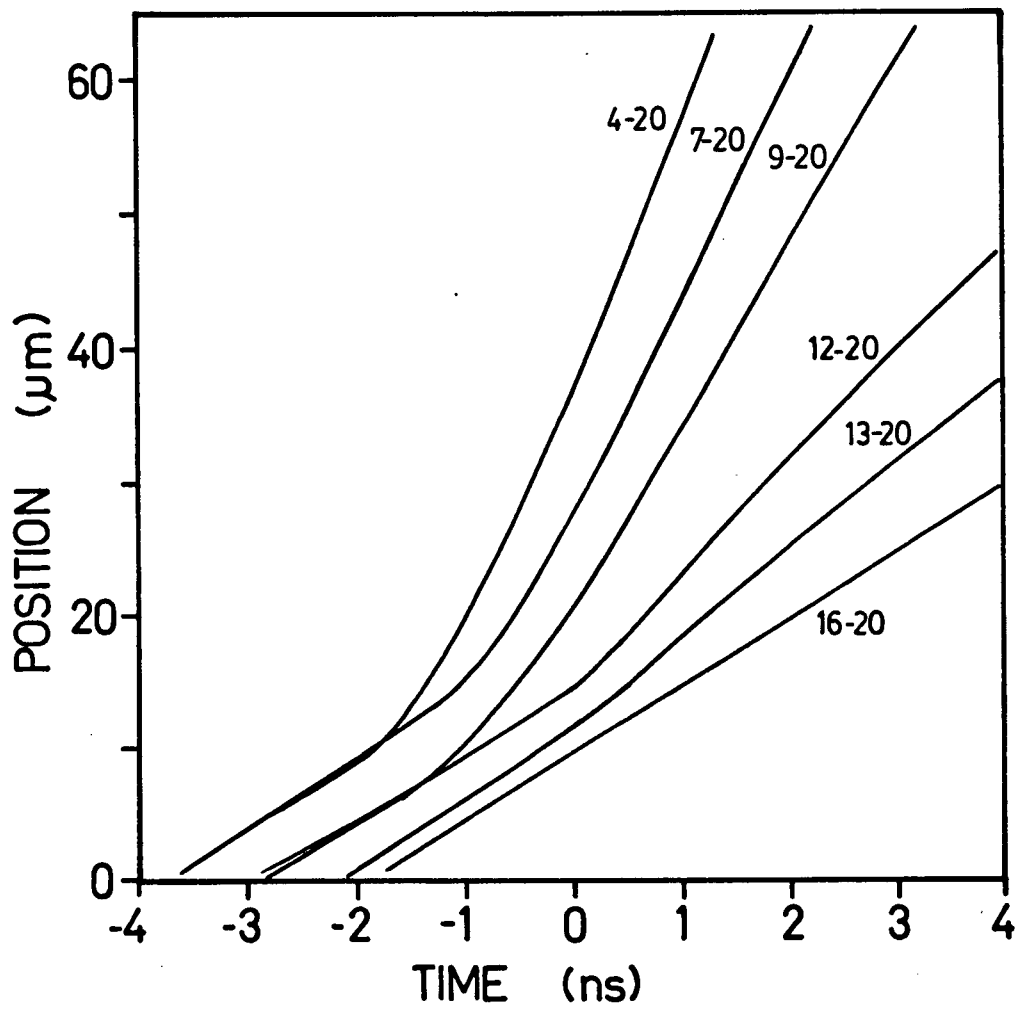

Figure 5-2 Simulated trajectories corresponding to the set of shots displayed in Figure 5-1. The curves show the trajectories of the leading front of the pressure wave, on the $\rho = 2.3$ g/cm^3 contour. Each curve is identified by a shot number identifying the shot for which the simulation was performed.

initial segment may not represent the true (high pressure) shock front, while the later segment does. From the measurements it appears that the high pressure shock front is not evident until it emerges at a depth of around 15 - 20 μm in the target. At that point it also attains a maximum speed transiently, which then decreases to a nearly constant value on a time scale of 1 - 2 ns.

The two-wave structure is present in the simulations, although the details are different. Here the low density elastic wave is shown to propagate ahead of the main shock for the early stages of the pulse. However, the transition where the high pressure front overtakes the elastic wave is evidently very smooth in the simulations. The choice of the $\rho = 2.3$ g/cm^3 contour to represent the leading front is arbitrary to some degree.† This contour shows the position of the leading front of the pressure wave when it is an elastic wave at low pressures, and when it is a strong shock at high pressures after the high pressure wave has overtaken the elastic front. However, because this density is reached at low stresses (a few GPa) this contour is quite sensitive to the rising edge (gaussian wing) of the laser pulse. For all the shots at intensities $> 10^{13}$ W/cm^2 (4-20, 7-20 and 9-20) the high pressure shock is well developed at least 1 ns before the peak of the pulse and is clearly overtaking the elastic wave. Furthermore, there is no transient "overshoot" in the shock speed. This contrasts with the experiment which shows the formation of the high pressure shock much later in the pulse, even for the high intensity shots.

Further information from the experiment is obtained by examining the trajectory speeds. Shown in Figure 5-3 are the two speeds, D_p and D_f, derived from the measured trajectories and plotted as a function of laser intensity. The lower set of values, with error bars, correspond to D_f, which is the asymptotic or late

† For low pressures (near the HEL at $\sim$ 10 GPa) the elastic wave front is not very sharp due to the anomalous elastic precursor unique to fused silica[52,60] (*cf.* §2.4). This behaviour is reproduced in the simulations because the compressibility anomaly[61] which causes it is represented in the SESAME EOS table 7380.

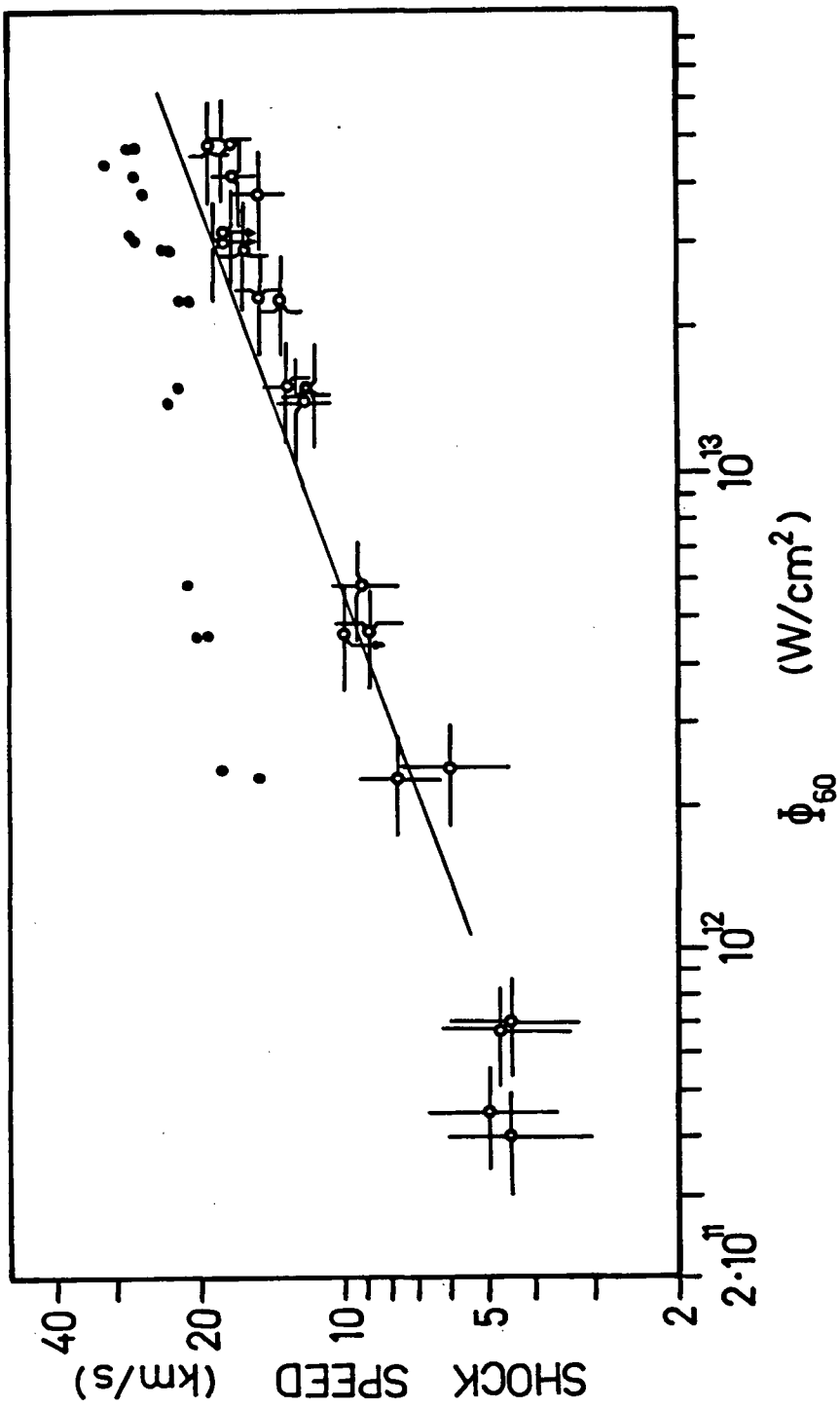

Figure 5-3 Trajectory speeds as a function of laser intensity. Open symbols with error bars represent the asymptotic speeds, D_f; solid symbols represent the peak speeds, D_p. The solid curve is the shock speed versus intensity scaling predicted by the simulations as descibed in §4.4.3.

time trajectory speed. At late times the trajectories appeared to be approaching nearly steady (or slowly decaying) shock states, so D_f is representative of the characteristic pressure reached in the experiment. The solid curve shown in Figure 5-3 represents the shock speed versus intensity scaling (*cf.* §4.4.3) for comparison with the experimental results. The upper set of data points (solid symbols) represent the measurements of D_p, which is the peak transient speed measured at the moment the stong shock appeared to emerge as the leading front. No error bars are indicated on the graph, however the uncertainties are similar in absolute magnitude to those indicated for the D_f values. It is remarkable that the peak values ranged from 40% to 100% larger in magnitude than the asymptotic speed, and lie consistently above the shock speed versus intensity scaling curve (solid line) derived from the simulations. For the lowest intensity shots, no transient was observed and only the asymptotic speed is shown.

The experimental results for D_f appear to fit the expected shock speeds fairly well. The higher intensity shots tend to have slightly lower speeds than predicted by the scaling. (Similarly $P_{D_f} < P_\Phi$ in this intensity range.) This might be expected for two reasons. Firstly, the values for D_f were extracted at times late in the laser pulse, when the ablation pressure has dropped considerably. In contrast, the scaling law curve was obtained using the maximum shock speeds attained near the peak of the laser pulse in the simulations. Secondly, the late time shock speeds were obtained at times when the shock has propagated to large depths in the target, and the motion is beginning to become two-dimensional (expanding), which tends to reduce its speed below the value expected for planar motion. This discrepancy is not far beyond the bounds of the error bars; one may conclude that the pressures expected from the P_Φ scaling are in fact being generated in the target.

The peak transient speeds extracted from the trajectories appear to have a systematic scaling with laser intensity, roughly $D_p \sim \Phi^{0.25}$. This is not consistent with the shock Hugoniot scaling of $D \sim \Phi^{0.38}$. These speeds are remarkable because

of their very large magnitude, and the fact that they are highly transient. The very large magnitudes are not consistent with Hugoniot states expected from the pressures thought to be generated in the target. For example in the worst case a peak transient speed of $\sim$ 16 km/s was obtained at $\Phi_{60} \sim 2.5 \times 10^{12}$ W/cm^2 ($P_\Phi \sim 60$ GPa), while a steady shock propagating at this speed would require a pressure $>$ 300 GPa ($\Phi_{60} \sim 3 \times 10^{13}$ W/cm^2). Even the large uncertainties associated with the measurements cannot account for this. Therefore it appears quite likely that these transients are a real effect which cannot be accounted for by shock states on the principal Hugoniot.

5.3 Comparison of results

For most laser intensities at least two or more shots were taken so that they can be compared to assess the reproducibility of the measurements. The trajectories can be grouped according to the laser amplifier pumping level, which tends to give similar (but not identical) conditions from shot to shot. These groups of reduced trajectories are displayed in Figures 5-4 and 5-5, along with the results of a simulation representative of the shots within each group. In these figures the measured trajectories are represented by the dashed curves and labelled with the shot number; a representative error bar is shown to indicate the relative uncertainty in placing the measured curve on the origin of the plot. The simulation results are represented by the solid and dotted curves. The solid curve corresponds to the $\rho = 2.3$ g/cm^3 density contour which is the leading front of the elastic wave. The dotted curve shows the $\rho = 4.0$ g/cm^3 density contour which identifies the stishovite transition.

Examination of the trajectory data in comparison with the simulations shows a systematic trend as a function of laser intensity. The data can be separated into two groups: low intensity $< 10^{13}$ W/cm^2, Figure 5-4; and, high intensity $> 10^{13}$ W/cm^2, Figure 5-5.

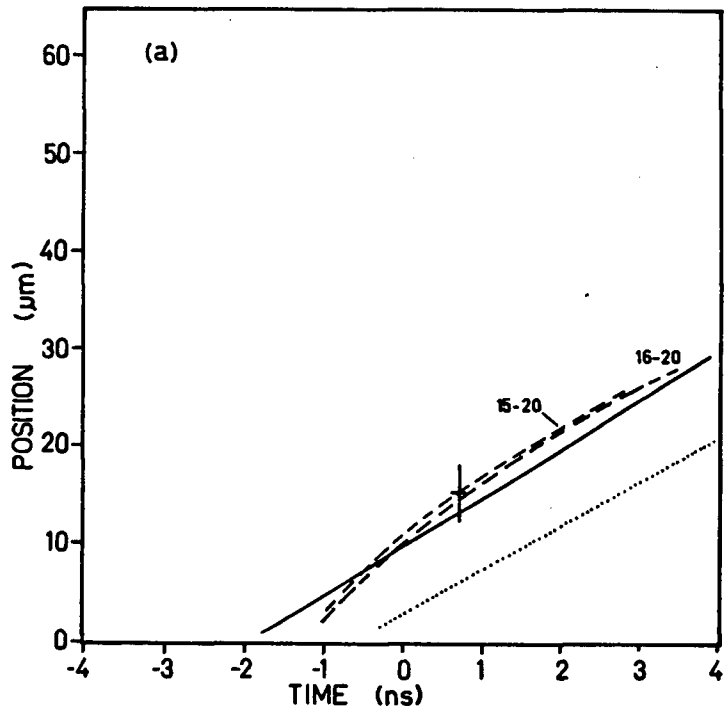

Figure 5-4 Measurements and simulations of low intensity shots. Dashed curves are measured trajectories. Solid curve and dotted curves are from simulations. Solid curves represent the $\rho = 2.3$ g/cm^3 density contours; dotted curves represent the $\rho = 4.0$ g/cm^3 density contours.

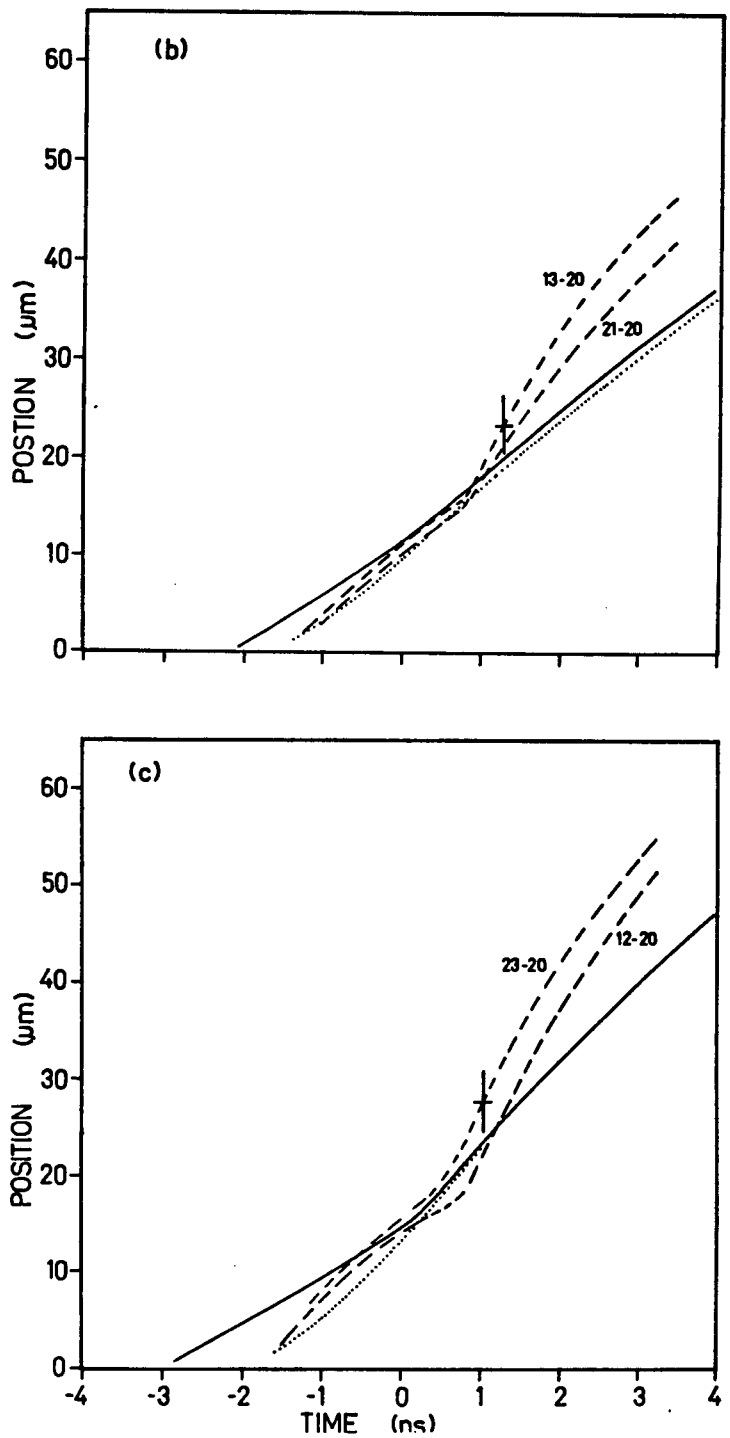

Figure 5-4 (continued).

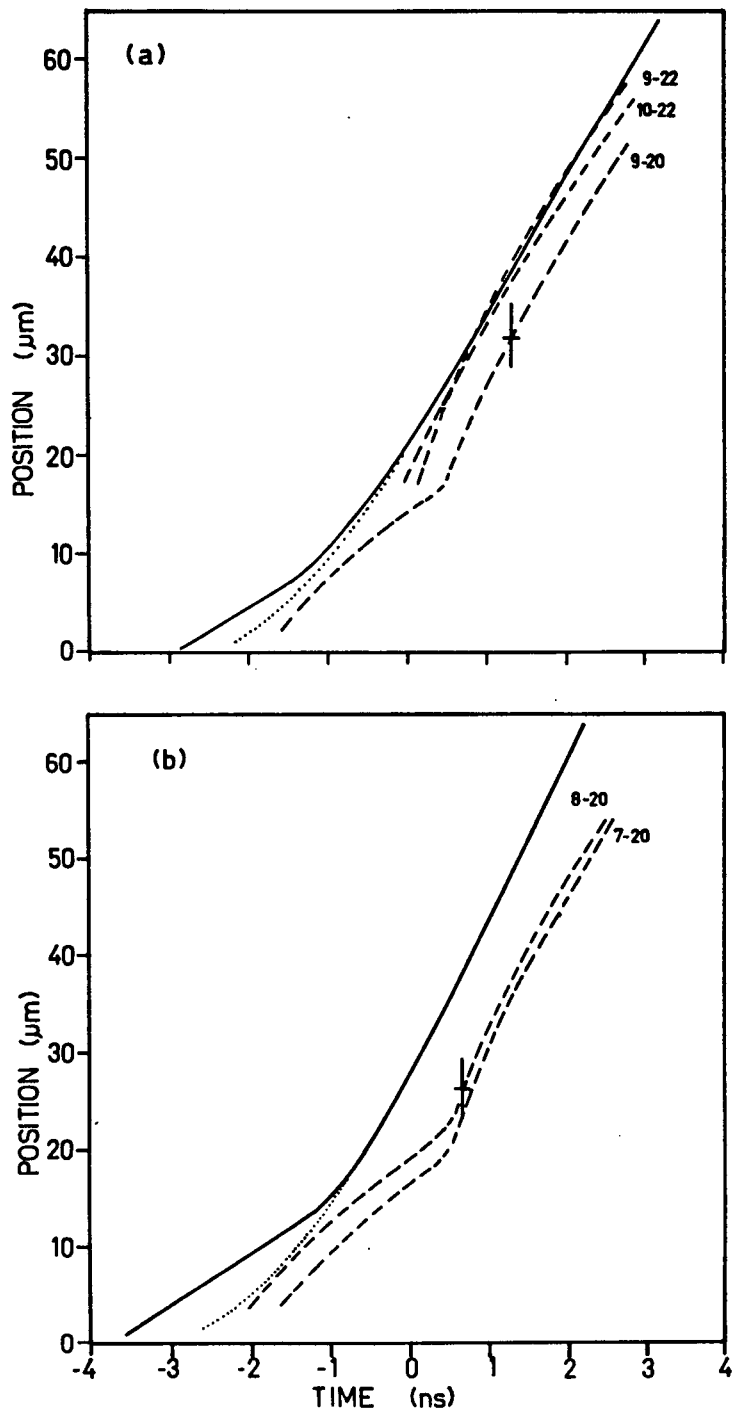

Figure 5-5 Measurements and simulations of high intensity shots. Dashed curves are measured trajectories. Solid curve and dotted curves are from simulations. Solid curves represent the $\rho = 2.3$ g/cm^3 density contours; dotted curves represent the $\rho = 4.0$ g/cm^3 density contours.

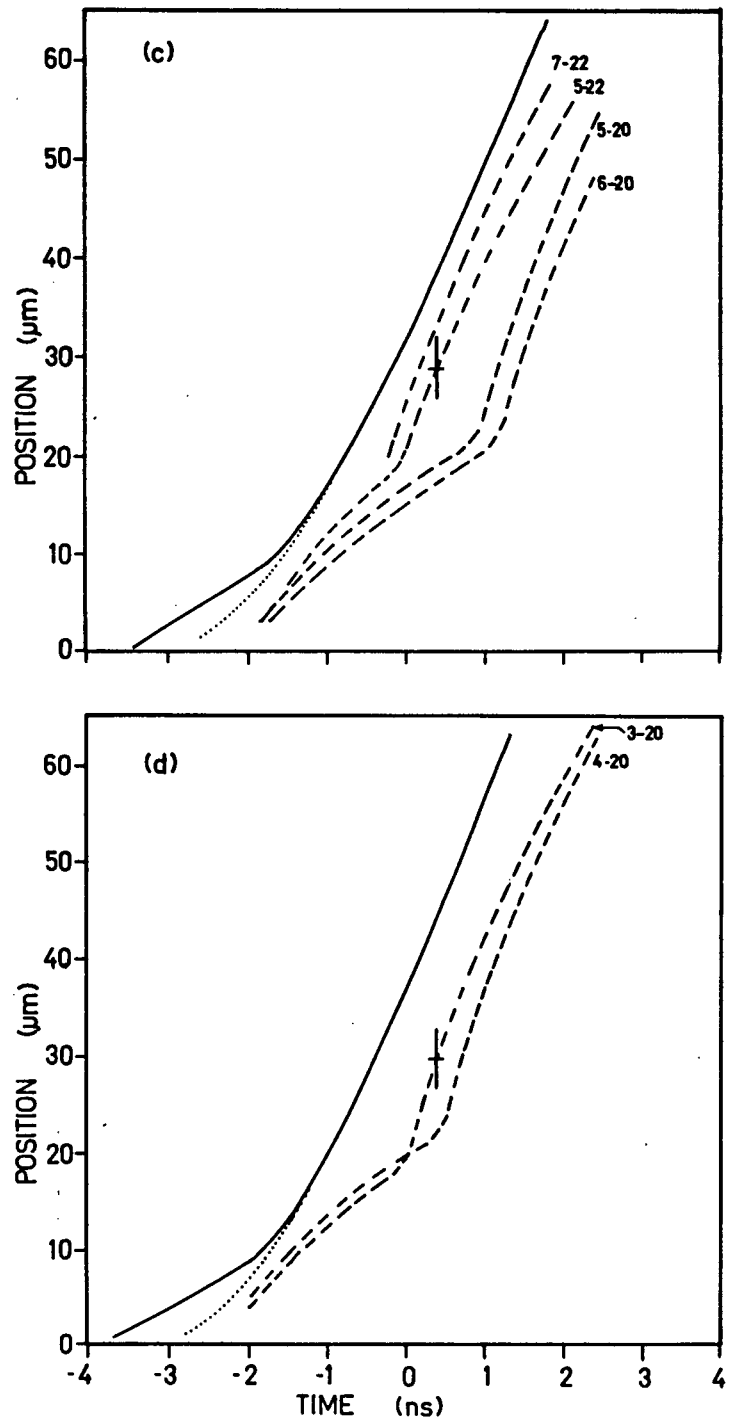

Figure 5-5 (continued).

At the lowest intensities (shots 15-20, 16-20)† the trajectories did not show the two-wave structure. The pressures expected for this range of intensities (on the basis of the P_Φ scaling) are near or below the stishovite transition pressure, so that these trajectories correspond to the low pressure elastic wave, which propagates at close to the sound speed. Comparison of the data with the simulation (Figure 5-4a) shows very good agreement with the elastic front. The simulations predict that a slower second wave is produced, but this does not form until late in the pulse, and it does not catch up to the elastic wave front. In reference to the discussion of elastic-plastic flow in §2.2.2, this situation corresponds roughly to a shock pressure in the range $P > P_{hel}$, but not large enough to form a single step.

For intensities in the range $> 2 \times 10^{12}$ W/cm^2 all the trajectories display the two-wave structure. Similarly, all the corresponding simulations show the high pressure stishovite wave (second wave) catching up to the elastic wave as the driving pressure increases, eventually to overtake the elastic wave. The "low intensity" shots of Figure 5-4b and Figure 5-4c were separated from the "high intensity" shots of Figure 5-5 because the comparison of experiment and simulation for the former cases differs from the latter in two aspects. Firstly, the high pressure wave as measured from the experimental trajectories appears to emerge as the leading front at roughly the same point on the x-t diagram as the coalescence of the high pressure and elastic waves in the calculated trajectories. Secondly, the measured trajectories reach a large transient speed at the moment the high pressure front is formed, and because of this, the measured trajectories appear to penetrate much *deeper* into the target than is predicted by the simulation. The trajectory speed decays very quickly to a value closer in agreement with that expected for a steady shock at the expected pressure. To summarize, as the driving pressure is increased significantly beyond the stishovite transition pressure a two-wave structure appears in the trajectories.

† Shots 19-20 and 20-20, taken with the lowest intensity, had nearly identical trajectories (not shown) as shots 15-20 and 16-20.

In addition, during the initial stages after formation of the high pressure shock, the propagation is non-steady.

As noted above, the higher pressure shots of Figure 5-5 differ from the lower pressure shots. The former retain the prominent two-wave structure as well as the non-steady propagation of the high pressure front. However, in these shots the high pressure wave emerges late compared to the coalescence of the high pressure and elastic waves predicted from the simulations. Furthermore, all the trajectories seem to lag *behind* those predicted by the simulations. In contrast with this disagreement, the asymptotic shock speeds attained at late times do approach the values expected from the P_Φ scaling, i.e. the final shock speeds predicted by the simulations are in agreement with the experiment, even though the trajectories are quite different.

Reproducibility at the higher intensities is also less consistent. The high pressure shock emerges later in shot 9-20 (Figure 5-5a) than in shots 9-22 and 10-22 (taken on a different day), at conditions which were nominally quite similar. This could be due to slight differences in the laser pulse shape, or the spot distribution (which was known to occur on a day to day basis). A similar difference is noted between the pairs 6-20, 5-20 and 7-22, 5-22 (Figure 5-5c). Shots taken on the same day under similar conditions appear to be quite reproducible eg. 3-20,4-20; 7-20,8-20; 5-22,7-22; 9-22,10-22; as well as several pairs displayed in Figure 5-4. Despite these fluctuations all the high intensity trajectories appear to show the high pressure shock front emerging clearly behind the trajectories predicted from the simulations.

5.4 Discussion

The rather obvious disagreement between experiment and simulation makes interpretation of the results difficult and in some respects uncertain. A short description of the basic interpretation of the results is presented first. Further elaboration on this basic interpretation will follow.

The agreement of the late time trajectory speeds, D_f, with the expected shock speed scaling leads to the conclusion that the pressures expected for the laser intensities are indeed reached, and that the measured trajectories do represent a shock front formed by the pressure induced by the laser ablation process. A two-wave structure was observed for all shots with intensity $> 2 \times 10^{12}$ W/cm^2, while a single wave was observed at lower intensities. This is qualitatively consistent with the behaviour expected due to the stishovite transformation in fused silica (*cf.* §4.4.2) and it suggests that the prominent two-wave structure is somehow connected with the stishovite phase transformation. The high pressure shock front was observed to be non-steady, indicating that a relaxation process, such as would be involved in a phase transformation, was occurring in the material behind the observable front. The very high initial speed followed by a rapid decay implies that the density behind the initially formed front is less than the Hugoniot density. The material subsequently relaxes to the Hugoniot state on a time scale of $\sim$ 1 ns.

The anomalous delay in the formation of the strong shock as compared with the simulation results presents a far more difficult problem. There are two possible explanations. The most interesting one is that the material undergoes another phase transition with an associated volume collapse, thus reaching significantly higher densities beyond the stishovite density. If such a volume collapse occurred, the high pressure wave would be slowed down in propagating through this layer and would not emerge until later times than predicted by the simulations, thus leading to the observed delay. (When the high pressure front overtakes the elastic wave, it forms the strong shock which compresses the unperturbed material to the stishovite density, and eventually propagates on the known Hugoniot.) Furthermore, such a transition occurs only above a characteristic pressure, so that the delay effect is not observed for lower pressures: this is also consistent with the experimental observations.

Alternatively one might attribute the anomalous delay to a combination of various uncertainties which arise due to effects not taken into account in the data analysis and the simulations so far. These effects include primarily the obvious transient relaxation phenomena identified above as well as two-dimensional motion.

5.4.1 The high speed transient

Non-steady propagation of the high pressure shock, as observed in the measurements, can be understood within the picture presented in chapter 2 discussing phase transitions. A schematic diagram of the dynamic material states obtained in a non-steady wave is shown in Figure 5-6. The solid curve in the figure represents the equilibrium Hugoniot curve for a material which undergoes transformation, above a characteristic pressure, P_t, to the final state. Also indicated is a dashed curve which extapolates the low pressure stress-volume response to pressures above the characteristic transition. Such a curve might represent an elastic compression curve, or perhaps the Hugoniot of the low pressure phase extrapolated into the high pressure regime where this phase is unstable or metastable under thermodynamic and hydrostatic equilibrium conditions. One assumes that there is a characteristic relaxation time, τ_t, associated with the transformation process which determines the rate at which the material can transform to the equilibrium phase from the unstable or metastable phase under non-equilibrium conditions. We wish to examine the wave propagation induced by a sharp jump in pressure applied to the material at a well-defined instant in time. If one observes the initial stages of shock propagation on a time scale small compared to the transformation time, τ_t, then one observes a shocked state appropriate to the dashed curve in Figure 5-6. The main point is that, on an instantaneous or very short time scale, the material responds to the applied stress by reaching an unstable (non-equilibrium) stress-volume state of lower compression than the final state. The transformation is then completed on

a time scale governed by the microscopic processes that effect the transformation to the stable phase or state.

Two cases (a) and (b) are illustrated in Figure 5-6 which show how this kind of material response results in a decaying (non-steady) shock. If the characteristic transformation time is τ_t we can consider the two asymptotic extremes of time t measured from the initial formation of the wave. In case (a), corresponding to time $t \ll \tau_t$, the shocked state lies on the metastable extrapolation of the Hugoniot for the initial phase. This is because for these short times none of the shocked material has sufficient time to undergo significant tranformation to the final state on the Hugoniot. The Rayleigh line corresponding to this metastable state is steeper than that for the Hugoniot, so that the wave propagates at a speed *greater* than the speed given by the Hugoniot. In the other extreme, for times $t \gg \tau_t$, as represented by case (b), the shock has propagated long enough for most of the material to reach the equilibrium Hugoniot state. Therfore, the shock propagates as a steady wave with constant speed, D. A thin layer at the wave front, of thickness $d \sim D\tau_t$, is not in equilibrium because of the finite transformation rate. The Rayleigh line for the standard Hugoniot state is shown in the figure, and one may note that this line passes through the metastable Hugoniot at the point labelled 'f'. The corresponding steady wave profile is also indicated. The state corresponding to 'f' is obtained at the leading front, while subsequent compression to the final state occurs behind this leading front, on a time scale τ_t.

For the intermediate case where time $t \sim \tau_t$ the layers of material that were initially shocked have had enough time to complete much of the transformation to the final state; layers closer to the shock front have had less time, however, and do not reach these densities. The wave front also decelerates noticeably because of the relaxation taking place in the shocked material which sends a release wave that overtakes the shock front and reduces the stress level at the front. This intermediate

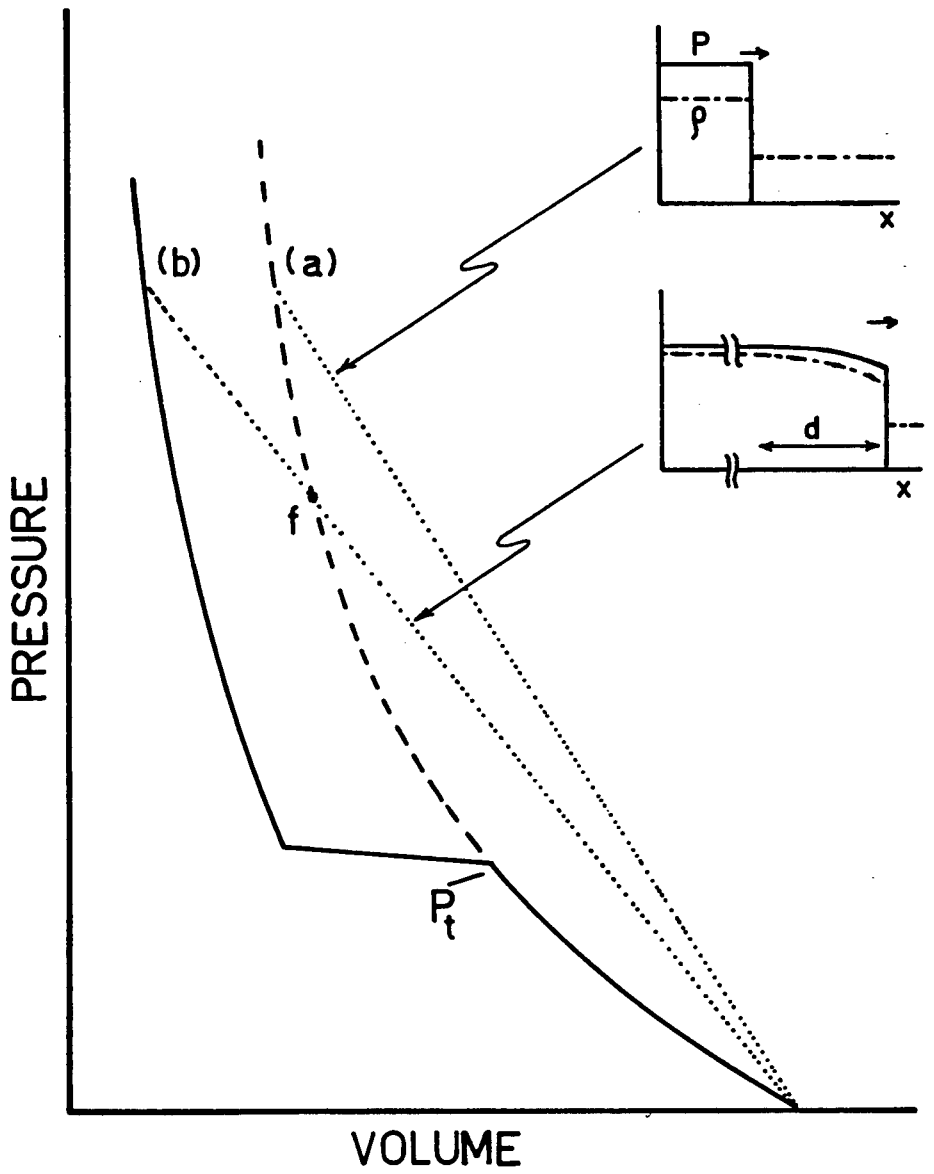

Figure 5-6 Schematic diagram of dynamic states reached in a non-steady shock front. The solid curve is the equilibrium Hugoniot; the dashed curve is the metastable (or unstable) Hugoniot extension from the initial state; the dotted curves are Rayleigh lines.

period represents the non-steady regime and the Rayleigh line construction cannot be used to describe it.

This basic picture has been presented before and in fact represents qualitatively some of the features predicted by the models utilized by Hayes[33,34] and Andrews[32] to describe shock induced phase transformations (*cf.* §2.2.4). Experimental measurements such as the stress relaxation in elastic shocks in α-quartz reported by Ahrens and Duvall[70] also display features similar to the description above. Similarly the dependence of the HEL on propagation distance in borosilcate glass, observed by Cagnoux[71], represents a non-steady shock front which is decaying due to stress relaxation processes behind the shock front. However, in the latter measurements the observed stress relaxation was measured at much lower stresses ($<$ 20 GPa) with much larger samples (mm size), and longer time scales (several μs). The microscopic processes taking place are also probably very different.

The non-equilibrium state at the non-steady shock front can be roughly calculated from the shock speed measurements if we use the simulations to estimate the pressure. The shock speed - pressure pair, (D_p,P_Φ), represents a "Hugoniot" point (the pressure is only inferred indirectly from the simulations) which can be displayed in comparison with the equilibrium Hugoniot. The assumption implied by this representation of the data is that the D_p values represent a measurement in the regime $t \ll \tau_t$; therefore the resulting "Hugoniot" represents the unstable branch corresponding to the dashed curve in Figure 5-6. A plot of the non-equilibrium "Hugoniot" points is shown in Figure 5-7 along with SESAME Hugoniots (tables 7380 and 7381) for comparison. Due to the large uncertainties in P_Φ the error bars on these plots are quite large. Nevertheless, the data which is shown in comparison with the equilibrium Hugoniot curve is clearly distinct from the equilibrium Hugoniot.

The relaxation time, τ_r, is shown in Figure 5-8, plotted as a function of laser intensity. Evidently τ_r ranges from about 2 ns at 2×10^{12} W/cm^2 to $<$ 1 ns at 5×10^{13}

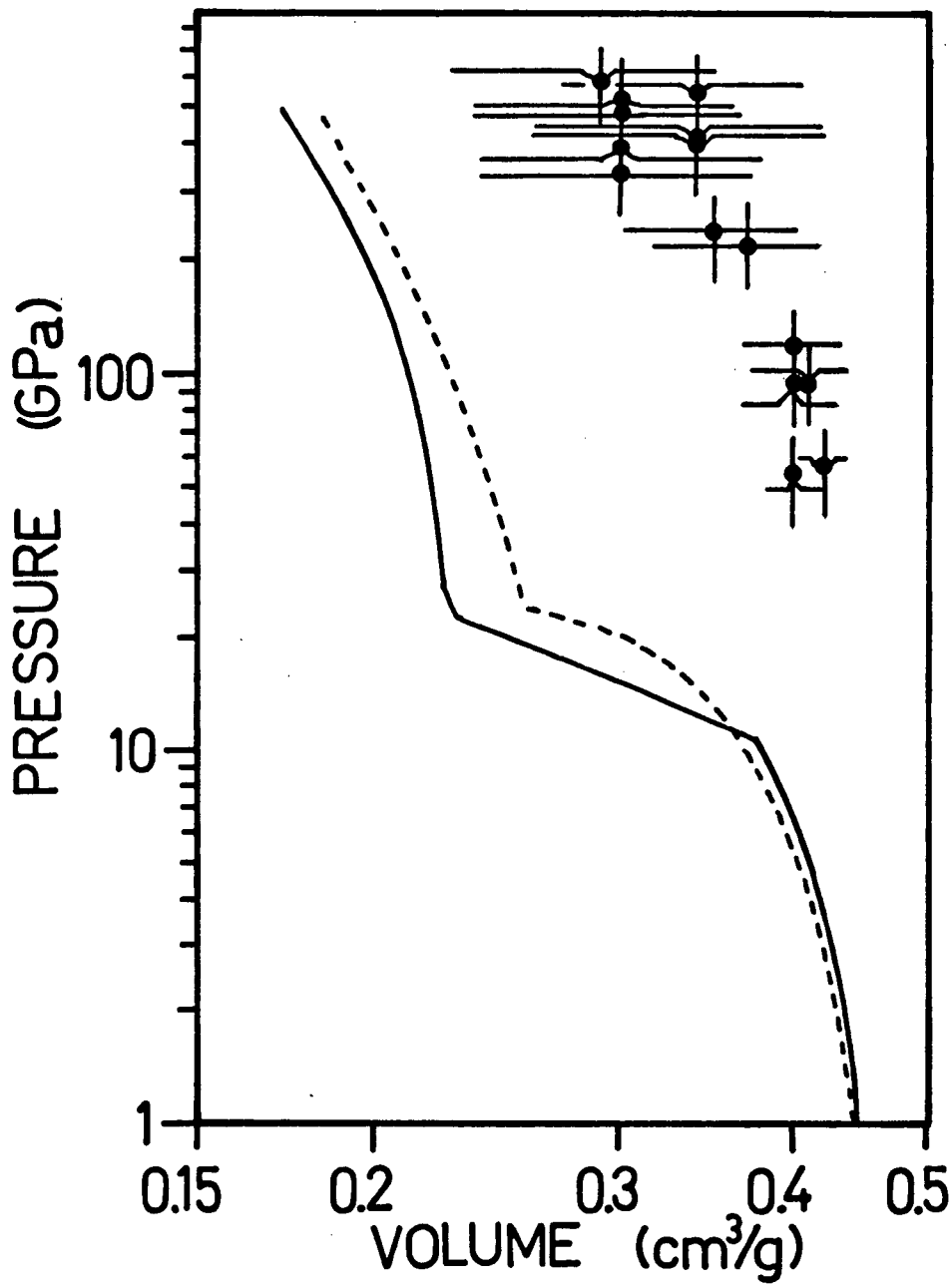

Figure 5-7a Non-equilibrium dynamic states reached in the non-steady shock front, on the $p-V$ plane. Equilibrium Hugoniots calculated from the SESAME 7380 (solid curve) and SESAME 7381 (dashed curve) EOS tables are shown for comparison.

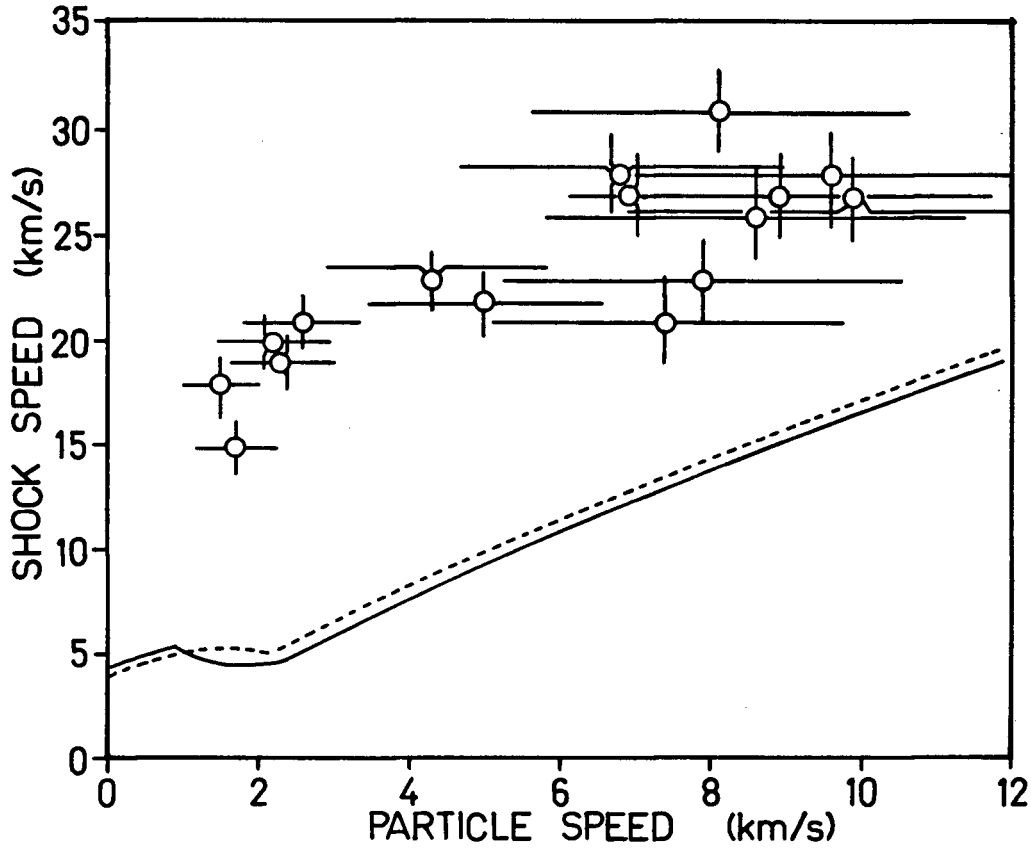

Figure 5-7b Non-equilibrium dynamic states reached in the non-steady shock front, on the $D-u$ plane. Equilibrium Hugoniots calculated from the SESAME 7380 (solid curve) and SESAME 7381 (dashed curve) EOS tables are shown for comparison.

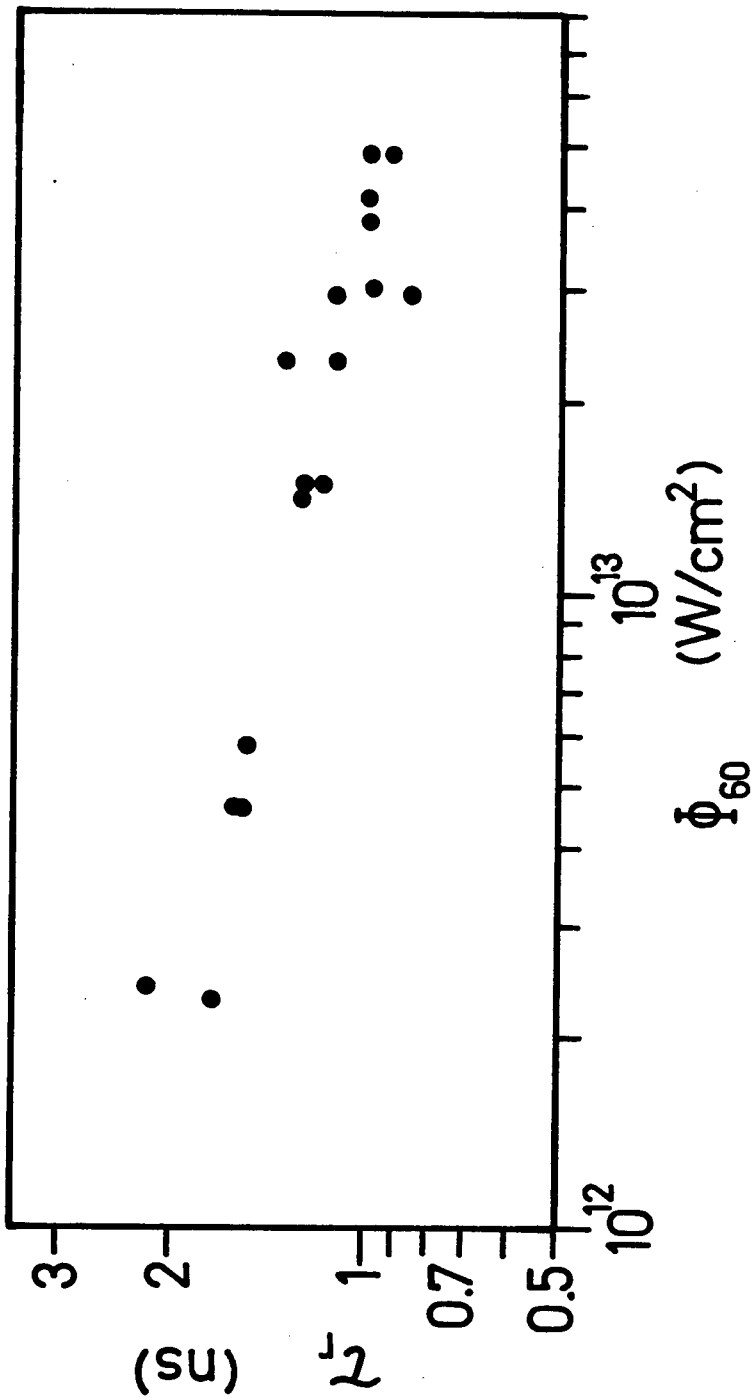

Figure 5-8 Relaxation time, τ_r, in the non-steady shock front.

W/cm^2. This data suggests a relatively weak scaling with intensity, $\tau_r \sim \Phi^{-0.2}$. The values for τ_r ranging from 2 - 1 ns combined with the (asymptotic) shock speeds ranging from 7 - 19 km/s implies an effective relaxation distance $d_r \sim D\tau_r$ of approximately 15 μm.

The data presented in Figures 5-7 and 5-8 implies non-equilibrium states that are remarkably far from the equilibrium Hugoniot. The time and space scales over which these non-equilibrium states persist are also not particularly small. Wallace's calculations for aluminum[26,27] predict shock rise times around 10^{-12} s at similar pressures.† Aluminum is structurally much simpler than silica, and does not undergo any known pressure-induced phase transitions (aside from melting). It is interesting to see that the complex phase transformations in silica can lengthen the equilibration time behind the shock by up to three orders of magnitude as compared with the calculation for aluminum.

One of the main assumptions in this interpretation is that the high pressure shock somehow forms suddenly – in this case at a depth of around 20 μm in the target. It is not clear why this should be so, although the reason might be related to the non-equilibrium properties suggested above. In the simulations the smoothly rising gaussian pressure pulse generates a smoothly accelerating shock front in which the compression to stishovite densities is clearly visible at early time in the laser pulse (for the high intensity pulses). Such a smoothly accelerating shock is clearly not observed in the experiment. The rise time of the pressure pulse is comparable to the relaxation time τ_r inferred from the data, which implies that the shock formation process throughout most of the laser pulse could be dominated by non-equilibrium relaxation effects. Because of these complications it is not appropriate to regard the value of τ_r as being more than an order of magnitude estimate of the characteristic relaxation time of the shocked material.

† Direct measurements on these time scales are not yet possible.

These facts provoke a large number of questions regarding the microscopic dynamics of the compression process. For example in reference to Cagnoux' observations of a stress dependent HEL in borosilicate glasses[70], one might ask if the effective HEL is substantially increased compared to the nominal value for the short duration of the applied stress created with the laser pulse? Is the abrupt formation of the high pressure shock an elastic yield process? If so, what is the magnitude of the stress deviator? Does the material in the 15-20 μm layer near the surface of the target deform homogeneously or inhomogeneously as suggested by Grady's shear banding theory? If it yields inhomogeneously, what is the characteristic dimension of the shear bands? It is interesting to note that elastic-plastic flow theory, and measurements, give a risetime of $\sim 10^{-8}$ s at 18 GPa[29,30] for fused silica, and a scaling of strain rate with the 4$^{\text{th}}$ power of the Hugoniot stress (i.e. $\tau \sim p^{-4}$). This can be extrapolated to be $\sim 10^{-11}$ s at 100 GPa, which is somewhat smaller than the magnitude of τ_r. The scaling of τ_r is not consistent with the inverse 4$^{\text{th}}$ power stress dependence as $\tau_r \sim \Phi^{-0.2}$ and $p \sim \Phi^{7/9}$ would imply that $\tau_r \sim p^{-0.26}$. This is not surprising as the stress range in the experiment is much higher than the range which is usually addressed in elastic-plastic flow models; moreover, elastic-plastic flow is usually addressed within the context of a two-wave system at stresses where the plastic wave remains behind the elastic precursor. It is also interesting to note that the pressures obtained in the experiment are close to, or larger than the Hugoniot melting transition pressure for fused silica. Lyzenga *et al.*[50] believe that the melt transition requires around 1 ns to take place (comparable to τ_r). However, the interpretation there was that the material reached stishovite density at the shock front and remained in a superheated solid state until the melt transition was nearly complete (the solid and liquid densities are nearly equal). The very high transient speeds measured here imply that the density at the shock front is not close to the stishovite density, but significantly lower, and that the relaxation process involves a significant amount of compression. The problem as it is presented in the context of

these results appears to be a complex time-dependent non-equilibrium process, and probably cannot be unravelled without more detailed information that can only be obtained from experiments designed specifically to investigate such processes.

For whatever reasons the abrupt formation of a high pressure non-steady shock front in fused silica appears to be a universal process in the experiment. The underlying reason for this seems to be that the time scale on which the pressure is applied, and the response is measured, is approaching that of a characteristic relaxation mode in the material. This fact points to a number of interesting questions and possibilities for laser-driven shock investigations of transparent materials. Besides the capability for extreme pressures, laser-driven shock loading provides opportunities for investigations on sub-nanosecond time and micron space scales. These microscopic scales are unique to the laser-driven shock loading method, and are very difficult to achieve with other shock loading methods. Surprisingly these scales appear to be sufficient for displaying the non-equilibrium effects related to the transformations of fused silica under compression. It should be noted that the shock transition in simpler materials, such as Al, with no known phase transformations is expected to occur on picosecond and nanometer scales, which are still beyond the reasonable capabilities of modern instrumentation. Phase transformations are known to occur in many transparent solids other than SiO_2, and one may be able to study the non-equilibrium dynamics of the transformations in such materials using similar techniques.

5.4.2 Delay in the formation of the strong shock

As discussed above, the apparent transient phenomena discussed above already lead to a complicated picture of the shock formation process. The possibility of a further phase change in SiO_2 is an interesting speculation which may be an important result if it is true. The analysis that leads to this speculation is based on the assumption of planar one-dimensional hydrodynamic motion that is implicit in

the simulations as well as the measurement. However, two-dimensional motion may also play an important role. A discussion of two-dimensional effects is presented in the next section. It should be noted that the interpretation of a phase transformation also implies that such a transformation must proceed at a rate fast enough to be observable during the measurement time.

The fact that the anomalous delay suggests a volume collapse occurs in the 15 - 20 μm layer of material near the target surface can be understood as follows. The point of formation of the high pressure shock marks the point where the high pressure front eventually steepens into a discontinuity. Such a discontinuity does not appear to exist at earlier times (or shallower depths) in the target. Thus the pressure front induced by the ablation process does not propagate very quickly, and it does not steepen into a discontinuity. The propagation speed of any compression (or expansion) wave is closely related to the degree of compression. This is evident in the definition of the sound speed, $c_s^2 = -V^2 \frac{\partial P}{\partial V}$ and also of the shock speed (the Rayleigh line), $D^2 = -V_0^2 \frac{\Delta P}{\Delta V}$, in which there is an inverse relationship between D^2 and ΔV. Thus a slow propagation speed implies a large volume change. The experimental result implies that the material in the compressed layer between the surface and the point of formation of the strong shock is reaching anomalously high densities, beyond the stishovite density.

This interpretation is supported mainly by the isentropic compression experiments reported by Pavlovskii *et al.*[88]. Those measurements imply that a volume collapse occurs on the isentrope (not the Hugoniot) at a pressure of $\sim$ 125 GPa and densities of $\sim$ 10 g/cm^3 are reached. The results of our experiment appear to be in agreement with such observations. The 125 GPa transition pressure is consistent with the fact that the delay effect is observed for shots with intensity $> 1.4 \times 10^{13}$ W/cm^2 ($P_\Phi > 220$ GPa, Figure 5-5), but not for shots at intensities $< 5 \times 10^{12}$ W/cm^2 ($P_\Phi < 100$ GPa, Figure 5-4). (No shots were taken at intermediate intensities.) In addition, Pavlovskii *et al.* emphasize the need for isentropic compression

to reach the high density phase. The simulation results presented in chapter 4 show that such a compression process may indeed occur with the gaussian laser pulse. In particular, the results presented in Figure 4-11 show that the isentropically compressed material follows a nearly constant temperature compression path, which is more likely to intercept a phase boundary at low temperatures (and high pressures) than the principal Hugoniot. However, the postulated new phase is not represented in the current EOS so that the compression process presented in the simulation results cannot represent the experimental situation exactly. This is because a strong shock is seen to form at early times in the simulations, in disagreement with the experimental results. Thus the experimental measurements suggest that as much as the first 20 μm of the target could be undergoing the anomalous compression, while a layer of only 10 - 15 μm thick is not strongly shocked according to the simulation results. Radiation preheat can affect the target to a depth of $\sim$ 8 μm, and should also be taken into account when considering the isentropic compression process.

As noted in §2.6 the isentropic compression results of Pavlovskii *et al.* have never been verified, and there is significant theoretical and experimental evidence against the existence of the postulated new phase. A rather obvious difficulty arises relating to the role of the non-equilibrium transformations, inferred above, in the dynamics of this volume collapse. For example, how can it be that fused silica is a material which *resists compression* to equilibrium densities on a 1 - 2 ns time scale in a shock front; yet, on very similar time scales it undergoes *anomalously large compression* to a new phase, with densities above the Hugoniot values, owing mainly to a smooth application of the pressure? These questions cannot be answered without further experiments designed specifically to investigate the existence of the phase transition.

5.4.3 Two-dimensional effects

The fairly small focal spot size used in the experiment always leads to two-dimensional motion, both in the expanding plasma and in the propagating shock front. These effects require attention since they may alter the interpretation of the experiment. One can discuss the effects of two-dimensional motion in the expanding plasma and in the shock front separately, although they are in fact coupled through the ablation zone.

Firstly, the hot expanding plasma created along the surface of the target rapidly expands to sizes much larger than the laser spot size. The expansion thus becomes spherical. Consequently the laser absorption region is removed further away from the ablation surface, and expands to an areal size larger than the nominal laser spot size. This has the effect of distributing the absorbed laser energy over a larger surface (and plasma volume) than would be inferred by the nominal spot size. The intensity, Φ, is effectively lowered thus reducing the associated ablation parameters such as pressure and temperature. Early experiments with laser driven shocks failed to achieve the pressures expected on the basis of the known laser focal spot size[7,8]; the reduction in pressure was attributed to the small spot effect described above. Subsequent improvements were achieved with larger focal spots[9], and shorter laser wavelengths[10,11,13,126]. A two-dimensional numerical study of this problem performed by Harrach *et al.*[127], was used to obtain analytic predictions of the dependence of the ablation pressure on the irradiation conditions. As a general rule pressure reduction due to two-dimensional plasma expansion is expected to set in with increasing intensities, and decreasing spot sizes. The experiments described here, and past experiments using the same laser and Al targets, show little evidence of a pressure reduction effect as the measured shock speeds appear to agree with the expected scaling (*cf.* Figure 5-3).

Two-dimensional motion can also take place in the shock propagating into the target. At early times the shock, being launched from a planar surface, is also planar. However, it has a tendency to expand laterally, as well as axially, and rarefactions from the edge of the shocked region penetrate towards the axis[17]; the overall effect is to expand the shock front area and reduce the shock pressure, thereby slowing it down. At very late times when the shock has propagated to distances large compared to the laser spot size, it takes on a hemispherical shape[7,15,16]. The transition from a planar to a hemispherical profile takes place roughly at a depth corresponding to the laser spot diameter. To take this description much beyond the qualitative stage requires a two-dimensional hydrocode (cylindrical symmetry) for theoretical treatment and a high speed framing diagnostic for two-dimensional observations. These capabilities were not available at the time the measurements were made.

Other effects that can modify the shock front planarity are related to the degree of non-uniformity in the deposition of the laser energy within the nominal focal spot diameter. This may also be of concern since the focal spot distribution is highly peaked as discussed in §3.2. The spatial pressure distribution at the target surface is smoothed out by thermal diffusion taking place in the ablation zone. The amount of smoothing expected from the thermal diffusion process can be estimated by considering the spatial separation, L_s, between the ablation surface where the peak pressures are developed, and the region of peak laser light absorption in the plasma. Between these regions energy is transported by electron thermal conduction. The separation between these regions is a strong function of intensity. Examination of the the simulation results shows that L_s varies with laser intensity as $L_s \sim 30\Phi^{0.67}$ where L_s is in units of μm and Φ in units of 10^{13} W/cm^2. Smoothing is stronger with increasing intensity. At $\Phi \sim 2 \times 10^{13}$ W/cm^2, $L_s \sim 45$ μm, while at $\Phi \sim 2 \times 10^{12}$ W/cm^2, $L_s \sim 10$ μm. In the former case L_s is of the order of the spot size, which would smooth out any intense features over a radius comparable

to the spot radius; however, in the latter case $L_s < D_{spot}$ so that an intense feature would be smoothed out roughly over an area with radius L_s, or a spot diameter of about 20 μm. In this respect the lower intensity shots are of more concern than the high intensity shots. From a focal spot intensity distribution, such as shown in Figure 3-3, one can construct an average intensity using a smaller effective radius (in this case L_s) to obtain an average intensity characteristic of the high intensity central feature smoothed by the thermal diffusion process. It is conceivable that the pressure attained in the intense region of the laser spot may be a factor of 2 larger than the nominal average value (i.e. P_Φ based on Φ_{60}). Nevertheless, this cannot account for the high transient speeds measured at the lower intensity range, which would imply an intensity fluctuation of a factor of 10 larger than the Φ_{60} value. It also cannot account for the transients observed at higher intensities where smoothing is expected to be much better.

An empirical estimate of the degree of planarity in the shock front can be made based on the size of the shock breakout region in aluminum foil experiments performed with the same laser and focussing optics. High resolution measurements of the shock breakout in an opaque foil have been obtained by observing the abrupt decrease in reflectivity of the rear surface at the moment the shock arrives at the surface and begins to unload[12,94,95]. This was measured by illuminating the surface with a probe beam and imaging onto a streak camera slit the region behind the laser spot where the shock emerges. Such a measurement of the breakout of a laser-driven shock in a 50 μm thick Al foil is shown in Figure 5-9. The laser intensity was about 7×10^{13} W/cm^2 in this measurement. Here, the shock is observed to emerge nearly simultaneously in a region of about 40 μm diameter with $\leq$ 2% variation in the shock speed across this breakout region, as estimated from the shock transit time. The 40 μm size of the central breakout region is consistent with the 60% energy spot diameter measured for the experiment. At diameters much larger than the central 40 μm disk the shock appears to emerge later. This breakout pattern suggests that the

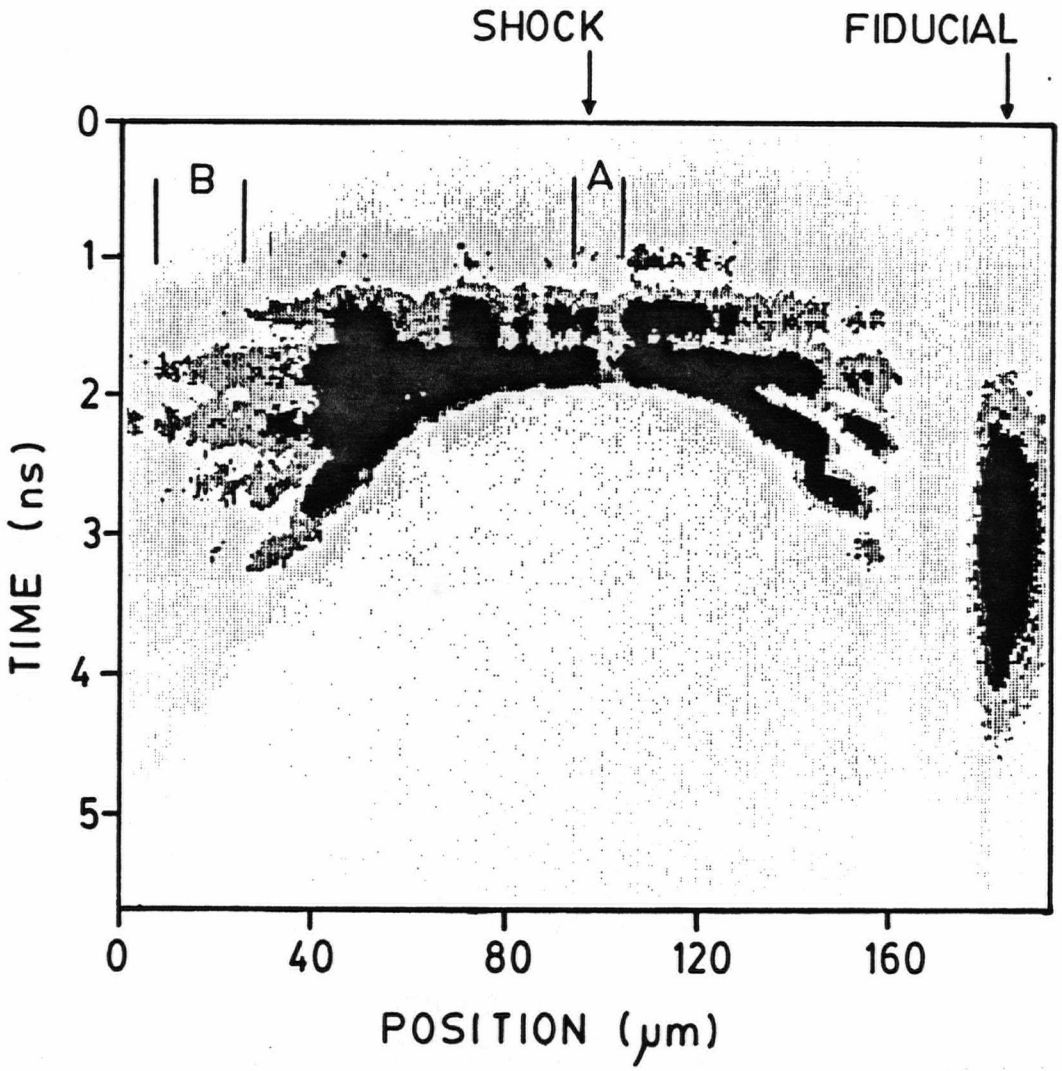

Figure 5-9 Shock breakout from a 50 μm Al foil irradiated with 7×10^{13} W/cm^2 2 ns laser pulse. This measurement was originally presented in the Ph.D. thesis of D. Parfeniuk[94].

central planar front joins smoothly onto a rounded or hemispherical shaped "wing" which is spreading outwards radially behind the planar central region, similar to a bow shock in supersonic flow.

A check on the validity of the one-dimensional model for the trajectory analysis is shown in Figure 5-10. This figure shows a comparison between a planar one-dimensional simulation (MEDUSA) and a shock trajectory derived from measurements of the transit time of the shock front through various thicknesses of Al foils[12,94]. It may be noted that the measurements reveal no sign of the anomalous effects observed in the SiO_2 targets, and appear to agree quite well with the simulations. The generally good agreement obtained in these results, and the planarity of the shock front at depths of up to 50 μm lends credibility to the use of a one-dimensional hydrodynamic analysis, at least for Al targets. Trajectory measurements on Al, Cu and Au similar to that displayed in Figure 5-10 have been performed by Cottet *et al.*[13,126] using a 0.26 μm wavelength beam (frequency quadrupled Nd laser) focussed to a similar ($\sim$ 50 μm) spot size as in our experiments. These experiments also tend to show agreement with the predictions of one-dimensional hydrodynamics for propagation depths of the order of the spot diameter.

The two-dimensional nature of the shock motion does allow another interpretation of the experiment that produces qualitative features similar to those observed. The basic idea is that the observed trajectory is sensitive, to some degree, to errors in positioning the streak camera entrance slit along the axis of the laser beam incident on the target. Specifically, the slit may not be aligned along the laser axis but offset by some distance as illustrated schematically in Figure 5-11. If the shock front is not precisely planar, and it is confined to a region of the order of the spot size, then such a positioning error could result in anomalous behaviour, depending on the degree of error. For a qualitative treatment we shall assume that the shock front is perfectly hemispherical at all times, thus representing a curved shock front

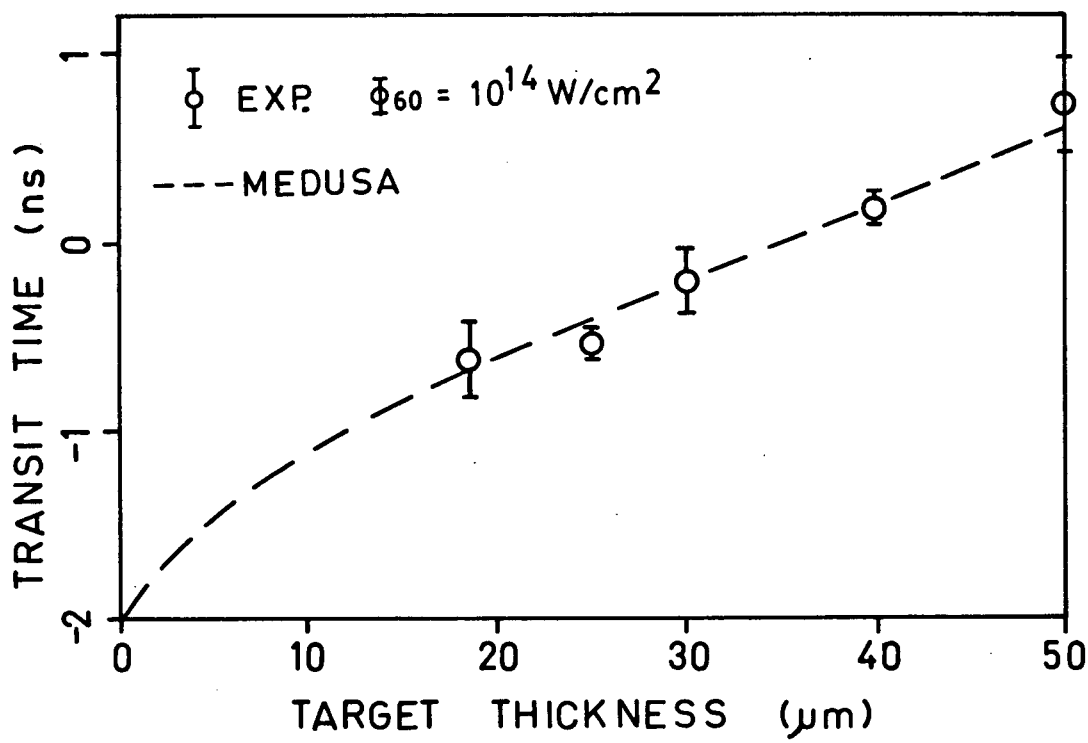

Figure 5-10 Trajectory measurement derived from transit times through various Al foil thicknesses. This measurement was originally reported in reference 12.

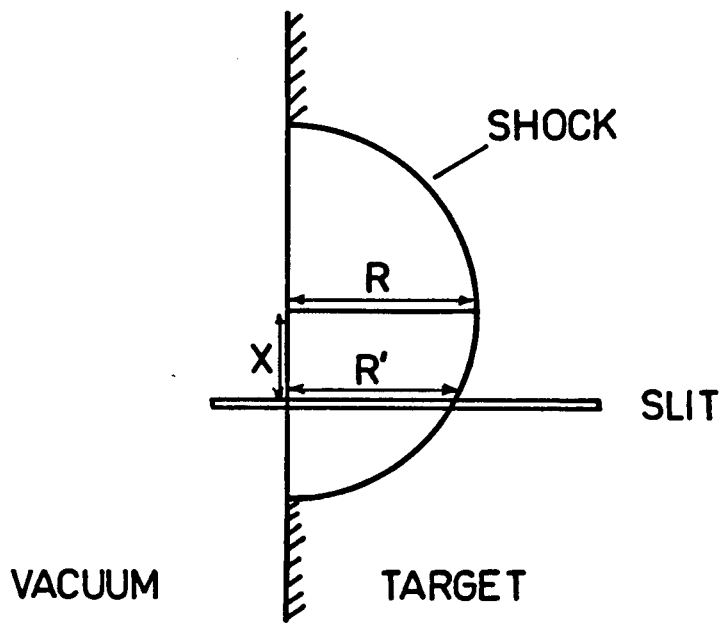

Figure 5-11 Schematic picture of the effect of positioning errors and a hemishperical shock front.

of finite area. In reality the shape of the shock front does not become hemispherical until late times, and would be more nearly planar over regions of the order of the spot size at earlier times. The hemispherical front expands with radius $R(t)$, and is measured with the streak camera slit offset a distance X from the centre. We shall assume that the radius $R(t)$ is given by the planar shock trajectory predicted in the simulations, which can be approximated by a linear relation, $R(t) = R_0 + Dt$. Here D is the shock speed, and R_0 is its position at the peak of the laser pulse ($t = 0$). The trajectory observed on the slit, $R'(t)$, is then given by, $R' = (R^2 - X^2)^{1/2}$, and the measured shock speed is given by $D' = DR/R'$. The main features of this simple picture are that the observed position R' always lags behind the true position R by a distance comparable to, but less than X; and, the observed speed appears to have a large transient feature in which it begins with a large (infinite) value, asymptotically approaching the true value, D.

This model is applied to the specific case of Figure 5-5b (shot 7-20) and the results are displayed in Figure 5-11. Here the simulated shock trajectory is approximated by $R_0 = 21.5$ μm and $D = 15.5$ km/s. Shown on the figure are "observed" trajectories for $X = 20$, 30, and 40 μm. Also shown are the actual experimental measurements. As can be seen, this simple model may account for the measurement discrepancy if we allow for a positioning error of $X \sim 30$ μm.

There are two major problems with the above model. The positioning error of the streak camera slit with respect to the laser axis is estimated to be $\pm$ 5 μm; a value of $\pm$ 10 μm may even be plausible, but an error of 30 μm is very difficult to accept. This is because the image of the target projected onto the streak camera slit was magnified $\sim 170\times$, so that a typical positioning error of < 1 mm at the slit translates to $\sim$ 5 μm at the target. If one ignores this difficulty and assumes that a positioning error of 30 μm was indeed possible (somehow), then one might expect this to explain all of the two-wave trajectories since they resemble, at least qualitatively, the trajectories predicted by the positioning error model. This,

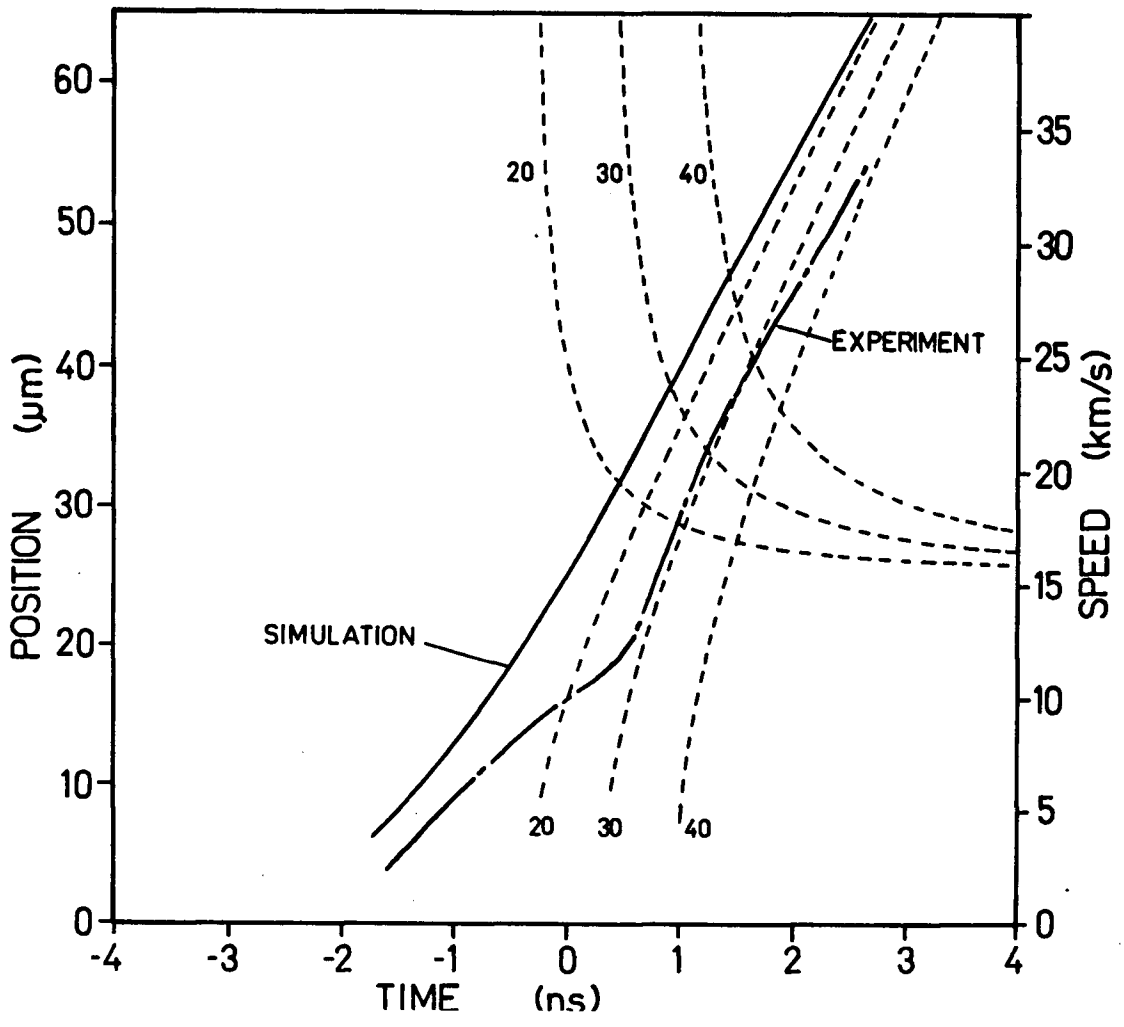

Figure 5- 12 Trajectories derived from the positioning error model. The solid curve is from a one-dimensional simulation of the experiment, and corresponds to the $\rho = 4.0$ g/cm^3 density contour. The dashed curves correspond to different slit offsets from the laser beam axis; these are labelled with values in units of μm. The lower set of curves are the observed trajectories, and the upper set are the corresponding speeds. The experimental trajectory is shown for comparison.

however, leads to a second problem: the model described above obviously cannot account for the measurements of Figures 5-4b and 5-4c in which the measured trajectories penetrate *deeper* than the calculated trajectories. This suggests, at least in these two cases, that the transient overshoot of shock velocity is a real physical effect and cannot be attributed to the type of measurement error described above.

5.4.4 Summary of interpretations

The experimental trajectories are both qualitatively and quantitatively quite different from the simulation results. The agreement between the measured and predicted shock speed scaling suggests that the pressures expected from the simulations are generated in the target.

The non-steady propagation of the high pressure shock front provides evidence that a non-equilibrium situation persists for $\sim$ 1 ns time scale and 10 - 15 μm spatial scale behind the shock front for the pressure range 60 - 400 GPa. The very large transient shows that the formation of the high pressure shock is not smooth, as in the simulations. Further understanding of the shock formation process, and the non-equilibrium dynamics is an open question, which can only be resolved with further experimentation.

The delay in the emergence of the high pressure shock is difficult to explain. If the shock motion in the target is essentially one-dimensional, then an obvious possibility is the existence of a phase transformation to a new dense phase of silica. An experiment by Pavlovskii *et al.*[88] supports this interpretation, however, there are no other experiments or theoretical works that support the existence of such a new phase. It is also difficult to see how such a phase transformation occurs on a time scale comparable to or less than the relatively long relaxation time inferred for the fused silica-stishovite transformation. Alternative interpretations might involve

two-dimensional effects, combined with measurement error. However, previous experimentation on Al targets shows that the central 40 μm diameter of the shocked region propagates on a nearly one-dimensional trajectory. Measurement error is also difficult to account for.

At present much of the experiment has been interpreted only qualitatively. A complete understanding of the experiment would have to resolve a number of prominent features in a self-consistent manner. These are the abrupt formation of the high pressure shock, the non-steady shock propagation, and the anomalous delay in shock formation at high intensities. All of these features of the experiment have become obvious "anomalies" when compared with extensive hydrocode simulations using standard equation of state data and well-known laser-plasma interaction physics.

CHAPTER 6

SUMMARY AND CONCLUSIONS

6.1 Summary

The main experimental results obtained in this study were: (i) the prominent two-wave structure in most of the shock trajectories; (ii) agreement between the asymptotic shock speed and the expected scaling of shock speed with laser intensity; (iii) non-steady propagation of the high pressure shock front at the moment of its formation; and, (iv) an anomalous delay in the formation of the high pressure shock for trajectories measured at intensities greater than about 10^{13} W/cm^2 ($P_\Phi > 200$ GPa).

In comparison, the simulations suggest that: (i) the two-wave structure should be barely observable; (ii) that there are no transient (non-steady shock) effects in an equilibrium EOS description; and, (iii) that the surface layers are compressed along isentropic paths behind a smoothly accelerating shock front. The predicted shock trajectories are modelled adequately using a single temperature EOS, inverse bremsstrahlung absorption of the laser, and Spitzer electron thermal conduction. Extensive investigations of modified versions of the basic computer model did not change the simulation results significantly.

The interpretation of the non-steady shock propagation in terms of a non-equilibrium relaxation model appears to be quite plausible, especially since similar effects have been observed and postulated for previous experiments on SiO_2. The

possibility of a significant volume collapse on the SiO_2 isentrope has been offered as an explanation for the observed delay of the shock formation in the high intensity trajectory measurements. This possibility is supported by the measurements of Pavlovski *et al.*[89], but these results have not been confirmed. Thus it should be viewed with some degree of skepticism. An alternative explanation may involve the two-dimensional nature of the shock front (at large depths) and requires an unaccountably large positioning error in the measurement. This alternative cannot explain the low intensity data in which the measured shock trajectory penetrates deeper than the equilibrium trajectory. Many questions regarding the compression process remain open. All that is known about SiO_2 already shows that it is one of the most complicated materials investigated in shock experiments, and that the current hydrocode model is certainly not adequate to describe many of the features of the trajectories.

6.2 New contributions

The results presented in this thesis are the first detailed study of the formation of a laser-driven shock in a transparent material. The observation of the non-steady propagation of the shock front has never been seen in a laser driven shock experiment. The anomalous delay in the formation of the high pressure shock at intensities $> 10^{13}$ W/cm^2 was also unexpected. The possibility of a phase transformation to a new, high density phase of silica, as reported by Pavlovskii *et al.*, has important ramifications; however, this conclusion is uncertain. These unexpected results, and the questions that remain indicate that there is more new physical information yet to be uncovered, with further experimentation, and more sophisticated modelling.

The possibilities of using laser-driven shocks to investigate non-equilibrium transformations in a shock front have, up to now, not been fully appreciated. The main emphasis in laser-driven shock research has been in realizing extremes in

pressure. With the relatively short duration pressure pulse, and small target dimensions, laser-driven shock techniques can be used to reveal non-steady shocks. This has been demonstrated clearly in the experimental results, and should lead to more refined experiments on phase transforming transparent dielectrics.

6.3 Future Work

To resolve some of the uncertainties in these results further experimentation is necessary. Firstly, new experiments should examine the same pressure range using a much larger spot size, and with a more uniform intensity distribution in the focal spot. This requires a larger laser than was used in the investigation reported here. This would reduce, or eliminate some of the uncertainties related to two-dimensional motion of the shock front. Special attention should be paid to making the spot distribution as smooth and reproducible as possible because this can lead to uncertainties in the reproducibility of the measured results.

Now that the basic technique has been verified on fused silica, it should be extended to examine other transparent materials such as α-quartz and NaCl. α-quartz is particularly interesting because although it reaches the similar final states as fused silica, the initial state is sufficiently different that the non-equilibrium dynamics of the stishovite transformation may result in quite different behaviour in the formation of the shock. It is also important to find a transparent material which behaves "normally", i.e. one which is accurately modelled with the hydrocode using a well-tested equilibrium EOS description. This can then be used as a benchmark to calibrate the hydrocode against the experiment. NaCl, or some other alkali halides might be appropriate for this.

Beyond these investigations it would be interesting to optimize the basic technique demonstrated here for studying non-steady shock propagation. Two possibilities for this can be considered. One could use a square laser pulse (flat top with short rise time) to apply a pressure step to the target. This is closer to the

ideal situation used for the purposes of the discussion in §5.4.1 of non-steady shock propagation induced by a pressure step. This kind of loading attempts to avoid dealing with slow compression of the initial layers of the target which occur with the gaussian laser pulse. Nevertheless, since any realistic laser pulse must have a finite rise time (10 - 100 ps), a sharp pressure step is only approximated with this kind of pulse. An alternative technique would use a thick ($\sim$ 30 μm) layer of aluminum bonded onto the target. A laser-driven shock developed in the aluminum could then be transmitted into the transparent target, thus applying a pressure step that is limited in rise time by the properties of the shock front in the aluminum layer ($< 10^{-12}$ s). A special pulse shape is not needed for this as long as the shock reaches the interface shortly after the peak of the pulse. Analysis of the results needs to take into account the impedance mismatch between the aluminum layer and the transparent target.

Finally, the anomalous delay in the formation of the strong shock should be investigated further by examining its sensitivity to the laser pulse length. This method should provide a means of distinguishing whether the delay effect could be related to the non-equilibrium relaxation processes inferred from the non-steady shock, or whether it is indeed caused by a phase transformation to a new phase under near thermodynamic equilibrium conditions. If the delay is related to an (equilibrium) phase transition then the measured trajectories should produce similar relative delays (delay as a fraction of pulse length) independent of the pulse length, as long as the pulse shape is conserved. This is because equilibrium hydrodynamic phenomena are inherently self-similar with no characteristic space and time scales. That is, an $x-t$ plot of the trajectory produced by a given pulse shape will have the same form as long as the x-scale (propagation distance) is increased by the same factor as the t-scale (pulse length). If a new phase transformation does exist then an accurately calibrated experiment with a longer pulse could be used to determine the transition pressure to better accuracy. If, on the other hand, the anomalous

delay effect is related to non-equilibrium effects, then a longer pulse experiment should produce better agreement with *calculated* trajectories (i.e. the relative delay should lessen) because the non-equilibrium time scale becomes smaller compared to the experimental time scale. However, the longer pulse implies a proportional increase in the laser focal spot diameter to maintain planarity in the shock front over the larger length scales; consequently the required laser energy needs to be increased in proportion to the cube of the pulse length.

References

1. B.K.Godwal, S.K. Sikka and R. Chidambaram, Phys. Rep., **102** 121 (1983)
2. R.G. McQueen, S.P. Marsh, J.W. Taylor, J.N. Fritz and W.J. Carter in: *High Velocity Impact Phenomena*, R. Kinslow ed., Academic Press, New York (1970)
3. A.C. Mitchell and W.J.Nellis, J. Appl. Phys., **52** 3363 (1981)
4. C.E. Ragan III, M.G. Silbert and B.C. Diven, J. Appl. Phys., **48** 2860 (1977)
5. J. Nuckolls, L. Wood, A. Theisson and G. Zimmerman, Nature, **239** 139 (1972)
6. K.A. Brueckner and S. Jorna, Rev. Mod. Phys., **46** 325 (1974)
7. C.G.M. van Kessel and R. Sigel, Phys. Rev. Lett., **33** 1020 (1974)
8. L. Veeser and J. Solem, Phys. Rev. Lett., **40** 1391 (1978)
9. R.J. Trainor, J.W. Shaner, J.M. Auerbach and N.C. Holmes, Phys. Rev. Lett., **42** 1154 (1979)
10. R.J. Trainor, N.C. Holmes, R.A. Anderson, E.M. Campbell, W.C. Mead, R.J. Olness, R.E. Turner and F. Ze, Appl. Phys. Lett., **43** 542 (1983)
11. A. Ng, D. Parfeniuk and L. DaSilva, Phys. Rev. Lett., **54** 2604 (1985)
12. A. Ng, D. Parfeniuk, P. Celliers, L. DaSilva, R.M. More and Y.T. Lee, Phys. Rev. Lett., **57**, 1594 (1986)
13. F. Cottet, J.P. Romain, R. Fabbro and G. Faral, Phys. Rev. Lett., **52** 1884 (1984)
14. N.C. Holmes, R.J. Trainor, R.A. Anderson, L.R. Veeser and G.A. Reeves in *Shock Waves in Condensed Matter, 1981*, W.J. Nellis, L. Seaman, R.A. Graham eds., AIP conference proceedings no. 78, New York (1982) pp. 160-163
15. C.G.M. van Kessel, Z. Naturforsch., **30a** 1581 (1975)
16. S. Ariga and R. Sigel, Z. Naturforsch., **31a** 697 (1976)

17. R.M. More in *Laser Interaction and Related Plasma Phenomena, Vol. 5*, H. Schwarz, H. Hora, M. Lubin and B. Yaakobi eds., Plenum (1981)
18. R.J. Trainor and Y.T. Lee, Phys. Fluids, **25** 1898 (1982)
19. R. Fedosejevs, Y. Teng, R. Sigel, K. Eidmann and R. Petsch, J. Appl. Phys., **52** 4186 (1981)
20. F. Amiranoff, R. Fedosejevs, R.F. Schmalz, R. Sigel and Yung-lu Teng, Phys. Rev. A, **32** 3535 (1985)
21. Ya.B. Zel'dovich and Yu.P. Raizer, *Physics of Shock Waves and High Temperature Hydrodynamic Phenomena,* W.D.Hayes and R.F. Probstein eds., Academic Press, New York (1966), Chapter XI
22. G.E.Duvall and R.A.Graham, Rev. Mod. Phys., **49** 523 (1977)
23. J.W. Shaner in *Physics of Solids Under High Pressure*, J.S. Schilling, R.N. Shelton eds., North-Holland (1981) pp. 99-108
24. J.N. Johnson and L.M. Barker, J. Appl. Phys., **40** 4321 (1969)
25. P.F. Chartagnac, J. Appl. Phys., **53** 948 (1982)
26. D.C.Wallace, Phys. Rev. B, **24** 5597 (1981)
27. D.C.Wallace, Phys. Rev. B, **24** 5607 (1981)
28. D.E.Grady, Appl.Phys.Lett., **38** 825 (1981)
29. J.W.Swegle and D.E.Grady, J.Appl.Phys., **58** 692 (1985); J.W.Swegle and D.E.Grady in *Shock Waves in Condensed Matter - 1985*, Y.M. Gupta ed., Plenum, New York (1986)
30. J.E. Dunn and D.E. Grady in *Shock Waves in Condensed Matter - 1985*, Y.M. Gupta ed., Plenum New York (1986) pp. 359-364
31. W.C. Moss, Appl. Phys. Lett., **47** 372 (1985)
32. D.J. Andrews, J. Comp. Phys., **7** 310 (1971)
33. D.B. Hayes, J. Appl. Phys., **46** 3438 (1975)
34. D.B. Hayes, J. Appl. Phys., **45** 1208 (1974)

35. J.N. Johnson, D.B. Hayes and J.R. Asay, J. Phys. Chem. Solids, **35** 501 (1974)

36. R.B. Sosman, *The Phases of Silica*, Rutgers University Press, New Brunswick, New Jersey (1965)

37. F.A. Hummel, *Introduction to Phase Equilibria in Ceramic Systems*, Marcel Dekker, New York (1984)

38. G. Behnke, H. Bilz and H. Buttner, Phys.Rev.Lett., **56** 1276 (1986)

39. L. Coes Jr., Science, **118** 131 (1953)

40. S.M. Stishov and S.V. Popova, Geokhimiya, **10** 837 (1961)

41. F.R. Boyd and J.L. England, J. Geophys. Res., **65** 749 (1960)

42. S. Akimoto and Y. Syono, J. Geophys. Res., **74** 1653 (1969)

43. E.C.T. Chao, E.M. Shoemaker and B.M. Madsen, Science, **132** 220 (1960); E.C.T. Chao, J.J. Fahey, J. Littler and D.J. Milton, J. Geophys. Res., **67** 419 (1962)

44. D. Stoffler, J. Geophys. Res., **76** 5474 (1971)

45. D.W. Gray in *AIP Handbook of Physics*, McGraw-Hill, New York (1957) §3-f

46. J.D. Jorgensen, J. Appl. Phys., **49** 5473 (1978)

47. W.P. Mason, *Piezoelectric Crystals and Their Application to Ultrasonics*, Van Nostrand, Princeton, New Jersey (1950) §6.2

48. H. Mizutani, Y. Hamano and S. Akimoto, J. Gephys. Res., **77** 3744 (1972)

49. P.W. Bridgman and I. Simon, J. Appl. Phys., **24** 405 (1953)

50. R.V. Gibbons and T.J. Ahrens, J. Geophys. Res., **76** 5489 (1971)

51. R.A.B. Devine and J. Arndt, Phys. Rev. B, **35** 9376 (1987)

52. Jerry Wackerle, J. Appl. Phys., **33** 922 (1962)

53. R.F. Trunin, G.V. Simakov, and M.A. Podurets, Izv. Acad. Sci. USSR Phys. Solid Earth, **2** 33 (1971)

54. G.A. Lyzenga, T.J. Ahrens and A.C. Mitchell, J. Geophys. Res., **88** 2431 (1983)

55. H. Sugiura, K. Kondo and A. Sawaoka, J. Appl. Phys., **52** 3375 (1981)

56. R.F. Trunin, G.V. Simakov, M.A. Podurets, B.N. Moiseyev, and L.V. Popov, Izv. Acad. Sci. USSR Phys. Solid Earth, **1** 13 (1970)

57. M.A. Podurets, L.V. Popov, A.G. Sevast'yanova, G.V. Simakov, and R.F. Trunin, Izv. Acad. Sci. USSR Phys. Solid Earth, **11** 59 (1976)

58. R.G. McQueen, J.N. Fritz and S.P. Marsh, J. Geophys. Res., **68** 2319 (1963)

59. J.L. Holm, O.L. Kleppa and E.F. Westrum, Geochimica et Cosmochimica Acta, **31** 2289 (1967)

60. L.M. Barker and R.E. Hollenbach, J. Appl. Phys., **41** 4208 (1970)

61. K. Kondo, S. Iio and A. Sawaoka, J. Appl. Phys., **52** 2826 (1981)

62. R.E. Setchell, J. Appl. Phys., **50** 8186 (1979)

63. D.E. Grady, J. Geophys. Res., **85** 913 (1980)

64. P.J. Brannon, R.W. Morris, C.H. Konrad and J.R. Asay in *Shock Waves in Condensed Matter - 1983*, J.R. Asay, R.A.Graham, G.K. Straub eds., Elsevier (1984) pp. 303-306

65. D. Schmitt, B. Svendsen and T.J. Ahrens in *Shock Waves in Condensed Matter - 1985*, Y.M. Gupta ed., Plenum, New York (1986) pp. 261-265

66. D.R. Schmitt and T.J. Ahrens in *Shock Waves in Condensed Matter - 1983*, J.R. Asay,R.A. Graham, G.K. Straub eds., Elsevier (1984) pp. 313-316

67. L.C. Chhabildas and D.E. Grady in *Shock Waves in Condensed Matter - 1983*, J.R. Asay, R.A. Graham, G.K. Straub eds., Elsevier (1984) pp. 176-178

68. L.C. Chhabildas in *Shock Waves in Condensed Matter - 1985*, Y.M. Gupta ed., Plenum, New York (1986) pp. 601-605

69. M.A. Podurets, G.V. Simakov and R.F. Trunin, Izv. Acad. Sci. USSR Phys. Solid Earth, **7** 3-11 (1976)

70. T.J. Ahrens and G.E. Duvall, J. Geophys. Res. **71** 4349-4360 (1966)

71. J. Cagnoux in *Shock Waves in Condensed Matter - 1981*, W.J. Nellis, L. Seaman, R.A. Graham eds., AIP conference proceedings no. 78, New York (1982) pp. 392-396

72. G.A. Lyzenga in *Shock Waves in Condensed Matter - 1981*, W.J. Nellis, L. Seaman, R.A. Graham eds., AIP conference proceedings no. 78, New York (1982) pp. 268-276

73. B.I. Bennett, J.D. Johnson, G.I. Kerley and G.T. Rood, Los Alamos National Laboratory report LA-7130 (February, 1978)

74. *T-4 Handbook of Material Properties Data Bases, Vol. Ic: Equations of State* K.S. Holian ed., Los Alamos National Laboratory report LA-10160-MS (1984)

75. J.F. Barnes, Phys.Rev. **153** 269 (1967)

76. R.D. Cowan and J. Ashkin, Phys. Rev., **105** 144 (1957)

77. N.W. Ashcroft and N.D. Mermin, *Solid State Physics*, Saunders College, Philadelphia (1976), Chapter 23

78. J.F. Barnes, *Thermodynamics of Nuclear Materials 1974*, International Atomic Energy Agency, Vienna, 1975 Vol. I, pp. 327-339

79. F. Ree, *Equation of State of the Silicon Dioxide System*, Lawrence Livermore National Laboratory report UCRL-52153, (1976)

80. M. Cowperthwaite and W.H. Zwisler, *TIGER Program Documentation*, Stanford Research Institute Publication No. Z106, Vol. I (1973), Vols. II-IV (1974)

81. C.A. Rouse, Astrophys. J., **137** 1286 (1963) and references therein

82. R. Grover, J. Chem. Phys. **55** 3435 (1971); E.B. Royce, *GRAY, Three-Phase Equation of State for Metals*, Lawrence Livermore National Laboratory report UCRL-51121 (1971)

83. S.L. McCarthy, *The Kirzhnits Correction to the Thomas-Fermi Equation of State*, Lawrence Livermore National Laboratory report UCID-14363 (1965)

84. K. Johnson, Lawrence Livermore National Laboratory internal report HTN-260 (1976)

85. T.J. Ahrens in *Shock Waves in Condensed Matter - 1985*, Y.M. Gupta ed., Plenum, New York (1986), pp. 571-588

86. R.G. McQueen, J.N. F ritz and S.P. Marsh, J. Geophys. Res., **69** 2947 (1964)

87. W.H. Ramsey, Royal Astronomical Society, Monthly Notices **108** 406-413 (1948)

88. A.I. Pavlovskii, N.P. Kolokol'chikov, M.I. Dolotenko, and A.I. Bykov, Sov. Phys. JETP Lett., **27** 264 (1978)

89. R.S. Hawke, D.E. Duerre, J.G. Huebel, R.N. Keeler, and H. Klapper, Phys. Earth Planet. Interiors **6** 44 (1972)

90. J.N. Fritz and R.G. McQueen in *Shock Waves in Condensed Matter - 1983*, J.R. Asay, R.A. Graham, G.K. Straub eds., Elsevier (1984), pp. 73-76

91. H.K. Mao, private communication

92. A.E. Carlsson, N.W. Ashcroft and A.R. Williams, Geophys. Res. Lett. **11** 617 (1984)

93. D. Pasini, Ph.D. Thesis, University of British Coumbia (1984), unpublished

94. D. Parfeniuk, Ph.D. Thesis, University of British Coumbia (1987), unpublished

95. A. Ng, D. Parfeniuk, L. DaSilva and P. Celliers, Laser and Particle Beams, **4** 555 (1986)

96. Hamamatsu Temporal Disperser model C1370-01, Hamamatsu Corp., 420 South Ave., Middlesex NJ 08846

97. Obtained from Fluorocarbon Co., U.S. Quartz Division, 17 Madison Road, Fairfield N.J. 07006 USA

98. Hamamatsu photodiode model R1193U

99. Gentec Inc., 2625 Dalton St., Ste-Foy Quebec, G1P 3S9, Canada

100. Scientech Inc., 5649 Arapahoe ave., Boulder CO 80303, USA

101. J.P. Christiansen, D.E.T.F. Ashby and K.V. Roberts, Comp. Phys. Commun. **7** 271 (1974)

102. D. Mihalas and B.W. Mihalas, *Foundations of Radiation Hydrodynamics* Oxford University Press, New York (1984), pp. 479-489

103. D.R. Bates, A.E. Kingston and R.W.P. McWhirter, Proc. R. Soc. London, Ser. A, **267**, 297 (1962); D.R. Bates, A.E. Kingston and R.W.P. McWhirter, Proc. R. Soc. London, Ser. A, **270**, 155 (1962)

104. Ya.B. Zel'dovich and Yu.P. Raizer, *Physics of Shock Waves and High Temperature Hydrodynamic Phenomena*, W.D.Hayes and R.F. Probstein eds., Academic Press, New York (1966), Chapter III §5

105. R.W.P. McWhirter in *Plasma Diagnostic Techniques*, R.H. Huddlestone and S.L. Leonard, eds., Academic Press, New York (1965), Chapter 5

106. SESAME Data Libraray, Table 17380

107. C.E. Max, C.F. McKee and W.C. Mead, Phys. Fluids, **23** 1620 (1920)

108. P. Colella and P.R. Woodward, J. Comp. Phys., **54** 174 (1984)

109. S.K. Godunov, Mat. Sb., **47** 271 (1959)

110. P. Colella and H.M. Glaz, J. Comp. Phys., **59** 264 (1985)

111. D.J. Nagel, P.G. Burkhalter, C.M. Dozier, J.F. Holzrichter, B.M. Klein, J.M. McMahon, J.A. Stamper and R.R. Whitlock, Phys. Rev. Lett., **33** 743 (1974)

112. W.C. Mead, E.M. Campbell, K.G. Estabrook, R.E. Turner, W.L. Kruer, P.H.Y. Lee, B. Pruett, V.C. Rupert, K.G. Tirsell, G.L. Stradling, F. Ze, C.E. Max, and M.D. Rosen, Phys. Rev. Lett., **47** 1289 (1981)

113. B. Yaakobi, P. Bourke, Y. Conturie, J. Delettrez, J.M. Forsyth, R.D. Frankel, L.M. Goldman, R.L. McCrory, W. Seka, J.M. Soures, A.J. Burek and R.E. Deslattes, Opt. Commun., **38** 196 (1981)

114. T. Mochizuki, T. Yabe, K. Okada, M. Hamada, N. Ikeda, S. Kiyokawa, and C. Yamanaka, Phys. Rev. A, **33** 525 (1986)

115. P. Alaterre, H. Pepin, R. Fabbro and B. Faral, Phys. Rev. A, **34** 4184 (1986)

116. D. Duston, R.W. Clark, J. Davis and J.P. Apruzese, Phys. Rev. A, **27** 1441 (1983)

117. D. Duston, R.W. Clark and J. Davis, Phys. Rev. **A**, **27** 1441 (1983)

118. J. Delettrez, Can. J. Phys., **64** 932 (1986)

119. W.M. Manheimer, D.G. Colombant and J.H. Gardner, Phys. Fluids, **25** 1644 (1982)

120. P. Mora, Phys. Fluids, **25** 1051 (1982)

121. R.F. Schmalz, J. Meyer-ter-Vehn, and R. Ramis, Phys. Rev. A, **34** 2177 (1986)

122. R.E. Marshak, Phys. Fluids, **1** 24 (1957)

123. Ya.B. Zel'dovich and Yu.P. Raizer, *Physics of Shock Waves and High Temperature Hydrodynamic Phenomena*, W.D.Hayes and R.F. Probstein eds., Academic Press, New York (1966), Chapter X

124. R. Pakula and R. Sigel, Phys. Fluids, **28** 232 (1985)

125. K. Eidmann and T. Kishimoto, Appl. Phys. Lett., **49** 377 (1986)

126. R. Fabbro, B. Faral, J. Virmont, F. Cottet, J.P. Romain and H. Pepin, Phys. Fluids, **28** 3414 (1985)

127. R.J. Harrach, Y.T. Lee, R.J. Trainor, N.C. Holmes, M.D. Rosen, D.L. Banner and R.J. Olness in *Shock Waves in Condensed Matter, 1981*, W.J. Nellis, L. Seaman, R.A. Graham eds., AIP conference proceedings no. 78, New York (1982) pp. 164-168